Applications of Liquid Crystals in Laser
Resonators and Amplifiers


Jae-Cheul Lee
Ph.D. Thesis

# APPLICATIONS OF LIQUID CRYSTALS IN LASER RESONATORS AND AMPLIFIERS

by

Jae-Cheul Lee

Submitted in Partial Fullfilment

of the

Requirements for the Degree

## DOCTOR OF PHILOSOPHY

Supervised by Professor Stephen D. Jacobs

The Institute of Optics

The University of Rochester

Rochester, New York

1990

# CURRICULUM VITAE

Jae-Cheul Lee was born in 1956 at Buyeo, Choong Cheong Nam- Do in Korea. He holds a M.S. degree in Optics from the University of Rochester in 1987, B.S. and M.S. in Electronic Engineering from the Yonsei University in Korea in 1980 and 1982, respectively.  He has been employed by Daewoo Heavy Industries Ltd. since 1982.

# LIST OF PUBLICATIONS AND PATENTS

## PUBLICATIONS

"Design and Construction of Liquid Crystal Laser End Mirrors," Jae-Cheul Lee and S. D. Jacobs, Appl. Phys. Lett., submitted for publication (April 1990).

"TEM$_{00}$ Mode and Mono-Mode Operation with a Cholesteric Liquid Crystal as a Laser End Mirror," Jae-Cheul Lee, S. D. Jacobs, T. Gunderman, A. Schmid, T. J. Kessler, and M. D. Skeldon, Opt. Lett., submitted for publication (March 1990).

"Laser Beam Apodizer Utilizing Gradient-Index Optical Effects in Liquid Crystals," Jae-Cheul Lee, S. D. Jacobs, and K. J. Skerrett, Opt. Eng., submitted for publication (December 1989).

"Effects of Anchoring Under Intense Optical Fields in a Cholesteric Liquid Crystal," Jae-Cheul Lee, A. Schmid, and S. D. Jacobs, Mol. Cryst. & Liq. Cryst. 166, 253–265 (1989).

"Gain Squaring in a Cr:Nd:GSGG Active-Mirror Amplifier Using a Cholesteric Liquid Crystal Mirror," Jae-Cheul. Lee, J. H. Kelly, D. L. Smith, and S. D. Jacobs, IEEE J. Quantum Electron. 24, 2238–2242 (1988).

"Nd:YAG Laser with Cholesteric Liquid Crystal Cavity Mirrors," J. C. Lee, S. D. Jacobs, and R. J. Gingold, <u>Advances in Nonlinear Polymers and Inorganic Crystals, Liquid Crystals, and Laser Media</u> (SPIE, Bellingham, WA, 1988), Vol. 824, pp. 7–17.

"High-Repetition-Rate Cr:Nd:GSGG Active-Mirror Amplifier," J. H. Kelly, D. L. Smith, J. C. Lee, S. D. Jacobs, D. J. Smith, J. C. Lambropoulos, and M. J. Shoup III, <u>Opt. Lett.</u> <u>12</u>, 996–998 (1987).

"Retro-Self-Focusing and Pinholing Effect in a Cholesteric Liquid Crystal," J. C. Lee, S. D. Jacobs, and A. Schmid, <u>Mol. Cryst. Liq. Cryst.</u> <u>150b</u>, 617–629 (1987).

"Refractive Index and $\Delta n/\Delta T$ of Cr:Nd:GSGG at 1064 nm," Jae-Cheul Lee and S. D. Jacobs, <u>Appl. Opt.</u> <u>26</u>, 777–778 (1987).

## Patents

"Gradient Index Liquid Crystal Devices Method of Fabrication Thereof," Jae-Cheul Lee and S. D. Jacobs, patent application submitted on december 1989.

# ACKNOWLEDGMENTS

# ABSTRACT

The unique linear optical properties of cholesteric liquid crystals are reviewed for laser applications. Jones matrix representations of elements are derived for the first time based on an analogy with a combination of conventional optical components.

We show both in theory and experiment that under exposure to a plane wave with Gaussian intensity distribution, a retro-self-focusing effect occurs in which the reflected field comes to focus, as a result of intensity-dependent pitch dilation in cholesteric liquid crystals. We also show how the anchoring conditions at the substrate-cholesteric liquid crystal interface affect the pitch change of a cholesteric liquid crystal in an intense optical field.

We explain how a simple cholesteric liquid crystal element, when utilized as a laser end mirror in a solid state laser oscillator, can be used to achieve mono-longitudinal mode in addition to $TEM_{00}$ mode operation.

The mechanism for gain squaring in a Cr:Nd:GSGG active-mirror amplifier using a cholesteric liquid crystal mirror is explained in terms of the optical properties of cholesteric liquid crystals. The use of a CLC element permits the beam to traverse through the gain medium twice.

The fabrication of laser beam apodizers with large clear aperture utilizing fluid thickness variation and gradient-index optical effects in cholesteric liquid crystals is described. A circular apodizer is discussed, in which the thickness variation of cholesteric liquid crystal fluid allows reshaping the input laser beam profile. Here the thickness variation is obtained by two substrates with different inner surface profiles. The ability to vary the order of the super-Gaussian is established by using the mixing properties of liquid crystals to create a gradient index optical effect. A soft edge profile

is achieved by filling a cell with two seperate cholesteric liquid crystal mixtures with different selective reflection bands. The fluid-like property of liquid crystals allows them to mix at the interface. In this overap region, the reflectivity changes as a function of position. An electro-optic, profile-tunable apodizer, based on nematic liquid crystals is then explored to give rise to a fine tuning capability in both the clear aperture and the order of super-Gaussian edge-profile.

# TABLE OF CONTENTS

**Chapter**

x

# LIST OF FIGURES

xiv

# LIST OF TABLES

# LIST OF SYMBOLS

| | |
|---|---|
| A,B,C,D | parameters for ABCD matrix formalism |
| $\alpha$ | apex angle of the prism |
| B | background intensity |
| $\beta$ | normalization factor of intensity $(= \epsilon_a / 32 \pi k_{22} \kappa^2)$ |
| c | velocity of light |
| d | cavity length |
| $\vec{D}$ | electric displacement vector |
| $\delta$ | detuning parameter $\{= 2\pi(1/\lambda - 1/\lambda_o)n_{av}\}$ |
| $\delta_p$ | phase retardation |
| $\hat{e}_+$ | Jones matrix representation for circularly polarized light |
| $E_+, E_-$ | electric field amplitudes in a circular base |
| $\varepsilon_+, \varepsilon_-$ | electric field amplitudes without $e^{ikz}$ term.in $E_+$ and $E_-$ |
| $E_x, E_y$ | electric field amplitudes in a cartesian coordinate |
| $\epsilon_{\parallel}, \epsilon_{\perp}$ | dielectric constant parallel and perpendicular to the director, respectively |
| $\epsilon_{av}$ | average dielectric constant |
| $\epsilon_a$ | optical dielectric anisotropy |
| f | a form of solution for a twisted nematic liquid crystal. |
| $f_1, f_2$ | focal length of the mirror |
| F | free energy |
| $\phi$ | wave number which satisfies Maxwell's equation in a CLC medium with infinite thickness |

| $\phi_+(0)$ | phase of the input right circularly polarized light at z=0 in a CLC medium |
|---|---|
| $\phi_-(0)$ | phase of the reflected field at z=0 from a CLC element |
| $\gamma$ | material parameter $(=2\epsilon_{av}/\epsilon_a)$ |
| $i$ | incidence angle of the beam on the prism |
| $I$ | normalized input intensity of the light at z=0 in a CLC medium |
| $I_p$ | Gaussian intensity distribution |
| $I_o$ | maximum intensity of $I_p$ |
| $I_o(r)$ | output intensity as a function of radius |
| $I_i(r)$ | input intensity as a function of radius |
| $I_s$ | intensity for interference between two counter-propagating waves |
| $J$ | normalized input intensity of the light at z=L in a CLC medium |
| $\varphi$ | total phase change in an uniaxial crystal |
| $\varphi_o$ | phase change $\varphi$ at the center of the beam |
| $k$ | wave number in air |
| $k_o$ | wave number $(=2\pi\epsilon_{av}/\lambda)$ |
| $k_1$ | wave number $(=2\pi\epsilon_a/2\lambda)$ |

| | |
|---|---|
| $k_{ez}$, $k_{oz}$ | wave number for extra-ordinary and ordinary wave, respectively |
| $k_r$, $k_l$ | wave number for right and left circularly polarized light, respectively |
| $k_u$, $k_v$ | wave number in (u,v) coordinates system |
| $k_x$, $k_y$ | wave number in (x,y) coordinates system |
| $k_{11}$, $k_{22}$, $k_{33}$ | Frank elastic constants |
| $\Delta k$ | detuning parameter |
| $\kappa$ | coupling coefficient at wavelength $\lambda$ |
| $\kappa_o$ | coupling coefficient at selective reflection band peak wavelength $\lambda_o=\pi\Delta n/\lambda_o$ |
| $\ell$ | beam path length |
| L | liquid crystal fluid thickness |
| $\lambda$ | wavelength |
| $\Delta\lambda$ | bandwidth of selective reflection |
| $m_1$, $m_2$ | normalized wave number, $\phi/k_o$ |
| $n_{av}$ | average refractive index |
| $n_e$ | extra-ordinary refractive index |

| | |
|---|---|
| $n_o$ | ordinary refractive index |
| $n_{e,ch}$ | extra-ordinary refractive index for CLC chiral structure |
| $n_{e,ch}$ | ordinary refractive index for CLC chiral structure |
| $n_{e,n}$ | extra-ordinary refractive index for nematic substructure |
| $n_{o,n}$ | ordinary refractive index for nematic substructure |
| $n_x, n_y, n_z$ | cartesian components of the director |
| $\Delta n$ | optical birefringence |
| $P_o$ | pitch length at selective reflection band peak wavelength |
| $q_o$ | helix wave number ($=2\pi/P_o$) |
| $Q(u)$ | fourth-order polynomial as a function of normalized intensity u |
| $\theta$ | angle between the initial and final directions of the ray (Chap. 4) |
| $\Delta\theta$ | change of angle $\theta$ due to temperature |
| $\theta_f$ | rotation angle of the straight fringes in shearing interferogram |
| $\theta(z)$ | orientation angle of molecules |

| | |
|---|---|
| $\Theta$ | rotation angle of linearly polarized light in an optically active medium |
| r | radial distance; angle of refraction in prism (Chap. 4) |
| $r_0$ | radius of flat-top region in a profile-tunable laser beam apodizer |
| $r_1$ | half of the clear aperture of the amplifying device |
| R | reflectivity of CLC mirror |
| $R_{CLC}$ | effective radius of curvature of CLC mirror |
| $R_d$ | effective radius of curvature of laser rod |
| $R_0$ | radius of curvature of output coupler |
| $\rho$ | electric field amplitude ratio between right and left circularly polarized light for the solution of Maxwell's equation in a CLC medium |
| $\rho$, $\rho'$ | radius of curvature of the substrates (Chap. 5) |
| s | shearing distance |
| S | normalized intensity at z in a CLC medium where the helix wave number is equal to $q_0$ |
| t | time |
| $t_f$ | fringe spacing in a shearing interferogram |

| | |
|---|---|
| $T(r)$ | transmission function of the apodizer |
| $\Delta T$ | temperature difference |
| $u(z)$, $v(z)$ | normalized intensity for forward($u$) and counter($v$)-propagating optical fields in a CLC medium |
| $u_1$, $u_2$, $u_3$, $u_4$ | solutions of a fourth-order polynomial of $Q(u)$ |
| $w$ | beam radius |
| $w_A$ | beam radius at position A outside of the cavity |
| $w_o$ | beam radius at the output coupler |
| $\omega$ | angular frequency |
| $\Omega$ | rotation angle of isogyre pattern in a CLC medium |
| $\psi$ | a phase term in coupled amplitude equations |
| $\Delta y$ | displacement of the laser beam spot |
| $\sigma$ | $\kappa^2 - \delta^2$ |

# CHAPTER I

## Introduction

Over the past 15 years, major advances in the field of liquid crystals have been achieved. The main motivation was the application of liquid crystals for displays.[1,2] Low voltage requirements, low power consumption, compactness and flexible size were the unique features that made liquid crystal displays (LCDs) preferable. LCDs are flat and nonemissive, whereas CRTs are curved and may emit harmful x-ray radiation. Another important factor has been the compatibility of LCDs with integrated circuits. This reduces the cost and size of various consumer products such as calculators and watches. Research projects on liquid crystals covering both theory and experiment have been initiated to understand their unique properties. As a result, researchers have been able to synthesize liquid crystals tailored to exhibit a broad range of physical properties.

Many applications in different fields are found in the literature.[3-6] Applications of liquid crystals involving lasers have occured in image processing such as spatial light modulators[7] and optical A/D converters.[8] Power limiters[9,10] and beam deflectors[11] are also described in the literature. Applications of liquid crystals in large laser systems[12-15] were explored, starting in 1979 by S. D. Jacobs. He realized that large clear aperture requirements of some optical components could not be easily satisfied by solid crystalline materials. Solid crystalline materials were either very expensive, not available in large clear apertures and large quantities, or could not be reused once damaged by intense laser beams. Liquid crystals were the solution for the problems described above.

The purpose of this research is to better understand the interaction of laser radiation with cholesteric liquid crystals, and to exploit the optical properties of cholesteric liquid crystals to reduce the complexity and improve the quality of solid state laser systems.

In this chapter, we will briefly explain the definition and types of liquid crystals and their chemical structures. The alignment and fabrication of liquid crystal devices will be reviewed.

## 1.1 Definition and Classification of Liquid Crystals

The liquid crystal state of matter was discovered in cholesteryl benzonate by the Austrian botanist F. Reintzer in 1880.[16] The term "Liquid Crystals" first used by German Physicist O. Lehmann in 1890, designates a state of matter that is intermediate between the solid crystalline and the isotropic liquid phases. Liquid crystals are also called mesophases or mesomorphic phases because of their intermediate nature. Liquid crystals flow like ordinary liquids but exhibit anisotropic properties.

There are two processes by which liquid crystallinity is observed.[15] In thermotropic liquid crystals, the presence of a liquid crystalline phase depends on temperature. As the temperature is increased, a thermotropic compound passes from an anisotropic solid phase that exhibits optical scatter into a liquid crystal phase. At higher temperatures, the liquid crystal phase disappears and the fluid become isotropic. This phase transition is reversible. In lyotropic liquid crystals, the phase change depends on solvent concentration. A waxy solid becomes a lyotropic liquid crystal as solvent concentration increases and then disappears at high solvent concentrations. In this thesis, the focus will be on the laser applications of thermotropic liquid crystals.

Liquid crystal molecules are generally organic in nature and elongated in shape. These cigar shaped molecules are more or less parallel to each other in the mesophase and their long range orientational ordering gives rise to their anisotropic physical properties. This orientational ordering is measured by the orientational order parameter. Depending on the molecular arrangement and ordering, liquid crystals based on Friedel's proposal[17] are classified into three types; nematic, cholesteric, and smectic. Schematic diagrams of these basic types are shown in Fig. 1.1.



(a)

(b)

(c)
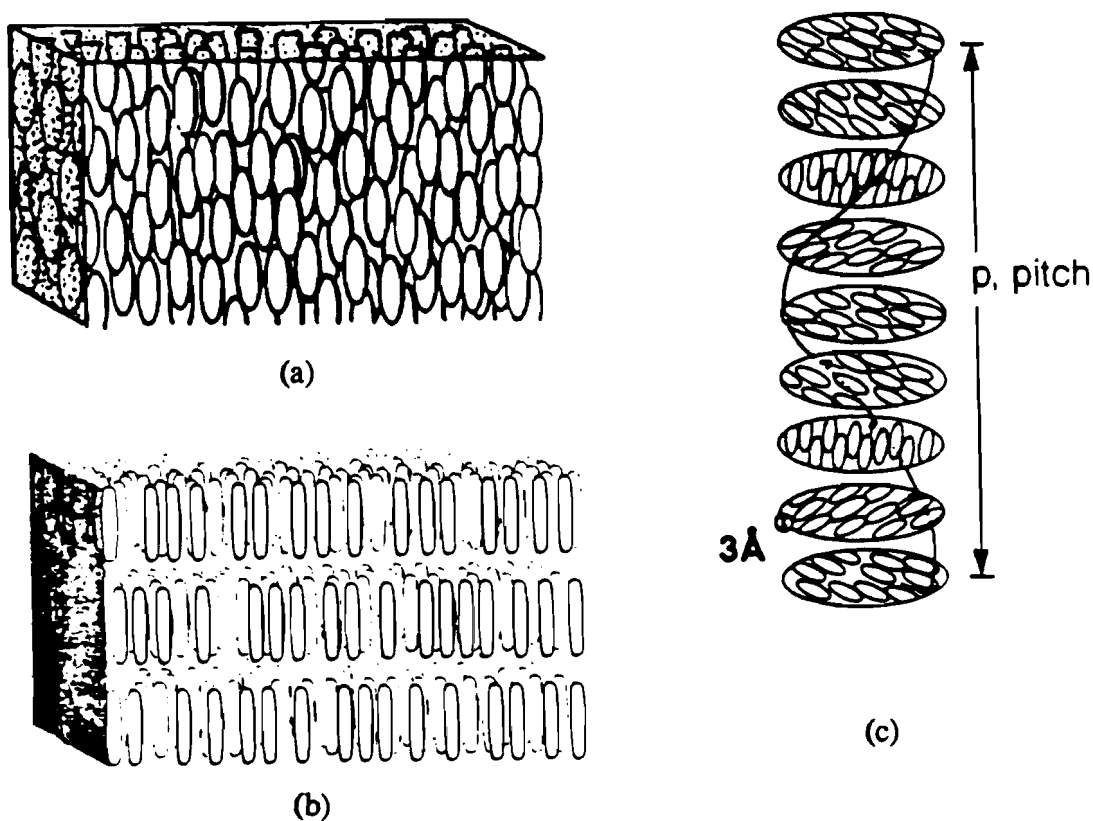
Fig. 1.1     Molecular structures of liquid crystals.

(a) nematic (b) smectic (c) cholesteric

- Nematic Liquid Crystals

The nematic is derived from the Greek word 'nemato' meaning thread-like, because the disinclinations in liquid crystals (which correspond to dislocations in solid crystals) appear thread-like when observed between crossed polarizers. In this state, nematic molecules spontaneously align with their long axes parallel to one another, but there is no layered separation as shown in Fig.1.1(a). The applications of nematic liquid crystals are based on their low viscosity and high birefringence which varies from 0.04 to 0.4.

- Smectic Liquid Crystals

The smectic is derived from the Greek word 'smectic' meaning soap-like, because the earlier smectic liquid crystals were soaps such as sodium palmitate.[2] Even though most currently studied smectic liquid crystals are non-soaps, the same name is still used. In this class the molecules are arranged in a series of layers as shown in Fig. 1.1(b). The long axes of the molecules in each layer are perpendicular to the plane of the layer. Smectic liquid crystals are much more viscous than nematic liquid crystals, but their layered structure does allow for a sliding motion. Smectics are divided into nine subclasses A, B, C, D, E, F, G, H, and I depending on the molecular arrangement inside the layers.

- Cholesteric Liquid Crystals

The cholesteric liquid crystals were derivatives of cholesterol from which the name was derived. Cholesteric liquid crystals exhibit a layered structure like smectics, but the molecules within the each layer are ordered like nemetics as shown in Fig. 1.1(c). The rotation of layers throughout the fluid gives rise to a helical structure. This helical structure leads to the important optical properties of selective reflection in

wavelength and polarization. The direction of rotation of the helix can be left-handed or right-handed.

## 1.2 Chemical Structure of Liquid Crystals

Most liquid crystal compounds have the following chemical structure[2,15]:

$$R - A - X - B - R'$$

It consists of two rigid aromatic groups (A, B) coupled with a central linkage group (-X-). R, R' are terminal groups along the molecular long axis. In most cases, the two aromatic groups are benzene rings. The most important central linkage groups X are biphenyl(-), Schiff bases (CH=N), azobenzenes (N=N) , and azoxy benzenes (N=NO). The chemical structures of some biphenyl-type liquid crystal phases are shown in Fig. 1.2.[18] In this example, CN(cyano), $CH_3(CH_2)_n$ (alkyl), and $CH_3(CH_2)_nO$ (alkoxy) are used as terminal groups. The nematic liquid crystal, E7, which has been used in most of our research applications, is a mixture of 47% K15, 25% K21, 18% M24, and 10% T15. This eutectic has a liquid crystal phase in the temperature range of -10° to 60.5°C.

## 1.3 Alignment and Fabrication of Liquid Crystal Devices

Making good liquid crystal devices is not an easy thing to do. It requires many trials until one finds a set of optimal conditions. However, there are some recipes which are well known.[1] In this section, we introduce the liquid crystal materials we have used for laser applications and explain alignment methods and fabrication procedures for devices. We also introduce important nomenclature for the liquid crystal elements, which is useful to this work.

K15: cyano-alkyl-biphenyl $CH_3(CH_2)_4$ —⬡—⬡— CN

K21: cyano-alkyl-biphenyl $CH_3(CH_2)_6$ —⬡—⬡— CN

M24: cyano-alkoxy-biphenyl $CH_3(CH_2)_7O$ —⬡—⬡— CN

T15: cyano-terphenyl $CH_3(CH_2)_4$ —⬡—⬡—⬡— CN
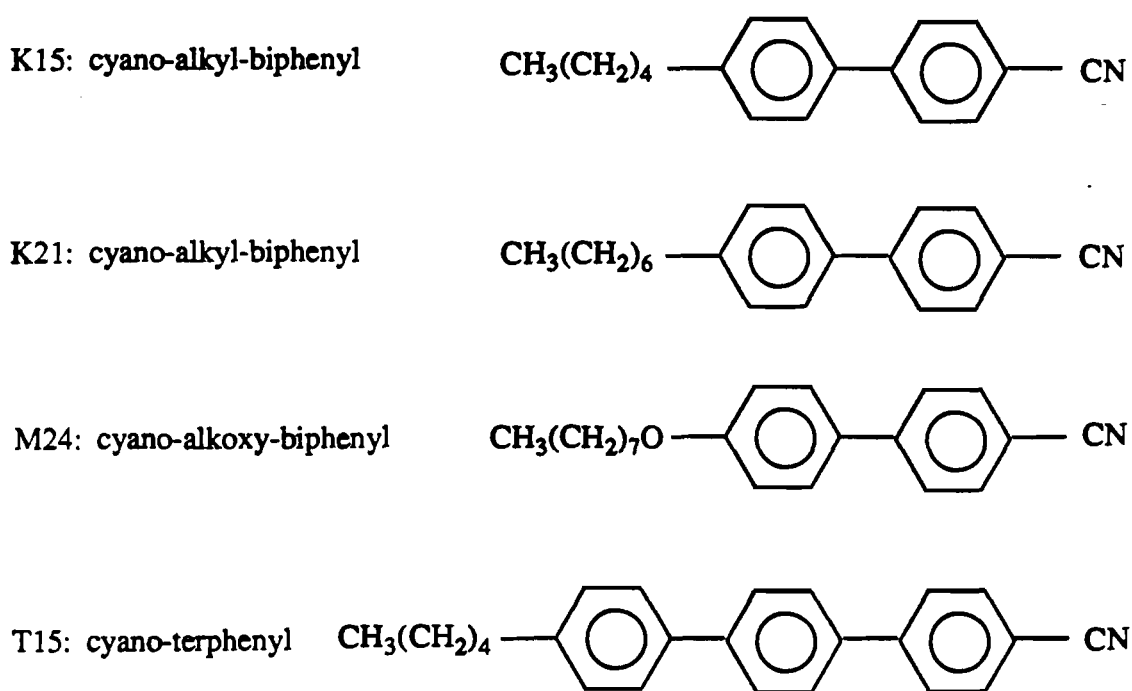
Fig. 1.2    Chemical structures of some nematic liquid crystals.

### 1.3.1 Liquid Crystal Materials

Nematic liquid crystals are commercially available.[19] They can be used without further purification. For our laser applications of liquid crystals, two different nematic liquid crystals, E7 and ZLI 1167 were used. The physical properties of these two nematic liquid crystals are summarized in Table 1.1. Our cholesteric liquid crystals are mixtures of either one of the above nematics and a chiral additive. The chiral material causes the director of liquid crystal molecules to twist its orientation in a helical manner. CB15 is a right-handed chiral additive which we have used. The blending

Table 1.1

Physical Properties of Two Nematic Liquid Crystals

| | S -N*(°C) | Clearing temp. (°C) | $\Delta n$ @589.6 and 20°C | $n_e$ | $n_o$ | $\in_\parallel$ | $\in_\perp$ | Viscosity (mm²/s) | Elastic Constants [x 10⁻⁷ dyne] | | |
| | | | | | | | | | $k_{11}$ | $k_{22}$ | $k_{33}$ |
|---|---|---|---|---|---|---|---|---|---|---|---|
| E7 | <-20 | 60.5 | 0.225 | 1.746 | 1.521 | 19.0 | 5.2 | 40 | 11.1 | -- | 17.1 |
| ZLI1167 | 32 | 83 | 0.06 | 1.52 | 1.46 | 7.5 | 3.6 | -- | -- | -- | -- |

*S-N: Smectic to nematic phase transition

(relative concentration) ratio of the chiral additive component determines the pitch of the helical structure. In blending, adding more nematic liquid crystal increases the pitch length of the helical structure and adding more chiral additives decreases the pitch length of the helical structure, P. The helical structure of a cholesteric liquid crystal gives rise to a selective reflection band in wavelength. The peak (or center) wavelength of the selective reflection band, $\lambda_o$, is equal to $n_{av}P$. For $\lambda_o$ = 1064 nm, [78.64% of E7 and 21.36% of CB15] and [80.70% of ZLI1167 and 19.30% of CB15] are required, respectively.

### 1.3.2 Alignment of Liquid Crystals

Liquid crystal devices consist of a liquid crystal fluid layer confined between a pair of glass substrates. These are separated by spacers of appropriate thickness. Alignment of liquid crystals is achieved by a cumulative ordering of the molecules affected by the surface force of the substrates. Alignment configurations useful for most applications are depicted in Fig. 1.3. Homogeneous and homeotropic alignment are obtained for nematics when the long axes of the molecules align either parallel (a) or perpendicular (b) to the substrate surface. Homogeneous alignment is obtained by coating the inner substrate surface with a thin film of a polymer and by buffing it unidirectionally to create fine grooves on the surface. There are several polymers that have been used for this purpose[2]:

- 0.2% polyvinyl alcohol (PVA) in deionized water: This produces good alignment but is susceptible to moisture.
- 0.2% Nylon® in formic acid as a solvent: This has a good chemical stability against most of the liquid crystals. However, it is not good for

production because it requires an acid as a solvent; it takes over one hour to evaporate the acid.

- 0.2% polyimide in N-methylpyrollidone: This is the most usually employed material for displays today.

In addition to these, the oblique evaporation of various materials such as gold, SiOx, and MgF$_2$ can create homogeneous alignment.[20–22] However this does not produce a unidirectional, low tilt angle (with respect to the plane of the substrate surface) of the liquid crystal molecules. The polymer coating and unidirectional buffing procedure generates a low tilt angle (2–5°) alignment of liquid crystal molecules. Homeotropic alignment in nematics is obtained by treating the glass substrate surface by lecithin or some other surfactant. Quasi-homeotropic alignment can be achieved by oblique vacuum deposition of an SiOx coating.[2]

Among the many structures of cholesteric liquid crystals, the representatives are Grandjean (c) and focal-conic (d) in Fig. 1.3. In the Grandjean (or planar) texture, the alignment of helical axes is perpendicular to the glass substrates. This is achieved by treating the surface with homogeneous aligning agents or just mechanical shear. In the focal-conic texture, the helical axes are randomly oriented. This is obtained by treating the surface with homeotropic aligning agents, or by thermal quenching without a mechanical shear.

### 1.3.3 Device Fabrication Procedures

<u>Substrate Selection</u>:

38 mm diameter BK-7 substrates with refractive index of 1.509 at 1064 nm were used to fabricate devices. This glass is chemically stable and does not interact
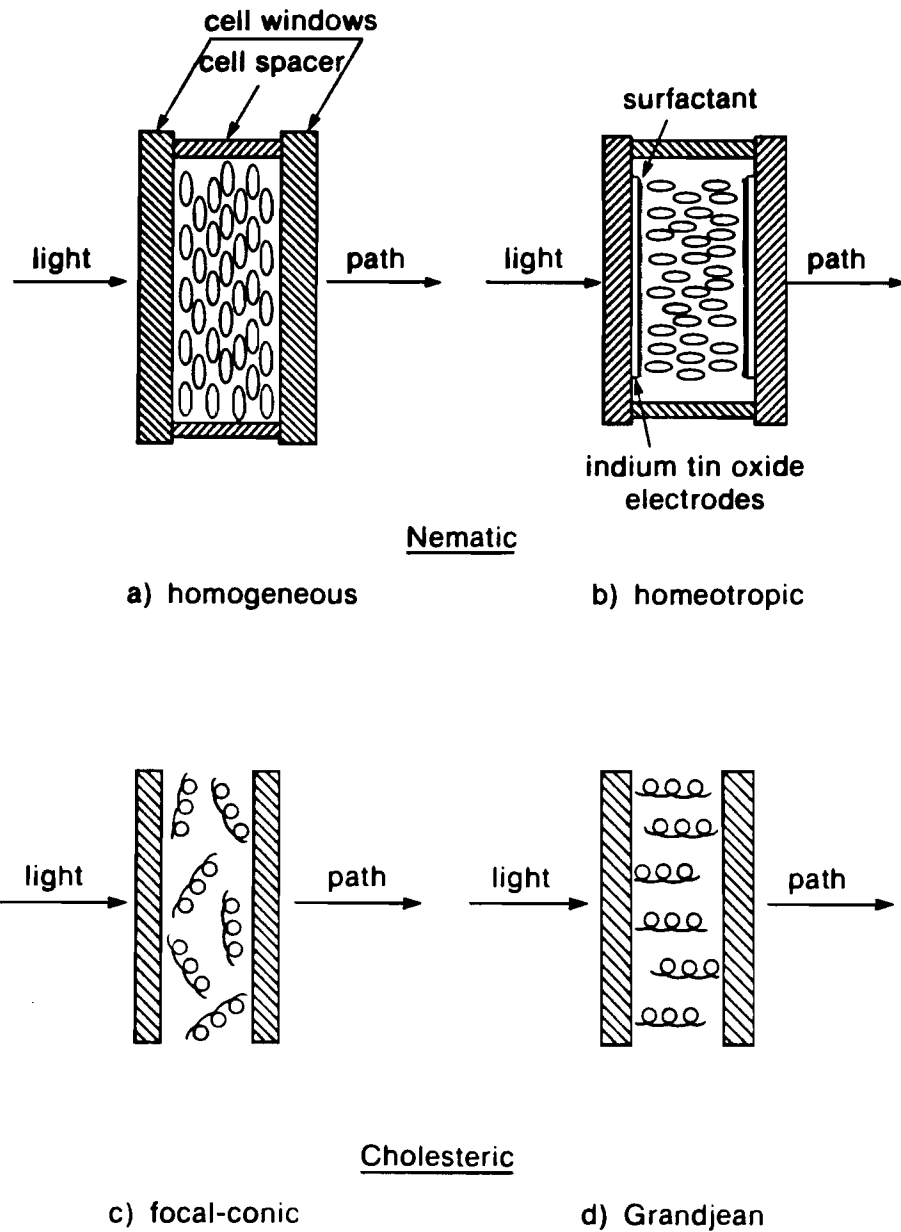
Fig. 1.3   Molecular alignment configurations for nematic (a and b) and

cholesteric (c and d) compounds.

with most of liquid crystal materials. Its index of refraction matches that of the liquid crystal materials used throughout this work.

Glass Cleaning:

This is the most important step for making a good device. In this step, an ultrasonic cleaning bath is filled with a solution of detergent and deionized water and warmed to 40°C. After ultrasonic agitation for 1 minute, substrates are rinsed in running deionized water until no water breaks occur on the glass surface. Substrates are dried by blowing pressurized $N_2$ gas across the surface.

Alignment Coatings:

The alignment agents are applied by spin coating. The rotation speed and the duration for spinning determine the thickness of the thin film for a given solvent concentration. Usually 20 nm is a good layer thickness for a 0.2% solution. This thickness is obtained at a spin rate of 1000 rpm for 1 minute.

Baking:

Spin-coated substrates are placed on a hot plate at 120°C for 15 minutes for PVA, and at least for 2 hours for Nylon® coated-substrates. Cured parts are cooled down gradually to room temperature.

Buffing:

Substrates are lightly buffed with a short-fiber paint roller rotating on a level platform to create fine grooves in the alignment agents. An arrow is marked on the side of each substrate to indicate the rubbing direction.

Assembly:

A bottom substrate is placed on clean lens tissue with the alignment-coated-side up. Three Mylar® spacers are applied with a 120° angular separation. Spacers vary from a few microns to 10s of microns in thickness. The top substrate is then placed

coated side down on the bottom substrate so that the arrows for rubbing direction are in line and parallel. The assembled cell is then transferred to a hot plate in a class 100 laminar cleanhood. The hot plate is set to the isotropic temperature (60°C for the mixture of E7 and CB15, 85°C for the mixture of ZLI1167 and CB15) and the cell is left to thermalize for 20–30 minutes.

Liquid Crystal Filling:

A 1 cc syringe with 18 gauge needle is filled with liquid crystal material which has been heated to the isotropic temperature and degassed. The syringe is slowly inverted and the air bubble is allowed to rise to the top and expelled. The 18 gauge needle is then discarded and a 0.45 µm filter is placed on the syringe followed by a 25 gauge needle. Air in the filter is slowly expelled, pressing gently on the plunger to avoid rupturing the filter. The first few drops are discarded. Marks for rubbing direction should be away from the filling direction. The cell is filled drop-by-drop without moving the needle from the bevel edge of the substrates, keeping liquid crystal in the gap but not too much in the bevel. Capillary action spreads the fluid throughout the cell gap. When the cell is completely filled, the hot plate temperature is set to 20°C and the cell is left to cool for 30 minutes.

Shearing:

If the cell looks cloudy, the substrates are mechanically sheared along the buffing direction in a back and forth manner over a distance of 1–2 mm. This forces the alignment from focal conic to Grandjean structure. This procedure is required only in fabricating cholesteric liquid crystal devices.

Visual Inspection:

Liquid crystal devices are inspected between crossed polarizers on a light table. The thickness uniformity can be checked by seeing uniformity in color and any air

bubbles will show up as black spots. Scattering is an important thing to check for laser cavity mirror applications because it reduces transmittance.

### 1.3.4 Nomenclature for the Cholesteric Liquid Crystal Mirror

Alignment coatings play a dominant roles not only for improving alignment of the molecules but also for revealing different physical phenomena which will be discussed in Chap. 2 and 3.

For convenience, we introduce an identification code to describe different kinds of anchoring of the cholesteric liquid crystal (CLC) mirrors shown in Fig. 1.4. The format is:
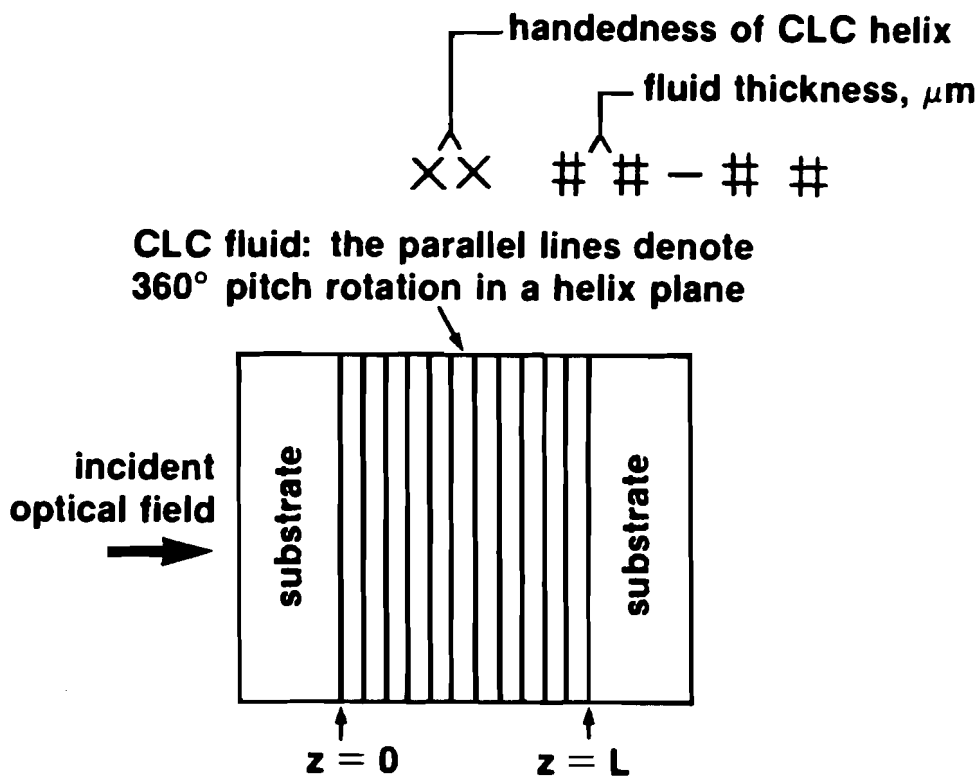


Fig. 1.4    Identification code for different anchoring schemes.

The first two characters XX indicate the handedness of the helical structure: RH (right-handed helical structure) or LH (left-handed helical structure). The next two characters ## indicate the fluid thickness in units of μm and the last two characters describe the state of anchoring at the inner substrate surfaces,

00: weak surface anchoring at both sides.

01: weak anchoring at $z = 0$, strong anchoring at $z = L$.

10: strong anchoring at $z = 0$, weak anchoring $z = L$.

11: strong anchoring at both sides.

For example, RH10–10 indicates a CLC mirror with a right-handed helix structure, 10-μm fluid thickness and a strong anchoring at $z = 0$. This CLC can also be designated as RH10–01 if the cell is flipped end-for-end in the incident beam.

**REFERENCES**

1. F. J. Kahn, "The Molecular Physics of Liquid-Crystal Devices," Phys. Today, 35, 66 (1982).

2. B. Bahadur, "Liquid Crystal Displays," Mol. Cryst. Liq. Cryst. 109, 3 (1984).

3. G. Meier, E. Sackmann, and J. G. Grabmaier, Applications of Liquid Crystals (Springer Verlag, NY, 1975).

4. See Special issue on liquid crystals, Phys. Today, 35 (1982).

5. G. W. Gary, Thermotropic Liquid Crystals in Critical Reports on Applied Chemistry (John Wiley and Sons, NY, 1987), Vol. 22, pp. 125–131.

6. D. M. Makow, "Color Properties of Liquid Crystals and Their Application to Visual Arts," Color Res. & Appl. 4, 25 (1979).

7. See Proceedings on Spatial Light Modulators and Applications II, SPIE 825.(1987)

8. A. D. McAulay, "Optical Analog to Digital Converter Using Optical Logic and Table Look–Up," Opt. Eng. 29, 114–120 (1990).

9. S. T. Wu, "Voltage-Biased Liquid Crystal Optical Power Limiters," SPIE 684, 108 (1986).

10. I. C. Khoo, R. R. Michael, and G. M. Finn, "Self-Phase Modulation and Optical Limiting of a Low-Power $CO_2$ Laser with a Nematic Liquid-Crystal Film," Appl. Phys. Lett. 52, 2108 (1988).

11. G. Labrunie and S. Valette, "Nematic Liquid Crystal Digital Light Deflector," Appl. Opt. 13, 1802 (1974).

12. S. D. Jacobs, "Liquid Crystals as Large Aperture Waveplates and Circular Polarizers," SPIE 307, 98 (1981).

13. S. D. Jacobs, "Liquid Crystal Devices for Laser Systems," J. Fusion Energy 5, 65 (1986).

14. S. D. Jacobs, K. A. Cerqua, K. L. Marshall, A. Schmid, M. J. Guardalben, and K. J. Skerrett, "Liquid-Crystal Laser Optics: Design, Fabrication, and Performance," J. Opt. Soc. Am. B 5, 1962–1979 (1988).

15. S. D. Jacobs, "Liquid Crystals for Laser Applications," Optical Materials - Properties, edited by M. J. Weber, Part 2.(CRC Press, Boca Raton, FL, 1986), pp. 409–465.

16 I. G. Chistyakov, "Liquid Crystals," Sov. Phys.-Usp. 9, 551 (1967).

17. G. Friedel, Ann. Physique 18, 273 (1922).

18. G. W Gray, K. J. Harrison, and J. A. Nash, "New Family of Nematic Liquid Crystals for Displays," Electron. Lett. 9, 130 (1973).

19. Liquid crystals are available from EM chemicals, Hawthorne, NY.

20. J. L. Janning, "Thin film surface orientation for liquid crystals" Appl. Phys. Lett. 21, 173 (1972).

21. J. M. Pollack, W. E. Haas, and J. E. Adams, " Topology of obliquely coated silicon monoxide layers," J. Appl. Phys. 48, 831 (1977).

22. L. A. Goodman, J. T. McGinn, C. H. Anderson, and F. Digeronimo, "Topography of Obliquely Evaporated Silicon Oxide Films and Its Effects on Liquid-Crystal Orientation," IEEE Trans. Electron Devices 24, 795 (1977).

# Chapter II

# Optical Properties of Cholesteric Liquid Crystals

## 2.1 Linear Optical Wave Propagation in Cholesteric Liquid Crystals

The theory of linear wave propagation in a cholesteric liquid crystal(CLC) has been well developed by Mauguin,[1] Oseen[2] and De Vries[3] and presented in various forms by others.[4,5,6] They assume that a CLC can be treated as a twisted birefringent medium whose helix axis is oriented along the z-axis as shown in Fig. 2.1. The helical structure of the CLC can be described by the director n(z) which represents the average orientation of the elongated liquid crystal molecules. Arrows within each plane indicate the director orientation, and the pitch $P_0$ is the distance required for the director to rotate by 360°. The cartesian components of the director are:

$$n_x = \cos\theta(z), \quad n_y = \sin\theta(z), \quad n_z = 0 \tag{1}$$

In the absence of external fields, the angle $\theta(z)$ is given by $\theta = q_0 z$, where $q_0$ is the unperturbed wave number of the helix whose pitch is $P_0 = 2\pi/q_0$.

The electric displacement , $\vec{D}$, of the medium is given by

$$\vec{D} = \hat{\epsilon}(z)\vec{E} = \epsilon_\perp \vec{E} + \epsilon_a \hat{n}(\hat{n} \bullet \vec{E}) \tag{2}$$

where $\epsilon_a = \epsilon_\parallel - \epsilon_\perp$ is the optical dielectric anisotropy and $\epsilon_\parallel$ and $\epsilon_\perp$ represent the dielectric constant parallel and perpendicular to the local director. The explicit form of the dielectric tensor matrix is

17

z = L

z = 0

substrate

substrate

right-handed
circularly
polarized light

$P_o$

z
y
x
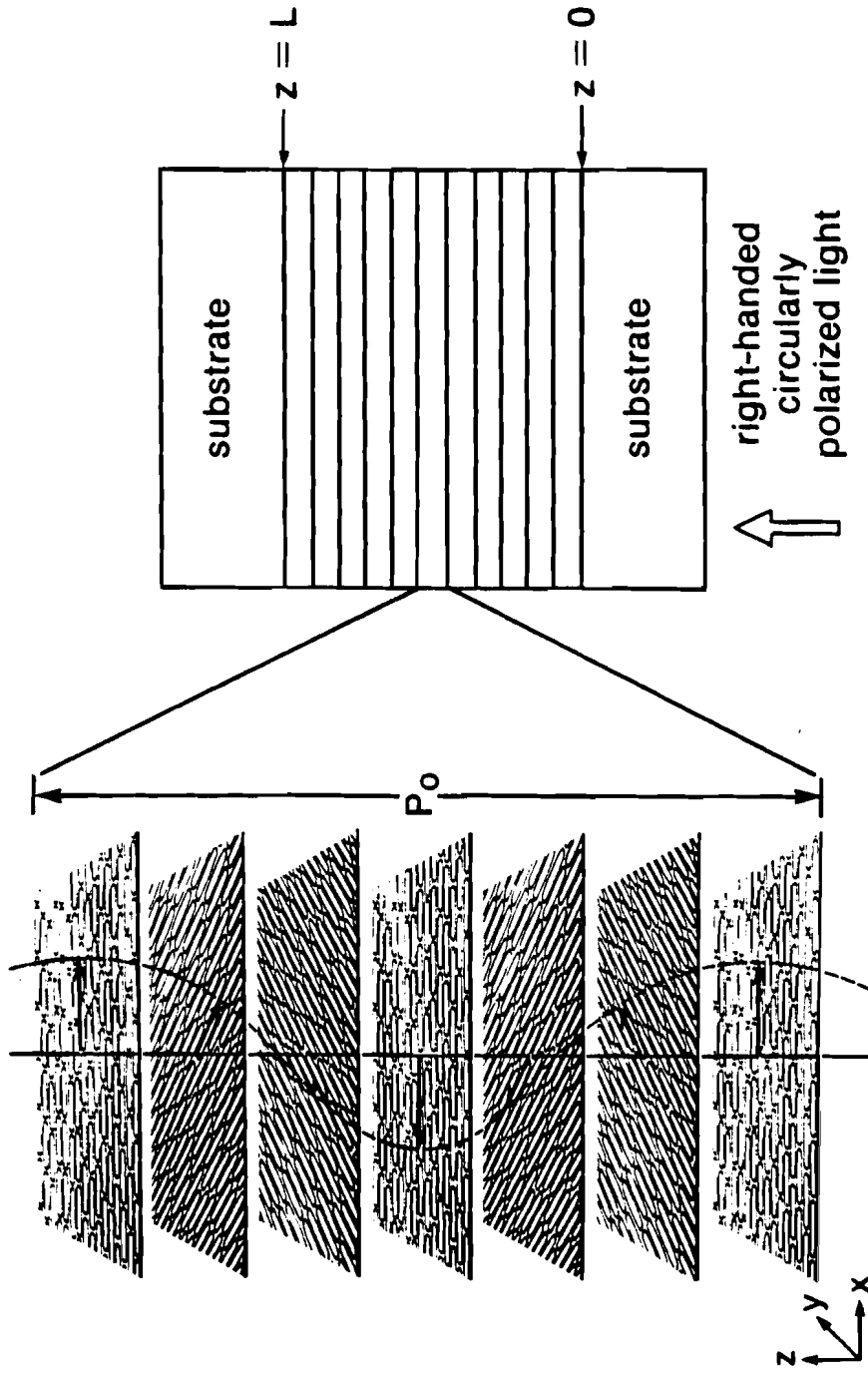
Fig. 2.1    Schematic diagram of a cholesteric liquid crystal cell.   The left-hand side of the figure shows one pitch length of the helical structure in the CLC.   Arrows within each plane indicate director orientation.

$$\hat{\epsilon}(z) = \epsilon_{av}\begin{pmatrix} 1 & 0 \\ 0 & 1 \end{pmatrix} + \frac{\epsilon_a}{2}\begin{pmatrix} \cos\theta(z) & \sin\theta(z) \\ \sin\theta(z) & -\cos\theta(z) \end{pmatrix} \tag{3}$$

where $\epsilon_{av} = (\epsilon_{\parallel} + \epsilon_{\perp})/2$ is the average dielectric constant. Because of the helicity of the medium, it is convenient to describe the electric fields in terms of circular bases, that is,

$$\vec{E} = \text{Re}\left[\left\{E_+(z)(\hat{x} - i\hat{y})/\sqrt{2} + E_-(z)(\hat{x} + i\hat{y})/\sqrt{2}\right\}e^{-i\omega t}\right] \tag{4}$$

where $E_\pm = E_x \pm iE_y$ represent the electric field amplitude of right and left circularly polarized light, respectively. Then Maxwell's equation in the medium can be rewritten as

$$-\frac{d^2E_\pm}{dz^2} = k_0^2 E_\pm + k_1^2 E_\mp e^{\pm\theta(z)} \tag{5}$$

where $k_0^2 = (\omega/c)^2 \epsilon_{av}$ and $k_1^2 = (\omega/c)^2 \epsilon_a/2$.

Let us consider a right-handed CLC where $\theta(z) = q_0 z$ [For left-handed CLC, $\theta(z) = -q_0 z$]. Then one can use the following form as a trial solution.

$$E_\pm(z) = \varepsilon_\pm e^{i(\phi \pm q_0)z} \tag{6}$$

The basic assumption in this trial solution is that the thickness of the CLC fluid is infinite. Substituting Eq. (6) into Eq. (5), we have

$$\begin{bmatrix} (\phi + q_0)^2 - k_0^2 & -k_1^2 \\ -k_1^2 & (\phi - q_0)^2 - k_0^2 \end{bmatrix} \begin{bmatrix} \epsilon_+ \\ \epsilon_- \end{bmatrix} = 0 \tag{7}$$

The two simultaneous equations have a nontrivial solution only if the corresponding determinant vanishes:

$$\left\{ (\phi + q_0)^2 - k_0^2 \right\} \left\{ (\phi - q_0)^2 - k_0^2 \right\} - k_1^4 = 0 \tag{8}$$

This fourth order equation has solutions:

$$\phi = \pm k_0 \left[ 1 + \overline{\lambda}^2 \pm \sqrt{4\overline{\lambda}^2 + \gamma^2} \right]^{\frac{1}{2}} \tag{9}$$

Here $\overline{\lambda} = \lambda / \lambda_0$ is the normalized wavelength where $\lambda_0 = \sqrt{\epsilon_{av}} \, P_0$ and $\gamma = (\epsilon_{\parallel} - \epsilon_{\perp}) / (\epsilon_{\parallel} + \epsilon_{\perp})$. The plus and minus signs in front of $k_0$ correspond to waves travelling in opposite directions along the helix.

## Selective Reflection in Wavelength and Polarization

For travelling waves, let us define the normalized wavenumber $m = \phi / k_0$.

$$m_1 = \left[ 1 + \overline{\lambda}^2 - \sqrt{4\overline{\lambda}^2 + \gamma^2} \right]^{\frac{1}{2}} \tag{10a}$$

$$m_2 = \left[ 1 + \overline{\lambda}^2 + \sqrt{4\overline{\lambda}^2 + \gamma^2} \right]^{\frac{1}{2}} \tag{10b}$$

When $\sqrt{1-\gamma} < \bar{\lambda} < \sqrt{1+\gamma}$ , $m_1$ is imaginary and the corresponding wave decrease exponentially as it propagates. Since there is no dissipative mechanism involved, it must be reflected in this wavelength region. This is the selective reflection in wavelength. For small $\gamma$, which is usually true, $\bar{\lambda} = 1$ corresponds to the selective reflection band peak wavelength and the bandwidth of the selective reflection $\Delta\lambda$ is equal to

$$\Delta\lambda = \gamma\lambda_0 \tag{11}$$

Corresponding to $m_1$ and $m_2$ solutions (say mode 1, 2 respectively), one can calculate the field amplitude ratio between right and left circularly polarized light.

$$\rho = \begin{cases} \rho_1 = \dfrac{|\varepsilon_+|}{|\varepsilon_-|} = \dfrac{\gamma^2}{(m_1-\bar{\lambda})^2 - 1} \\[4mm] \rho_2 = \dfrac{|\varepsilon_-|}{|\varepsilon_+|} = \dfrac{\gamma^2}{(m_2+\bar{\lambda})^2 - 1} \end{cases} \tag{12}$$

The plot of $\rho$ as a function of normalized wavelength for two modes is shown in Fig. 2.2. In this figure, $\rho = 0$ represents right circularly polarized light for mode 1 and left circularly polarized light for mode 2. $\rho = 1$ represents linearly polarized light. Each mode is a superposition of two components. Note that there is no place where $\rho = 0$, which represents pure circularly polarized light. When $\sqrt{1-\gamma} < \bar{\lambda} < \sqrt{1+\gamma}$, a right-handed CLC reflects right circularly polarized light ($\rho$ goes to infinity for mode 1)
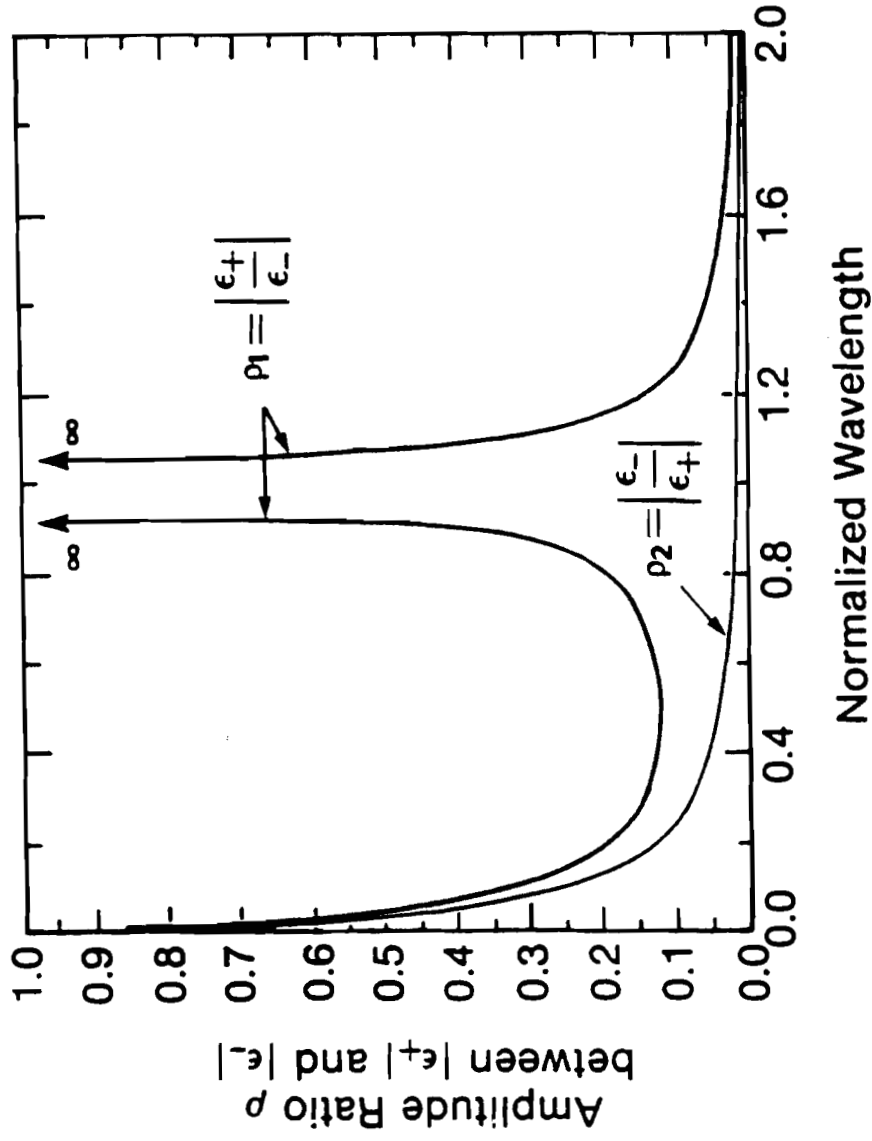
Fig. 2.2    Electric field amplitude ratio between right and left circularly polarized light as a function of a normalized wavelength for the solution of Maxwell's equation in a CLC medium ($\gamma = 0.122$).

and transmits left circularly polarized light (ρ is close to 0 for mode 2) or vice-versa for a left-handed CLC (remember that we begin with a right-handed CLC). This is the selective reflection in polarization.

## Optical Activity in CLC

For large values of $\bar{\lambda}$ , the two modes are nearly circularly polarized (where ρ is close to 0). They have opposite signs of rotation and propagate with different phase velocities. A superposition of two waves of opposite circular polarization can be thought of as a linearly polarized light wave whose plane of polarization lies along the bisector of the instantaneous angle between the two rotating vectors. Since the two circularly polarized light waves travel at different velocities in the medium, there is a net rotation of the plane of polarization when a linearly polarized wave is passed through a slab of the CLC. To show this, let us assume that linearly polarized light is incident on the slab. By using Jones notation,[7] this can be decomposed into a summation of right and left circularly polarized light as follows:

$$\begin{bmatrix} 1 \\ 0 \end{bmatrix} = \frac{1}{2}\begin{bmatrix} 1 \\ -i \end{bmatrix} + \frac{1}{2}\begin{bmatrix} 1 \\ i \end{bmatrix} \tag{13}$$

After traveling a distance L throught the medium, the complex amplitude of the wave is given by

$$\frac{1}{2}\begin{bmatrix} 1 \\ -i \end{bmatrix}e^{ik_rL} + \frac{1}{2}\begin{bmatrix} 1 \\ i \end{bmatrix}e^{ik_lL} = e^{i\left\{\frac{1}{2}(k_r + k_l)L\right\}}\begin{bmatrix} \cos\Theta \\ \sin\Theta \end{bmatrix} \tag{14}$$

where $\Theta = (k_r - k_l)L / 2$, and $k_r$ and $k_l$ are wavenumber for right and left circularly polarized light. This equation shows that a linearly polarized light is rotated with the angle $\Theta$ with respect to the original direction of polarization. From Eq. (6) and Eq. (9), the optical rotatory power per unit length $\Theta / L$ is given by

$$\frac{\Theta}{L} = q_0(1 + \frac{1}{2}\frac{m_1 - m_2}{\bar{\lambda}})$$
(15)

Especially when $4\bar{\lambda}^2 / \gamma^2 \gg 1$, $\Theta / L$ is given by

$$\frac{\Theta}{L} = -\frac{2\pi}{P}\frac{\gamma^2}{8\bar{\lambda}^2(1 - \bar{\lambda}^2)}$$
(16)

This is known as the De Vries equation.[3] In general, the medium is optically active if the dielectric tensor has conjugated imaginary off-diagonal elements.[7] By comparing between Eq. (9) and Eq. (6.128) in Ref. 7, one can rewrite the dielectric tensor in Eq. (3) as follows:

$$\begin{bmatrix} \bar{\lambda}^2 & i\sqrt{4\bar{\lambda}^2 + \gamma^2} \\ -i\sqrt{4\bar{\lambda}^2 + \gamma^2} & \bar{\lambda}^2 \end{bmatrix}$$
(17)

This shows that the CLC is a special case of an optically active medium whose optical activity comes from the helical structure.

## Reflectivity of CLC

When right circularly polarized light with wavelength $\lambda$ (close to $\lambda_0$) is incident on a right-handed CLC at normal incidence, the total electric field $\vec{E}$ in the medium can be described by the summation of a forward-propagating wave and a counter-propagating wave, which has the same sense of polarization as the forward-propagating wave as follows:

$$\vec{E} = \text{Re}\left[\left\{E_+(z)(\hat{x} - i\hat{y})/\sqrt{2} + E_-(z)(\hat{x} + i\hat{y})/\sqrt{2}\right\}e^{-i\omega t}\right] \tag{18}$$

This equation is the same as Eq. (4). This is because the mathematical notations for the forward-propagating, left circularly polarized light and the counter-propagating, right circularly polarized light are same. Therefore the same Maxwell's equation in Eq. (5) can be used. As a trial solution, the forward-propagating and counter-propagating waves can be represented as

$$E_\pm(z) = \varepsilon_\pm(z)e^{\pm ik_0 z} \tag{19}$$

In a slowly varying amplitude approximation, Maxwell's equation in Eq. (5) can be rewritten as a coupled amplitude equation[9]

$$\frac{d\varepsilon_+(z)}{dz} = i\kappa\varepsilon_{-(z)}e^{-i2\delta z} \tag{20a}$$

$$\frac{d\varepsilon_-(z)}{dz} = -i\kappa\varepsilon_{+(z)}e^{i2\delta z} \tag{20b}$$

where $\kappa = k_1^2 / 2k_0 = (\omega / c)(\epsilon_a / 4\sqrt{\epsilon_{av}})$ is the coupling coefficient and $\delta = k_0\text{-}q_0$ is the detuning parameter. In order to solve Eqs. (20), let $\epsilon_+(z) = R(z)e^{-i\delta z}$ and $\epsilon_-(z) = S(z)e^{i\delta z}$.

$$\frac{dR}{dz} - i\delta R(z) = i\kappa S(z) \tag{21a}$$

$$\frac{dS}{dz} + i\delta S(z) = -i\kappa R(z) \tag{21b}$$

Once again, let $R = F \cdot \sinh(\sigma z) + G \cdot \cosh(\sigma z)$ and $S = C \cdot \sinh(\sigma z) + D \cdot \cosh(\sigma z)$. Applying the boundary conditions at $z = 0$ and at $z = L$, that is, $\epsilon_+(z = 0) = \epsilon_+(0)$ and $\epsilon_-(z = L) = 0$ (where L is the CLC fluid thickness), we have

$$\epsilon_+(z) = \epsilon_+(0)\left[\frac{\sigma\cosh\{\sigma(L-z)\} - i\delta\sinh\{\sigma(L-z)\}}{\sigma\cosh(\sigma L) - i\delta\sinh(\sigma L)}\right]e^{-i\delta z} \tag{22a}$$

$$\epsilon_-(z) = \epsilon_+(0)\left[\frac{i\kappa\sinh\{\sigma(L-z)\}}{\sigma\cosh(\sigma L) - i\delta\sinh(\sigma L)}\right]e^{i\delta z} \tag{22b}$$

where $\sigma^2 = \kappa^2 - \delta^2$. The reflectivity of a CLC is defined as

$$R = \left|\frac{E_-(0)}{E_+(0)}\right|^2 = \frac{\sinh^2(\sigma L)}{\cosh^2(\sigma L) - (\delta / \kappa)^2} \tag{23}$$

When $\delta = 0$, that is, when the CLC structure is well phase (Bragg)-matched with the input wavelength, then

$$R = \tanh^2(\kappa_0 L) \tag{24}$$

The reflectivity R as a function of $\kappa_0 L$ is plotted in Fig. 2.3.

Since $\sqrt{\epsilon_a} \cong n_{av}$, the coupling coefficient $\kappa$, the detuning parameter $\delta/\kappa$, and the normalized wavelength $\bar{\lambda}$ can be simplified and rewritten as follows:

$$\kappa = \frac{\pi}{\lambda} \Delta n \tag{25}$$

$$\frac{\delta}{\kappa} = \frac{4 n_{av}}{\Delta n}(1 - \bar{\lambda}) \tag{26}$$

$$\bar{\lambda} = n_{av} P_0 \tag{27}$$

where $\Delta n = n_e - n_o$ is the optical birefringence, $n_{av} = (n_o + n_e)/2$, and $n_e$ and $n_o$ represent extra-ordinary and ordinary refractive indices, respectively, of the nematic substructure in the CLC.

A plot of reflectivity R as a function of $\bar{\lambda}$ for $\kappa_0 L = 4.59$ is shown in Fig. 2.4. It can be seen that when $\bar{\lambda} = 1.076$, the reflectivity of the CLC goes to zero. The ripples in this figure are due to phase mismatching. Let us define the bandwidth $\Delta\lambda$ as the wavelength difference between the first zeros. From Eq. (23), the bandwidth $\Delta\lambda$ is given by

$$\Delta\lambda = 2\frac{\sqrt{1 - (1 - \gamma^2/4)\left\{1 - (P_0/2L)^2\right\}}}{1 - (P_0/2L)^2}\lambda_0 \tag{28}$$
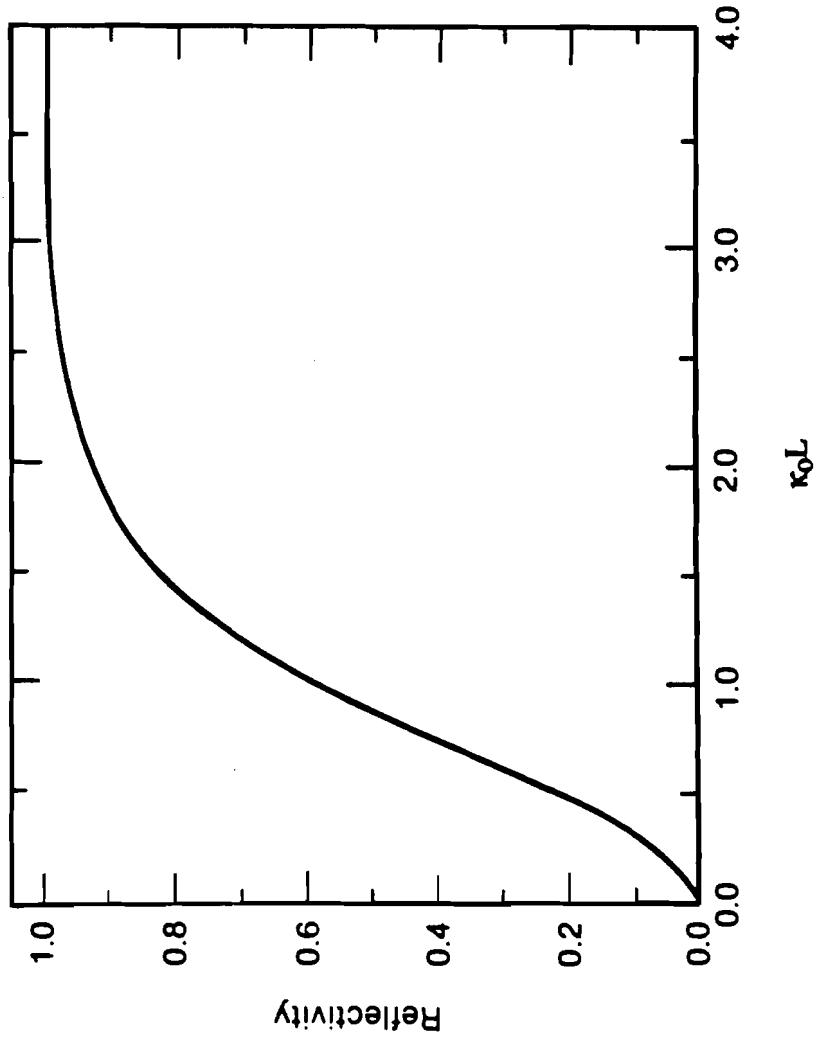
Fig. 2.3    Reflectivity R, in a CLC cell, as a function of $\kappa_0 L$ where $\kappa_0$ is the coupling coeffieient and L is the CLC fluid thickness.
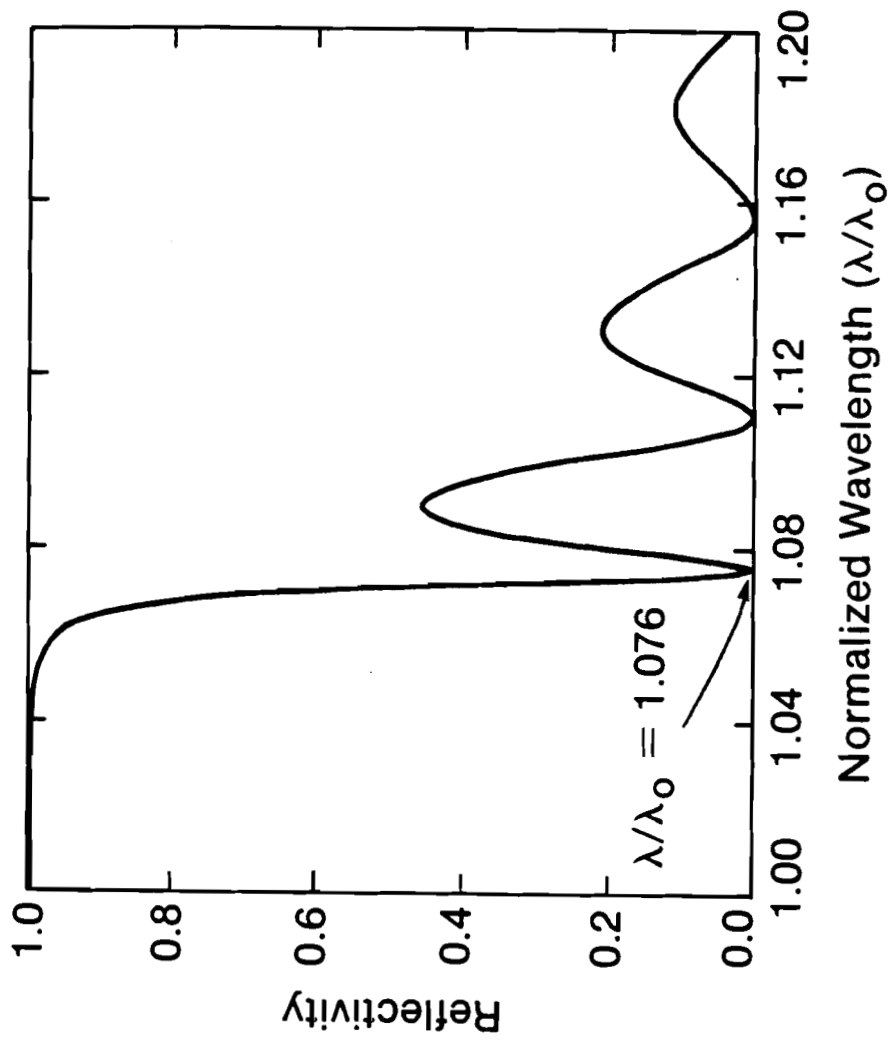
Fig. 2.4    Reflectivity R as a function of normalized wavelength $\lambda/\lambda_o$ for $\kappa_0 L = 4.59$.

Note that the bandwidth of the selective reflection depends on the thickness. When the thickness L goes to infinity, the selective reflection bandwidth reduces to Eq. (29).

$$\Delta\lambda = \frac{\Delta n}{n_{av}}\lambda_o \qquad (29)$$

It shows that the bandwidth is proportional to birefringence.

## 2.2 Nonlinear Effects in Cholesteric Liquid Crystals[10,11]

In the previous section, the linear propagation of light through the medium was discussed. There, the changes of the liquid crystal helical structure due to the presence of an optical field were almost negligible. But in intense optical fields, the helical structure can be changed and nonlinear effects can occur. The anchoring conditions between substrates and CLC fluid play a dominant role. In 1982, H. G. Winful[12] solved the coupled Euler-Lagrange and Maxwell's equations to show theoretically how optical bistability develops as a result of pitch dilation in a CLC with strong anchoring at the input side. We now show theoretically[10] that under exposure to a plane wave with a Gaussian intensity distribution, a retro-self-focusing effect occurs in which the reflected field comes to a focus. In addition, we discuss how the anchoring conditions affect the helical structure in a CLC.[11] The retro-self-focusing effect will be experimentally proven in Chap. 3

In an optical field $\vec{E}$, the new orientation of the director $\theta(z)$ in Eq. (5) can be found by minimizing the free energy F

$$F = \int_V d^3r \frac{1}{2}\left\{ k_{11}(\nabla\cdot\hat{n})^2 + k_{22}(\hat{n}\cdot\nabla \times \hat{n} + q_0)^2 + k_{33}(\hat{n} \times \nabla \times \hat{n})^2 - \vec{E}\cdot\vec{D}/4\pi \right\} \qquad (30)$$

where $k_{11}$, $k_{22}$, and $k_{33}$ are the Frank elastic constants in units of dyne that describe the basic distortions of splay, twist, and bend, respectively. In the case of a CLC which has a planar structure with the components of the director as given in Eq. (1), the first and third terms in Eq. (30) disappear and only the second term remains. This leads to the Euler-Lagrange equation of motion for the director angle $\theta(z)$:

$$\frac{d^2\theta}{dz^2} = \frac{\epsilon_a}{16\pi k_{22}} \left[ \text{Re}(E_+ E_-^*) \sin2\theta - \text{Im}(E_+ E_-^*) \cos2\theta \right] \tag{31}$$

As a trial solution for Maxwell's equation in Eq. (5), the forward-propagating and counter-propagating fields can be represented as

$$E_\pm = \left| \epsilon_\pm(z) \right| \exp \left[ i\phi_\pm(z) \pm iq_0 z \right] \tag{32}$$

By substituting Eq. (32) into Eq. (5), Maxwell's equation is reduced to a coupled amplitude equation within the slowly-varying-envelope approximation

$$\frac{d|\epsilon_+|}{dz} = \kappa |\epsilon_-| \sin\Psi \tag{33a}$$

$$\frac{d|\epsilon_-|}{dz} = \kappa |\epsilon_+| \sin\Psi \tag{33b}$$

$$\frac{d\Psi}{dz} = 2(q_0 + \Delta k) + \kappa \left( \frac{|\epsilon_-|}{|\epsilon_+|} + \frac{|\epsilon_+|}{|\epsilon_-|} \right) \cos\Psi - 2\frac{d\theta}{dz} \tag{33c}$$

where $\Psi(z) = \phi_+(z) - \phi_-(z) + 2q_0 z - 2\theta(z)$, the coupling coefficient $\kappa = k_1^2/2q_0$, and the detuning parameter $\Delta k = (k_0^2 - q_0^2)/2q_0$. This $\Delta k$ is slightly different from the detuning parameter defined in Eqs. (20). But when $k_0$ is close to $q_0$, $\Delta k = \delta$. We now proceed to solve Eqs. (33) for different boundary conditions.

## CLC-01 Case (Weak Anchoring/Strong Anchoring)

For this case, the boundary conditions required are as follows:

$$|\epsilon_+(L)| = |\epsilon_T|, \quad \text{transmitted field at } z = L \tag{34a}$$

$$|\epsilon_-(L)| = 0, \quad \text{no reflection at } z = L \tag{34b}$$

$$\theta(L) = 0, \quad \text{strong anchoring at } z = L \tag{34c}$$

$$\left.\frac{d\theta}{dz}\right|_{z=0} = q_0, \quad \text{weak anchoring at } z = 0 \tag{34d}$$

Substituting Eq. (32) into Eq. (31), we have

$$\frac{d^2\theta}{dz^2} = \frac{\epsilon_a}{16\pi k_{22}\kappa} \frac{d|\epsilon_+|^2}{dz} \tag{35}$$

Integration of Eq. (35) with the boundary condition in Eq. (34d), gives

$$q(z) = q_0 - \frac{\epsilon_a}{16\pi k_{22}\kappa} (|\epsilon_+(z)|^2 - |\epsilon_+(0)|^2) \tag{36}$$

Since $|\varepsilon_+(0)|^2 > |\varepsilon_+(z)|^2$, $q(z) > q_0$, that is, pitch contraction will occur.

## CLC-10 Case (Strong Anchoring/Weak Anchoring)

This case was discussed by H. G. Winful.[12] For this case, the boundary condition in Eq. (34d) is changed

$$\frac{d\theta}{dz}\bigg|_{z=L} = q_0, \text{ weak anchoring at } z = L \tag{37}$$

This boundary condition leads to

$$q(z) = \frac{d\theta}{dz} = q_0 - \frac{\epsilon_a}{16\pi k_{22}\kappa}\left(|\varepsilon_+(z)|^2 - |\varepsilon_T|^2\right) \tag{38}$$

Since $|\varepsilon_+(z)|^2 > |\varepsilon_T|^2$, $q(z) < q_0$. In other words, the pitch dilates in proportion to the local field intensity. The maximum dilation occurs around $z = 0$. From Eqs. (33) and (38), we find

$$\frac{d}{dz}\left(|\varepsilon_+\varepsilon_-|\cos\Psi\right) = -\frac{1}{\kappa}\frac{d|\varepsilon_+|^2}{dz}\left[\Delta k + \frac{\epsilon_a}{16\pi k_{22}\kappa}\left(|\varepsilon_+|^2 - |\varepsilon_-|^2\right)\right] \tag{39}$$

Let $u(z) = \beta |\varepsilon_+(z)|^2$, $J = \beta |\varepsilon_T|^2$ and $v(z) = \beta |\varepsilon_-(z)|^2$, where $\beta = \epsilon_a/32\pi k_{22}\kappa^2$. Rewriting Eq. (39), we have

$$\frac{d}{dz}\sqrt{uv}\cos\Psi = -\left[\frac{\Delta k}{\kappa} + 2(u - J)\right]\frac{du}{dz} \tag{40}$$

Integrating Eq. (40) with respect to z gives

$$\sqrt{uv}\cos\Psi = -\left(\frac{\Delta k}{\kappa} - 2J\right)u - u^2 + C \qquad (41)$$

Where C is a constant of integration. From the boundary conditions, Eq. (34a) and Eq. (34b), u(L) = J and v(L) = 0 respectively, and the solution for Eq. (40) takes the form

$$\sqrt{uv}\cos\Psi = -(u-J)\left(\frac{\Delta k}{\kappa} + u - J\right) \qquad (42)$$

Since $d\,|\varepsilon_+|/dz < 0$ in Eq. (33a), $\sin\Psi < 0$.

Therefore Eq. (42) becomes

$$\sin\Psi = -\left[1 - (1\text{-}J/u)\left\{\Delta k/\kappa + (u\text{-}J)\right\}^2\right]^{1/2} \qquad (43)$$

If we now multiply Eq. (33a) by $|\varepsilon_+|$ and rearrange it, we have

$$\frac{d}{dz}|\varepsilon_+|^2 = 2\kappa\,|\varepsilon_+\varepsilon_-|\sin\Psi \qquad (44)$$

Substituting Eq. (43) into Eq. (44), one finds

$$\frac{du}{dz} = -2\kappa\left[(u\text{-}J)\left\{u - (u\text{-}J)[\Delta k/\kappa + (u\text{-}J)]^2\right\}\right]^{1/2} \qquad (45)$$

$$= -2\kappa\,[Q(u)]^{1/2}$$

where $Q(u) = (u-J) \{u-(u-J)(\Delta k/\kappa + u-J)^2\}$.

When the roots of $Q(u)$ are real and $u_1 > u_2 > u_3 > u_4$, Eq. (45) may be solved in terms of a Jacobian elliptic function[13]:

$$u(z) = u_3 + \frac{u_2 - u_3}{1-(u_1-u_2)(u_1-u_3)^{-1}Sn^2\,[2\kappa(z-L)/g,k]} \qquad (46)$$

where Sn is a Jacobian elliptic function with $g = 2/[(u_1-u_3)(u_2-u_4)]^{1/2}$ and $k = [(u_1-u_2)(u_3-u_4)]^{1/2}\,g/2$. When the two roots of $Q(u)$ are real and $u_1 \geq u \geq u_2$ and the two roots $u_3$ and $u_4$ are complex, the solution of Eq. (45) becomes

$$u(z) = \frac{Bu_1 + Au_2 + (Au_2 - Bu_1)\,Cn[2\kappa(z-L)/g, k]}{A+B+(A-B)\,Cn\,[2\kappa(z-L)/g, k]} \qquad (47)$$

where $A^2 = (u_1 - b_1)^2 + b_2^2$, $B^2 = (u_2-b_1)^2 + b_2^2$, $b_1 = Re[u_3]$ and $b_2 = Imag\,[u_3]$, and Cn is a Jacobian elliptic function with $g = 1/\sqrt{AB}$ and $b_2 = \{(u_1-u_2)^2 - (A-B)^2\}/4AB$.

A plot of the normalized intensity $u(z)$ for the forward propagating wave and $v(z)$ for the counter propagating wave in the CLC medium is shown in Fig. 2.5. The incident field intensity $u(z)$ decays almost exponentially along the z-axis. This decay,
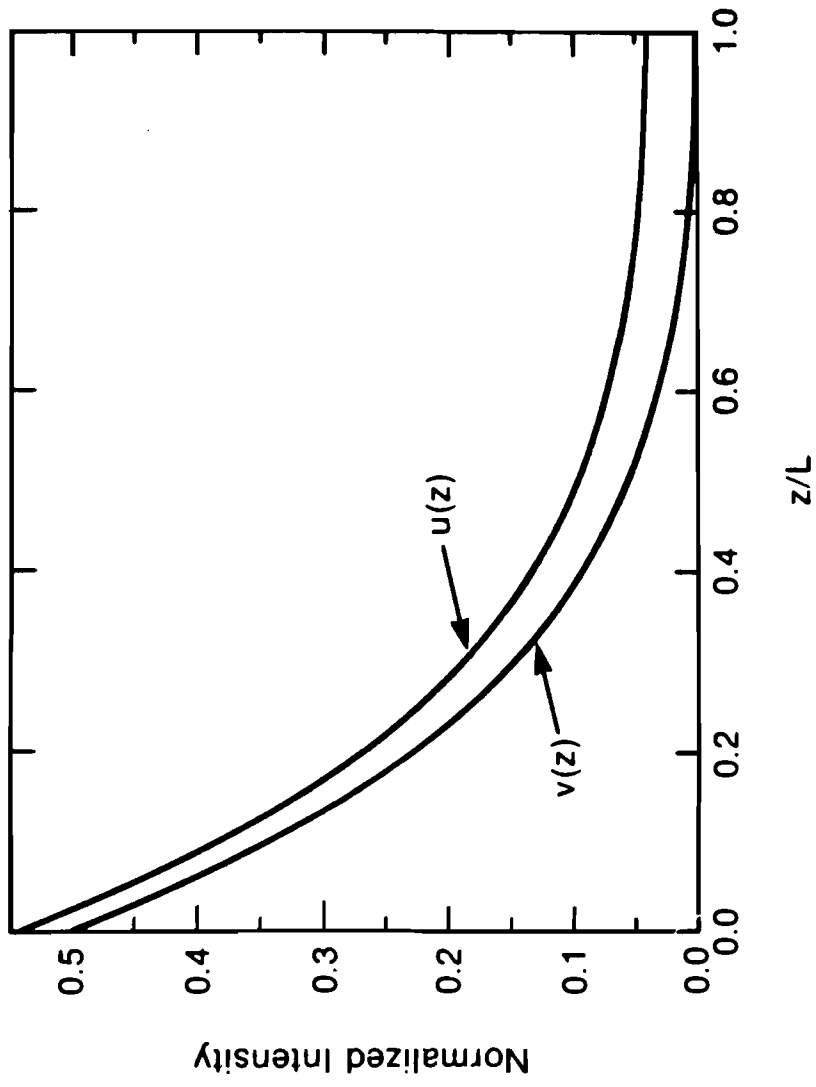
Fig. 2.5    Normalized forward propagating field intensity u(z) and counter propagating field v(z) through the medium, for κL = 2.0.

however, is due to energy transfer to the counter-propagating field, and not due to absorption. The relationship between incident field intensity I at z = 0 and transmitted field intensity J at z = L for $\kappa L = 2$ with $\Delta k/\kappa = 0, \pm 0.1$ is shown in Fig. 2.6. As H. G. Winful has already shown, optical bistability is predicted. Higher ($\Delta k/\kappa < 0$, that is, $\lambda > \lambda_0$ ) and lower ($\Delta k/\kappa > 0$, that is, $\lambda < \lambda_0$ ) intensities are required for a discontinuous jump in comparison to the case where $\Delta k/\kappa = 0$. Physically, $\Delta k/\kappa = 0$ means that the pitch of a CLC is exactly Bragg-matched to the wavelength of an incident field .

Now let us calculate the phase $\phi_-(z)$ of the reflected wave at z = 0. At z = 0, $\psi = \phi_+(0) - \phi_-(0)$. From Eq. (43),

$$\phi_-(0) = \phi_+(0) - \cos^{-1}\left[-\sqrt{1-J/I}\left\{\Delta k/\kappa + I - J\right\}\right] \qquad (48)$$

where I = u(0). Equation (48) shows explicitly the intensity dependence of the phase shift. Figure 2.7 shows the phase of the reflected wave as a function of normalized input intensity and the detuning parameter $\Delta k/\kappa$ when $\phi_+(0) = 0$. When $\Delta k/\kappa = 0$, the intense field destroys the Bragg condition $\lambda_0 = n_{av} \cdot P_0$ and the phase linearly decreases from 90° for the director distribution in Fig. 2.1 as the input field intensity increases. {For n(z) = [cos θ(z), -sinθ(z), 0], it decreases from 0°.} This agrees with the fact that the reflected field introduces a 90° phase shift in the weak field regime [see Eq. (22b)]. When $\Delta k/\kappa < 0$, the pitch dilates as the input intensity increases, and at a certain intensity the incident field satisfies the Bragg condition. In Fig. 2.7, when $\Delta k/\kappa = -0.1$, the phase of the reflected field increases with intensity from ~83° to 90° where the Bragg condition is met. The phase then decreases for higher intensity levels.
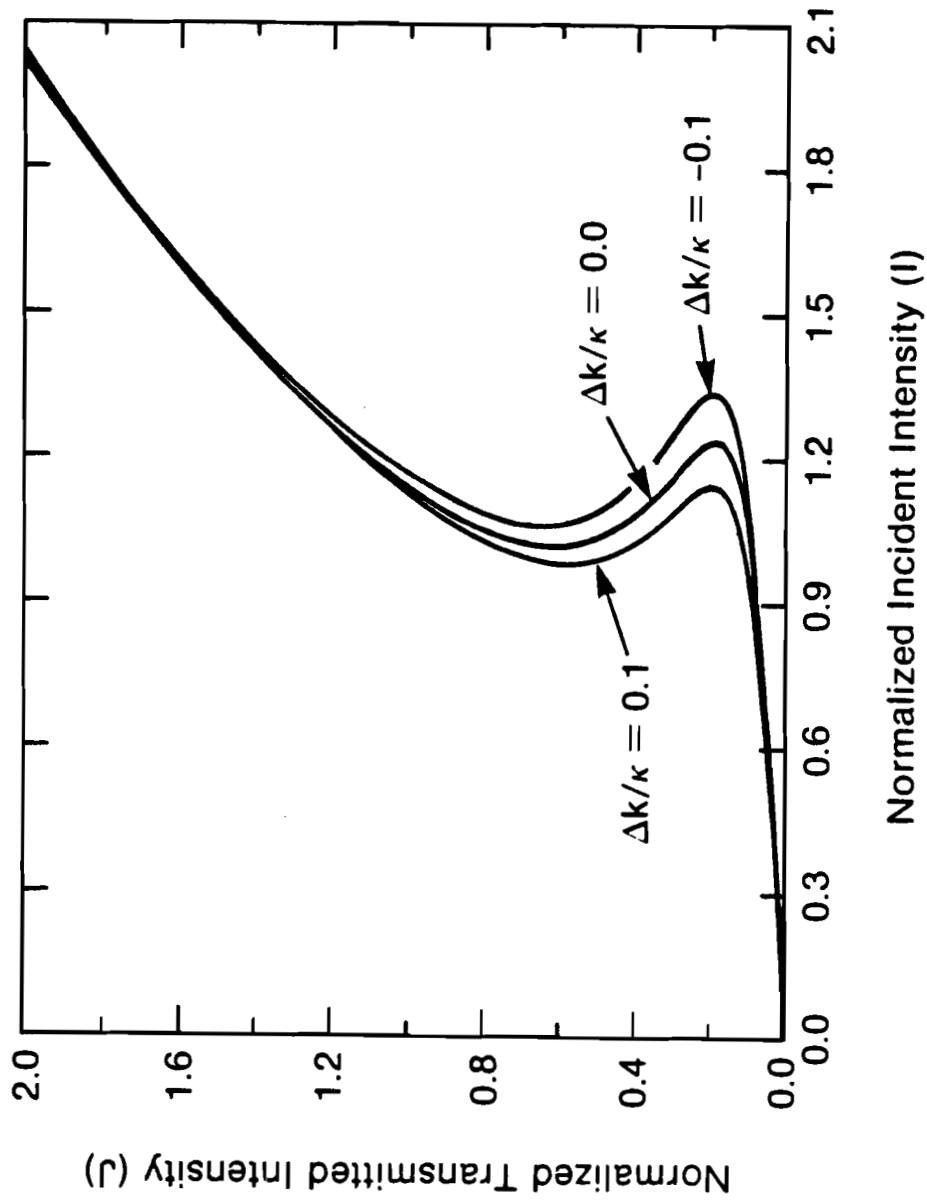
Fig. 2.6    Transmitted intensity J versus input intensity I for $\kappa L = 2.0$ for various values of the detuning parameter $\Delta k/\kappa = 0, \pm 0.1$. Intensities are normalized by $32\pi k_2 2\kappa^2/\epsilon_a$.
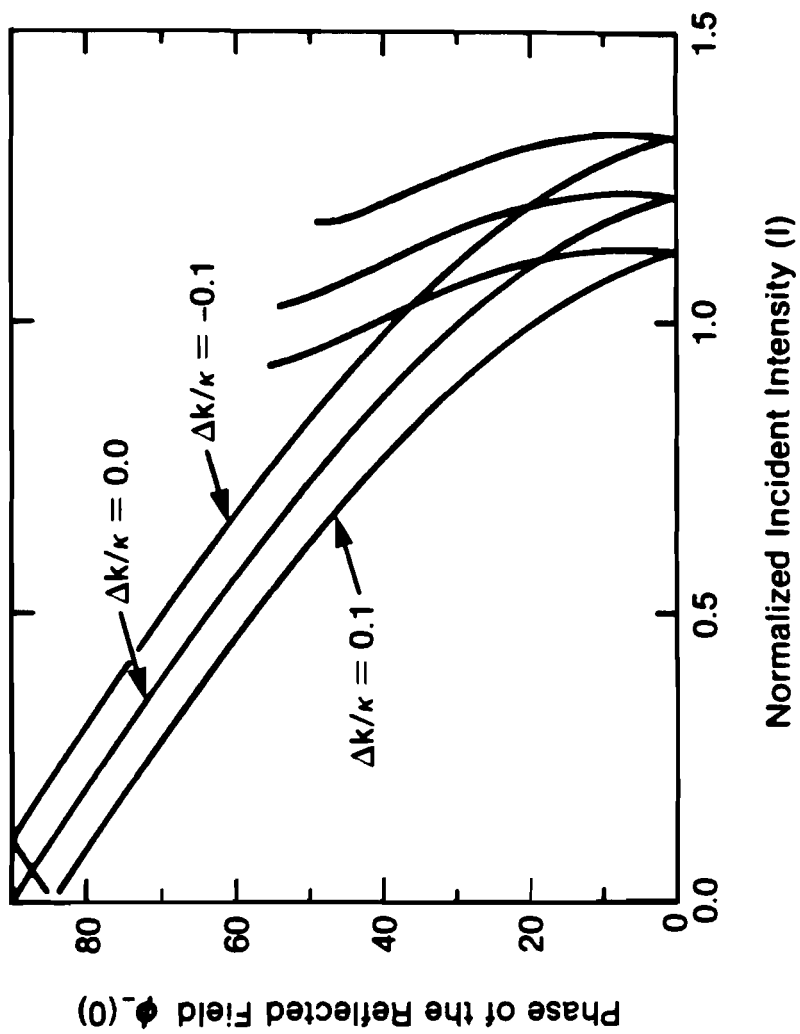
**Fig. 2.7**    Incident field intensity vs the phase of the reflected field when the phase of the reflected field $\phi_+(0) = 0$. (For $\kappa L = 2.0$ and for various values of the detuning parameter $\Delta k/\kappa = 0, \pm 0.1$ )

When $\Delta k/\kappa > 0$, the pitch of the CLC is already out of the Bragg condition. Its initial phase is less than $90°$ and it decreases with increasing intensity. The physical origin of this intensity dependence of the phase of a reflected field is as follows: higher field intensities cause a larger pitch dilation (for the CLC with $\epsilon_a > 0$). As a result, the Bragg reflection condition is perturbed and the optical field penetrates more deeply into the CLC before being reflected.

Now let us consider a plane wave with a Gaussian intensity distribution incident on the CLC. In a first approximation, we can apply our plane wave consideration to study the transverse effects. A very interesting condition results from considering a plane wave with a Gaussian distribution of the intensity $I_p$ in Eq. (49).

$$I_p = \left| \frac{ncE_o}{8\pi} \exp\left( -\frac{r^2}{w^2} \right) \right|^2 = I_o \exp\left( -\frac{2r^2}{w^2} \right) \tag{49}$$

where w is the spot size of the beam, n is the refractive index of the material and c is the velocity of light. Rewriting this as a normalized intensity with $\beta$ and introducing a radial-dependence, one finds

$$u(z = 0) = \beta |E(r,0)|^2 = \beta |E_o|^2 \exp\left( -\frac{2r^2}{w^2} \right) \tag{50}$$

By substituting Eq. (50) into Eq. (48), one derives the transverse phase shift of the reflected wave due to a Gaussian intensity distribution. In the first approximation, it is assumed that the first and third terms in Eq. (30) are still negligible. For $I \gg J$, i.e., for the lower-branch condition in the bistability curve of Fig. 2.6, Eq. (48) reduces to

$$\phi_-(0) = \phi_+(0) + \frac{\pi}{2} + \sqrt{1 - \frac{J}{I}} \left\{ \frac{\Delta k}{\kappa} + I - J \right\}$$

$$\approx \phi_+(0) + \frac{\pi}{2} + \frac{\Delta k}{\kappa} + I \qquad \text{when} \quad \left| \frac{\Delta k}{\kappa} + I \right| < 1 \qquad (51)$$

One can now readily derive the phase distribution of the reflected field,

$$\phi_-(0) \approx \left\{ \phi_+(0) + \frac{\pi}{2} + \frac{\Delta k}{\kappa} + \beta |E_o|^2 \right\} - \frac{2\beta |E_o|^2 r^2}{w^2} + \frac{4\beta |E_o|^2 r^4}{w^4} - \qquad (52)$$

The first term of Eq. (52) corresponds to the constant phase change. The second term corresponds to the quadratic phase change, and the third term corresponds to a spherical aberration ($r^4$ dependence). By analogy with the quadratic phase term of a Gaussian beam, we can calculate the intensity dependent radius of curvature of the reflected field as

$$R_{CLC} = \frac{-\pi w^2}{\lambda} \frac{1}{2\beta |E_o|^2} \qquad (53)$$

Equation (53) indicates a retro-self-focusing effect because the radius of curvature is negative and inversely proportional to the intensity as we expect. Several situations are described in Fig. 2.8. When $\Delta k/\kappa < 0$ and the shift of the selective-reflection peak wavelength $\lambda_o$ ($= n_{av} P_o$) due to the maximum pitch dilation at the center of the beam is less than the laser wavelength $\lambda_{laser}$, the CLC acts as a convex mirror [Fig. 2.8(a)].

42
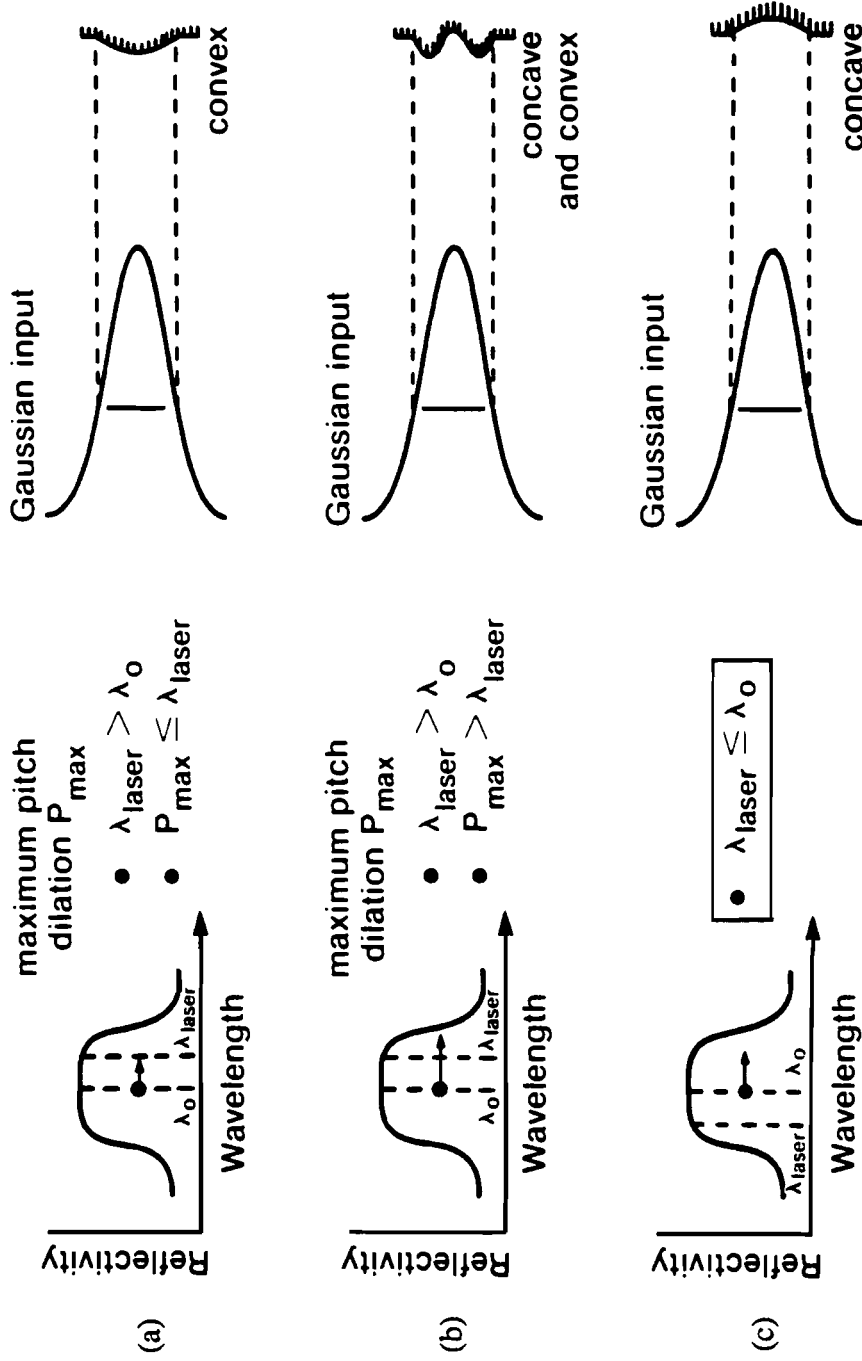


Fig. 2.8  The transverse curvature modulation of the CLC mirror by the incident Gaussian intensity distribution for different detuning conditions.

When $\Delta k/\kappa \geq 0$ and the maximum pitch dilation is restricted to the selective-reflection band, the phase of the reflected field lags as the intensity increases. Then CLC acts as a concave mirror causing a retro-self-focusing effect [Fig. 2.8(c)]. When $\Delta k/\kappa < 0$ and the shifted selective-reflection peak wavelength $\lambda_0$ is greater than the laser wavelength $\lambda_{laser}$, the CLC acts as a combination of concave and convex mirrors [Fig. 2.8(b)]. The radius of curvature of the CLC mirror depends on the location of the selective reflection peak wavelength $\lambda_0$ relative to the laser wavelength $\lambda_{laser}$ and on the maximum intensity of the incident field.

## CLC-11 Case (Strong Anchoring/Strong Anchoring)

For a CLC-11, the following boundary conditions are required.

$$| \varepsilon_+(L)| = | \varepsilon_T| , \quad \text{the transmitted field amplitude at } z = L \tag{54a}$$

$$| \varepsilon_-(L)| = 0, \quad \text{no reflection at } z = L \tag{54b}$$

$$\theta(0) = 0, \quad \text{the director angle at } z = 0 \tag{54c}$$

$$\theta(L) = q_0 L, \quad \text{the director angle at } z = L \tag{54d}$$

In addition to the above boundary conditions, the helix wave number should be equal to $q_0$ at some point $z = a$ inside the medium, that is,

$$q(z = a) = \left. \frac{d\theta}{dz} \right|_{z = a} = q_0 . \tag{54e}$$

Integration of Eq. (35) with the boundary condition in Eq. (54e), gives

$$q(z) = q_0 - \frac{\epsilon_a}{16\pi k_{22}\kappa} \left\{ |\epsilon_+(z)|^2 - |\epsilon_+(a)|^2 \right\} \tag{55}$$

When $0 \leq z < a$, $q(z) < q_0$, that is, the pitch dilates in proportion to the optical field intensity ($\epsilon_a > 0$) and $q(z) = q_0$ at $z = a$. When $a < z \leq L$, $q(z) > q_0$, that is, pitch contraction occurs. Therefore pitch dilation and contraction occur simultaneously in a CLC-11. From Eqs. (33) and Eq.(55), we find

$$\frac{d}{dz}(|\epsilon_+\epsilon_-|\cos\Psi) = -\frac{1}{\kappa}\frac{d|\epsilon_+|^2}{dz}\left[\Delta k + \frac{\epsilon_a}{16\pi k_{22}\kappa}\left(|\epsilon_+(z)|^2 - |\epsilon_+(a)|^2\right)\right] \tag{56}$$

Let $u(z) = \beta|\epsilon_+(z)|^2$, $J = \beta|\epsilon_T|^2$, $S = \beta|\epsilon_+(a)|^2$, and $v(z) = \beta|\epsilon_-(z)|^2$ where $\beta = \epsilon_a/32\pi k_{22}\kappa^2$.

From the boundary conditions Eq. (54a) and (54b), $u(L) = J$ and $v(L) = 0$ respectively. Then Eq. (56) becomes

$$\sqrt{uv}\cos\Psi = -(u-J)\{\Delta k/\kappa - 2s + u + J\}. \tag{57}$$

Multiplying Eq. (33) by $|\epsilon_+(z)|$ and rearranging it, we have

$$\frac{d|\epsilon_+|^2}{dz} = 2\kappa|\epsilon_+\epsilon_-|\sin\Psi \tag{58}$$

Substituting Eq. (57) into Eq. (58), one finds

$$\frac{du}{dz} = -2\kappa\sqrt{Q(u)} \tag{59}$$

where $Q(u) = (u - J) \{u - (u - J) (\Delta k/\kappa - 2S + u + J)^2\}$.

Integrating Eq. (55) and using the boundary condition in Eq. (54c), we have

$$\theta(z) = (q_0 + 2\kappa S)z - 2\kappa \int_0^z u(z)dz \; . \tag{60}$$

The boundary condition $\theta(L) = q_0 L$ in Eq. (54d) provides a means to calculate the normalized intensity S in Eq. (59), as follows:

$$S = \frac{1}{L} \int_0^L u(z)dz \; . \tag{61}$$

The physical interpretation of S is the average normalized intensity in the medium, where the helix wave number is equal to $q_0$.

The solution of Eq. (54) may be given in terms of a Jacobian elliptic function[8] as shown in Eq. (46) and Eq. (47).

A plot of the normalized intensity u(z) for the forward-propagating wave in the CLC medium is shown in Fig. 2.9. In this figure, $\kappa L = 2.0$, $q_0 L = 10\pi$, and $J = 0.08$. The solid lines represent the normalized intensity u(z) for CLC-11. The incident field intensity u(z) decays almost exponentially along the z-axis. The dotted
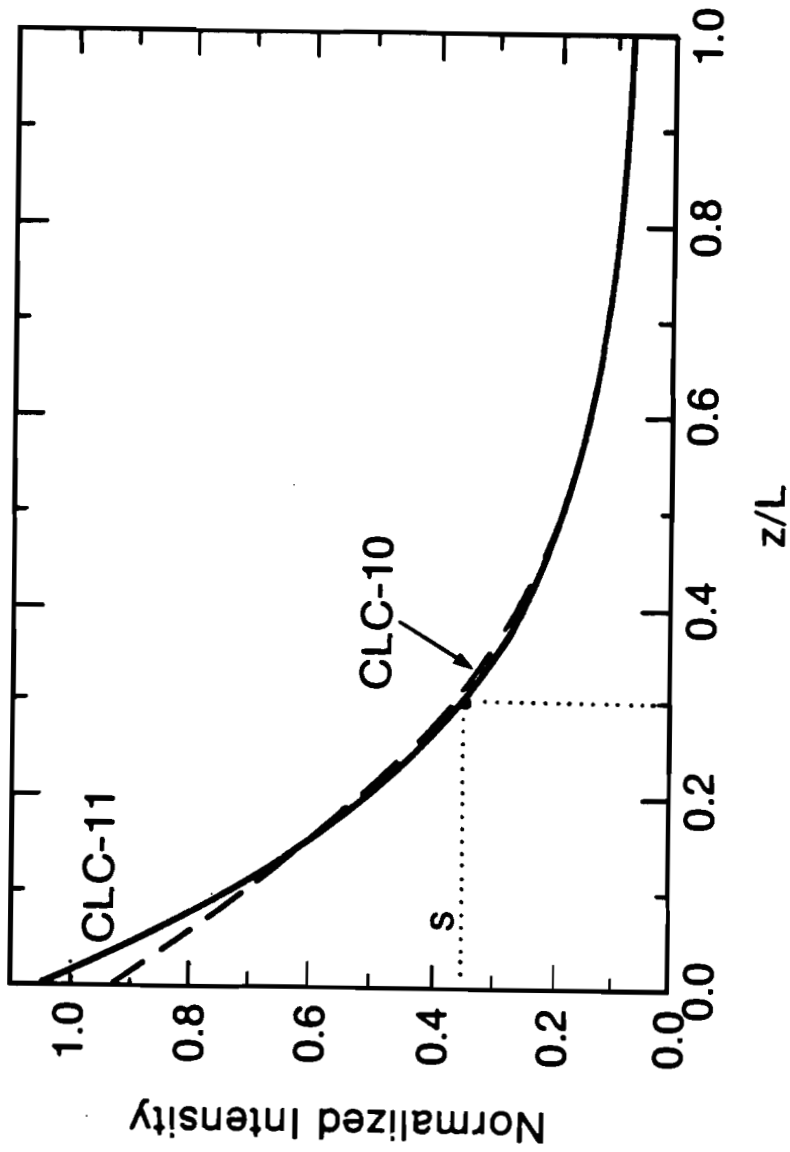
Fig. 2.9    Normalized forward propagating field intensity u(z) through the medium for $\kappa L = 2.0$, $q_0 L = 10\pi$ at normalized transmitted intensity $J = 0.08$. Solid lines represent CLC-11 case and dashed lines represent a CLC-10 case.

lines represent the normalized intensity u(z) for CLC-10. Additional input intensity is required to have the same transmitted intensity J for CLC-11 because the strong anchoring at z = L impedes the helical structure from changing. The value S on the ordinate represents the average normalized intensity in the medium, where the helix wave number of the CLC equals $q_o$.

The relationship between normalized input intensity I and normalized transmitted intensity J for $\kappa L = 2.0$ with $\Delta k/\kappa = 0$ and $q_o L = 10\,\pi$ is shown in Fig. 2.10. For the case of CLC-10, the optical bistability results. However, this nonlinearity disappears in the same range of normalized input intensity I in the case of CLC-11 as expected.

The value of the y component of the director is shown in Fig. 2.11 for the zero field intensity (dashed lines) and for an input intensity which gives rise to the normalized transmitted intensity J = 0.18 (solid lines). This figure shows the pitch dilation near z = 0 and the pitch contraction near z = L as we discussed earlier. In most cases, pitch dilation is more dominant than pitch contraction because most of the field reflects within a few pitch lengths from z = 0.

The reflectivity R of a CLC cell can be defined by

$$R = \frac{\text{reflected field intensity}}{\text{input field intensity}} = 1 - J/I \tag{62}$$

A plot of reflectivity as a function of the normalized input intensity I is shown in Fig. 2.12 for the two different anchoring conditions. The reflectivity for the CLC-11 is nearly constant over a broad range of normalized input intensity I and differs substantially from that of the CLC-10.
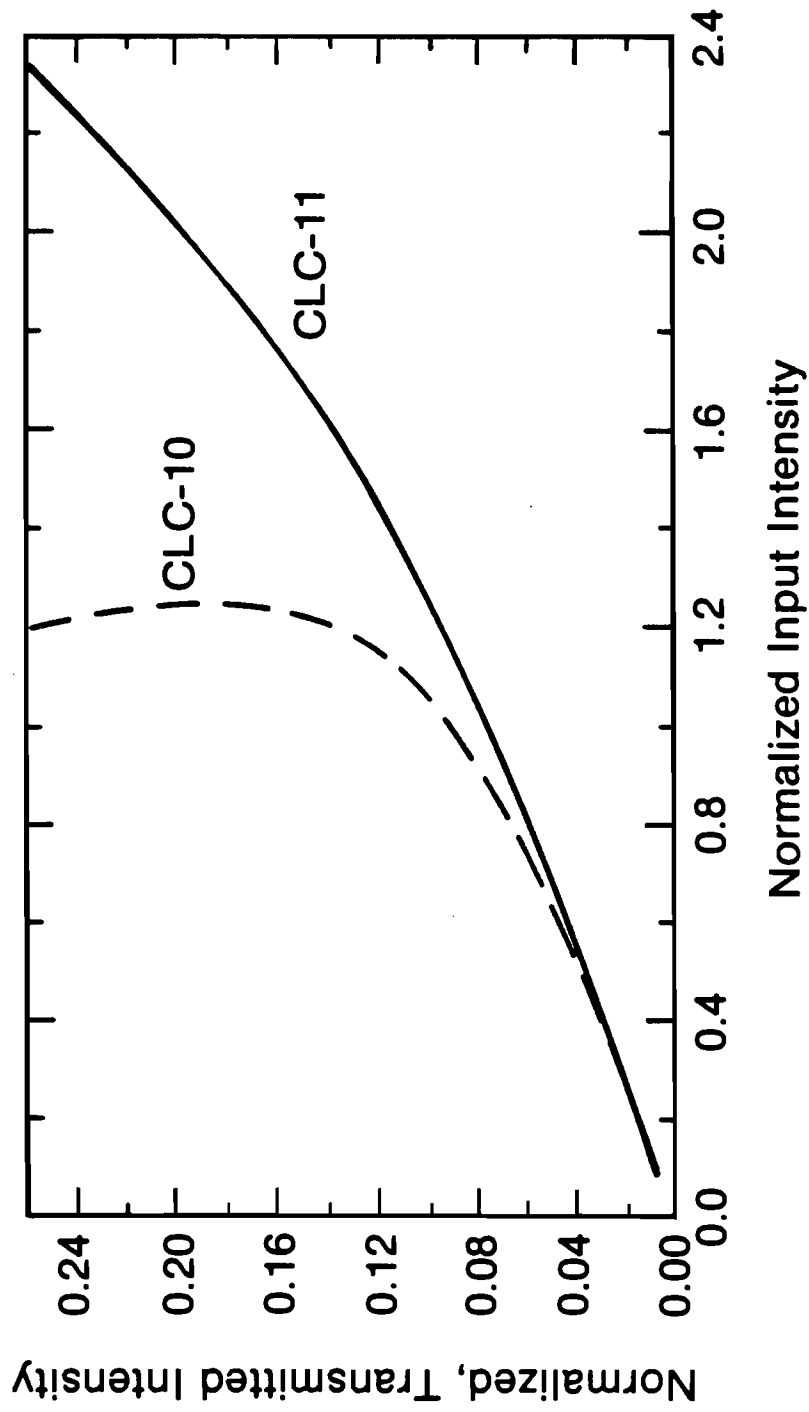
Fig. 2.10    Normalized transmitted intensity J versus normalized input intensity I for $\kappa L = 2.0$. (Solid lines represent the CLC-11 case and dashed lines represent the CLC-10 case). Intensities are normalized by $32\pi k_{22}\kappa^2/\epsilon_a$.
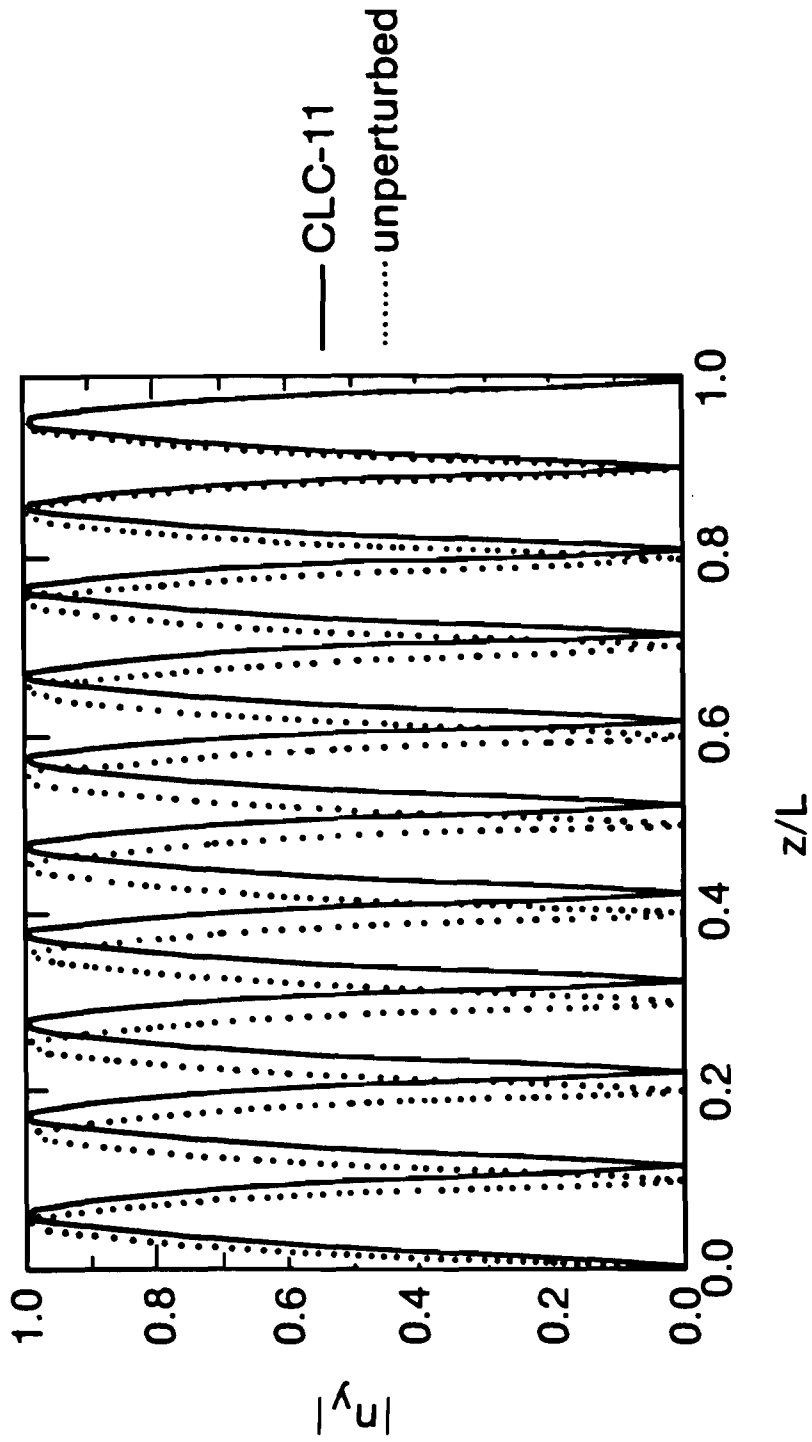
Fig. 2.11    The value of the y component of the director for the zero-field case (dashed lines: unperturbed case) and for an incident intensity which cause normalized transmitted intensity $J = 0.18$ (solid lines). $L$ is chosen to yield an unperturbed $\theta(L) = q_0L = 10\pi$.
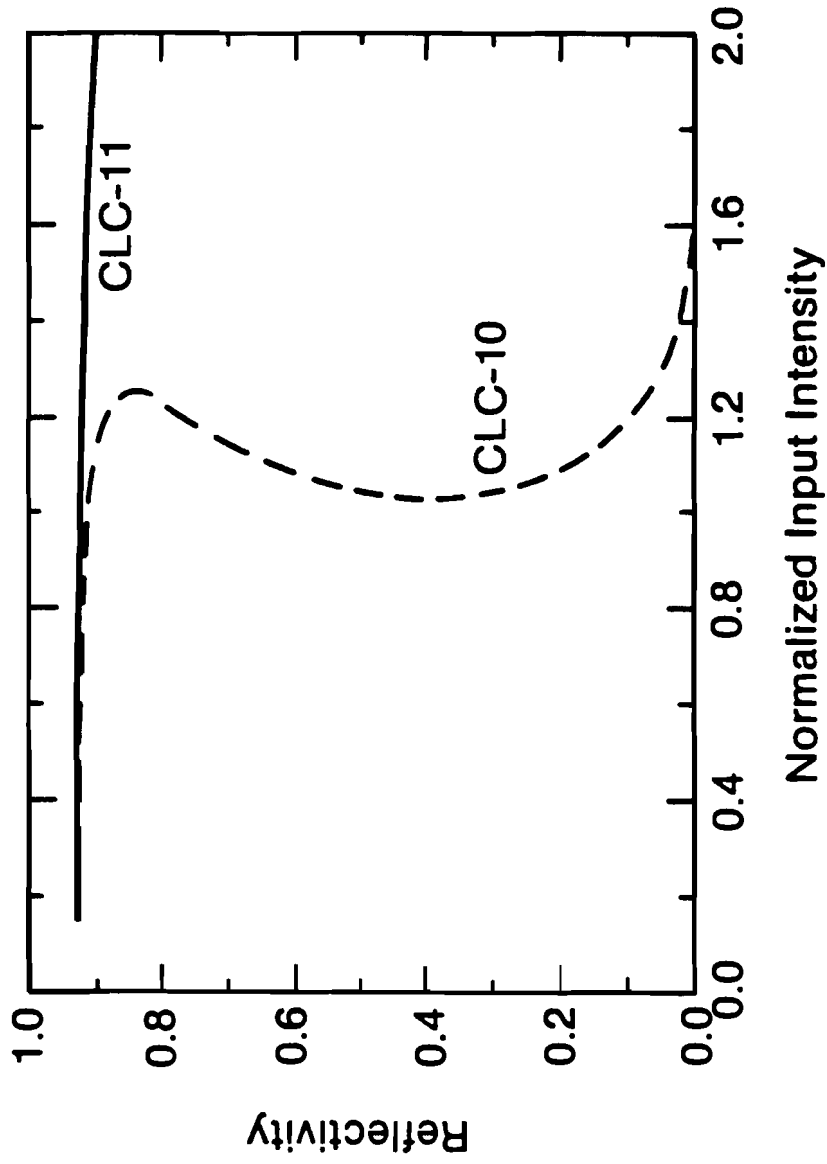
Fig. 2.12    Reflectivity R as a function of normalized input intensity I (solid lines represent the CLC-11 case and dashed lines represent CLC-10 case).

From Eq. (57), the phase of the reflected field at $z = 0$ can be written as:

$$\phi_-(0) = \phi_+(0) - \cos^{-1}\left[ -\sqrt{1\text{-}J/I} \ \{\Delta k/\kappa - 2S + I + J\}\right] \tag{63}$$

where $I = u(0)$. Equation (63) relates the phase of the reflected field to the normalized input intensity $I$. The phase of the reflected field for two different anchoring cases as a function of normalized input intensity $I$ and normalized detuning parameter $\Delta k/\kappa$ when $\phi_+(0) = 0$ is shown in Fig. 2.13. Since the strong anchoring at $z = L$ prohibits the helix from changing, the slope of the phase lag in a CLC-10 is steeper than in a CLC-11.

In conclusion, we have solved Maxwell's equation to derive the selective reflection in wavelength and polarization, optical activity, and the reflectivity for the CLC structure. We have also solved Maxwell's equation and the Euler-Lagrange equation in detail for cholesteric liquid crystals with different boundary conditions in the presense of an intense optical field. The results show that for CLC-11 case, pitch dilation at the input side of the cholesteric liquid crystal leads to pitch contraction at the output side, only pitch dilation for CLC-10 and pitch contraction for CLC-01. As a transverse effect, we showed that a CLC exhibits a retro-self-focusing effect under the Gaussian intensity distribution of an incident optical field, which is a result of intensity dependent pitch dilation.
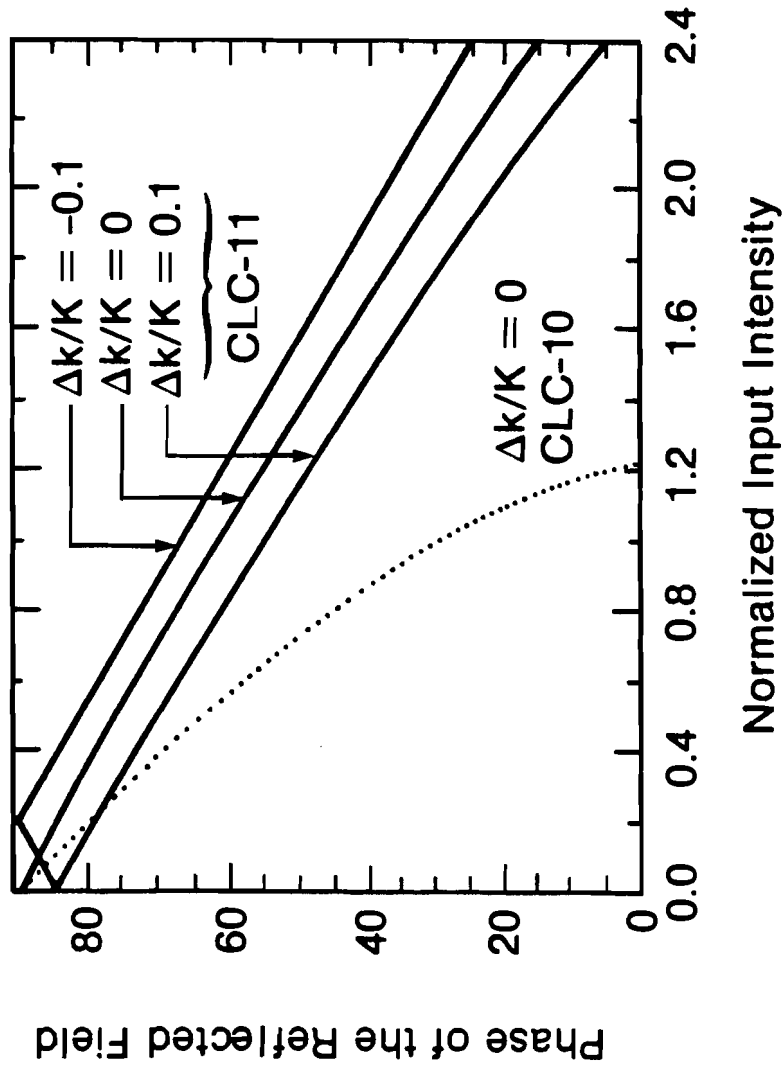
Fig. 2.13    Normalized input intensity I versus the phase of the reflected field when the phase of the incident field $\phi_+(0) = 0$.
($\kappa L = 2.0$ with $\Delta k/\kappa = 0$, $\pm 0.1$ and $q_0 L = 10\pi$ for CLC-11: solid lines; $\kappa L = 2.0$ with $\Delta k/\kappa = 0$ for CLC-10: dashed lines).

**REFERENCES**

1. M. C. Mauguin, <u>Bull. Soc. Soc. Franc. Miner. Crist.</u> <u>34</u>, 71 (1911).

2. C. W. Oseen, <u>Trans Faraday Soc.</u> <u>29</u>, 883 (1933).

3. H. De Vries, "Rotatory Power and Other Optical Properties of Certain Liquid Crystals," <u>Acta Cryst.</u> <u>4</u>, 219 (1951).

4. P. G. de Gennes, <u>The Physics of Liquid Crystals</u> (Claredon, Oxford, 1974), pp. 227–229.

5. E. B. Priestley, "Introduction to the Optical Properties of Cholesteric and Chiral Nematic Liquid Crystals," <u>RCA Rev.</u> <u>35</u>, 585 (1974).

6. J. W. Shelton and Y. R Shen, "Study of Phase-Matched Normal and Umklapp Third-Harmonic Generation Process in Cholesteric Liquid Crystals," <u>Phys. Rev. A</u> <u>5</u>, 1867 (1972).

7. G. R. Fowles, <u>Introduction to Modern Optics</u>, 2nd ed. (Holt, Rinehart and Winston, Inc., 1975).

8. Jae-Cheul Lee, J. H. Kelly, D. L. Smith, and S. D. Jacobs, "Gain Squaring in a Cr:Nd:GSGG Active-Mirror Amplifier Using a Cholesteric Liquid Crystal Mirror," <u>IEEE J. Quantum Electron.</u> <u>QE-24</u>, 2238 (1988).

9. A. Yariv, "Coupled-Mode Theory for Guided-Wave Optics," <u>IEEE J. Quantum Electron.</u> <u>QE-9</u>, 919 (1973)

10. J. C. Lee, S. D. Jacobs, and A. Schmid, "Retro-Self-Focusing and Pinholing Effect in a Cholesteric Liquid Crystal," <u>Mol. Cryst. Liq. Cryst.</u> <u>150b</u>, 617 (1987).

11. Jae-Cheul Lee, A. Schmid, and S. D. Jacobs, "Effects of Anchoring Under Intense Optical Fields in a Cholesteric Liquid Crystal," <u>Mol. Cryst. Liq. Cryst.</u> <u>166</u>, 253 (1989).

12. H. G. Winful, "Nonlinear Reflection in Cholesteric Liquid Crystals: Mirrorless Optical Bistability," <u>Phys. Rev. Lett.</u> <u>49</u>, 1179 (1982).

13. P. E. Byrd and M. D. Friedman, <u>Handbook of Elliptic Integrals for Engineers and Scientists</u> (Springer-Verlag, Berlin, 1971), pp. 120–133.

# CHAPTER III

## Nd:YAG Laser with Cholesteric Liquid Crystal Cavity Mirrors

The literature contains few references to the use of cholesteric liquid crystals (CLCs) as laser end mirrors. In 1978, I. P. Il'chishin et. al.[1] reported the tuning and narrowing of the emission spectrum of a dye laser with a CLC mirror. The frequency tuning from 567 nm to 585 nm was achieved in the temperature range of 22°-28°. In 1980, Denison et al.[2] also reported the operation of the Cu I vapor laser with a CLC end mirror. Temperature tuning for operation at 510.6 nm or 578.2 nm was demonstrated. However, no characterization of the output beam was provided. And in Chap. 2, we theoretically predicted that under exposure to a plane wave with a Gaussian intensity distribution, a retro-self-focusing effect can occur in which the reflected field comes to a focus.

In this chapter, we will demonstrate the nonlinear retro-self-focusing effect in a cavity configuration by using a CLC element as a laser end mirror and explain the mechanism for $TEM_{00}$ mode operation, the cause for its alignment simplicity and its angular insensitivity. We will also describe mono-mode operation of a solid state laser with a CLC cavity end mirror. In what follows, we begin with the design and construction of liquid crystal mirrors.

## 3.1    Design and Construction of Liquid Crystal Laser Cavity Mirror[3]

In this section, we derive the necessary design parameters required for the fabrication of optimized CLC laser cavity end mirrors. These include the reflectivity of the CLC mirror, the coupling coefficient and the exact selective reflection bandwidth.

We give the Jones matrix representation of the CLC device. Finally we describe the fabrication of several devices.

A liquid crystal mirror consists of a cholesteric liquid crystal medium confined between two flat glass substrates as shown in Fig. 2.1. The helical structure of the CLC material leads to the important optical properties of selective reflection in wavelength and circular polarization (circular dichroism). The field reflected by a CLC preserves its sense of the polarization, whereas the field reflected by a dielectric mirror changes its polarization from right to left circular or vice versa. A CLC mirror can be modeled with a Jones matrix[4] by considering right circularly polarized light which passes through a quarter wave plate and a linear polarizer. It is then reflected back from a dielectric mirror, passing again through a linear polarizer and a quarter wave plate as shown in Fig. 3.1. The Jones matrix for a right-handed CLC element is given by

$$\frac{1}{\sqrt{2}}\begin{bmatrix} 1 & i \\ i & 1 \end{bmatrix}_W \begin{bmatrix} 1 & 0 \\ 0 & 0 \end{bmatrix}_{LP} \begin{bmatrix} 1 & 0 \\ 0 & -1 \end{bmatrix}_M \begin{bmatrix} 1 & 0 \\ 0 & 0 \end{bmatrix}_{LP} \frac{1}{\sqrt{2}}\begin{bmatrix} 1 & i \\ i & 1 \end{bmatrix}_W = \frac{1}{2}\begin{bmatrix} 1 & i \\ i & -1 \end{bmatrix} \tag{1a}$$

where the subscripts W, LP, and M represent a quarter wave plate, a linear polarizer and a dielectric mirror, respectively. For the left circularly polarized case, the light passes through a wave plate and is then rejected from a linear polarizer. In a similar way, the Jones matrix for a left-handed CLC is given by

$$\frac{1}{2}\begin{bmatrix} 1 & -i \\ -i & -1 \end{bmatrix} \tag{1b}$$
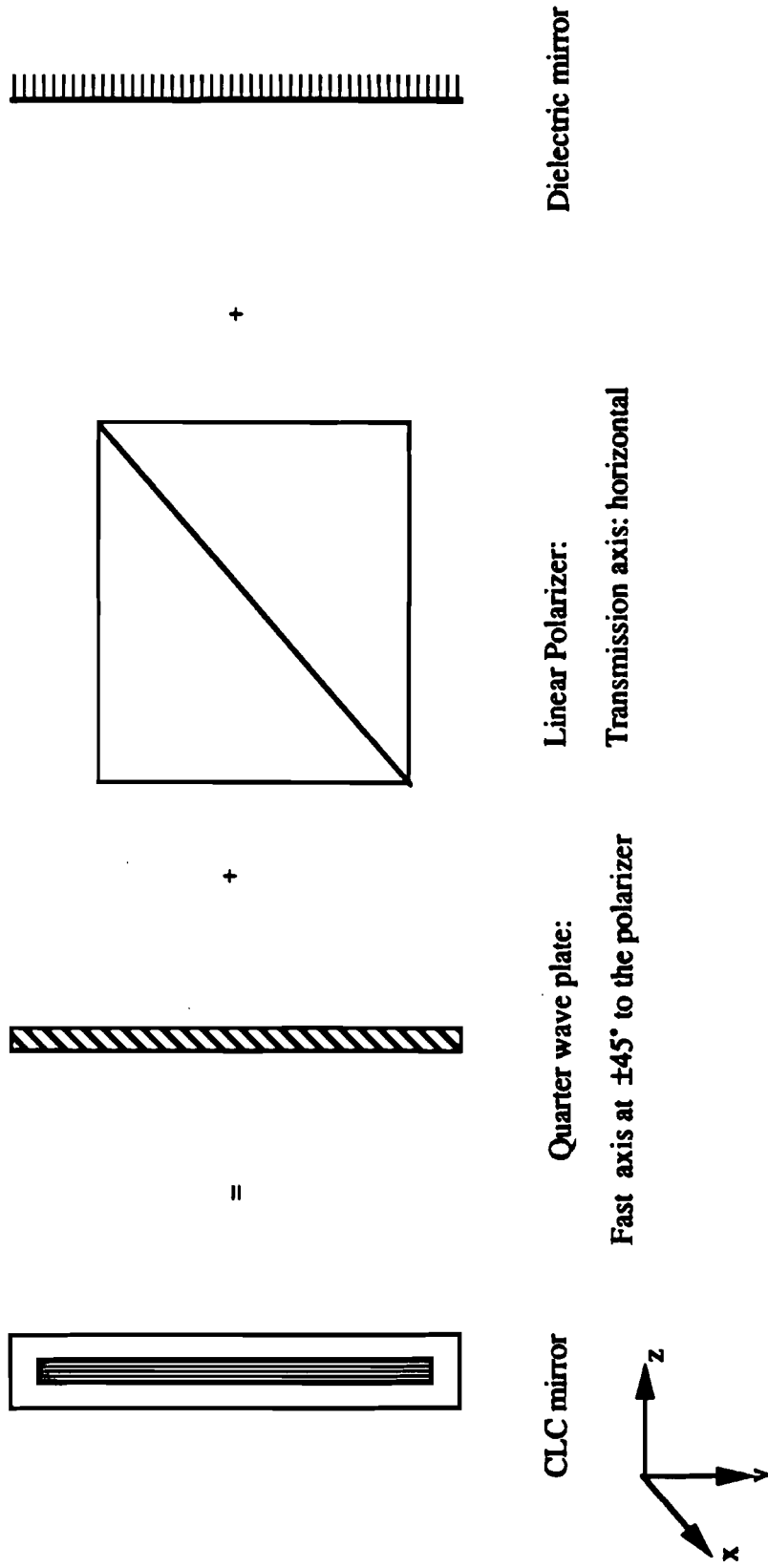
Fig. 3.1 Analogy of the CLC mirror with conventional optics. For a right-handed CLC, the fast axis is located at 45° with respect to the polarizer. For a left-handed CLC, the fast axis is located at -45° with respect to the polarizer.

When right (left) circularly polarized light with wavelength $\lambda$ propagates through a right (left)-handed CLC cell along the z-axis at normal incidence, the reflectivity from Eq. (23) in Chap. 2 is given by[5]

$$R = \frac{\sinh^2 \kappa L \sqrt{1 - (\delta/\kappa)^2}}{\cosh^2 \kappa L \sqrt{1 - (\delta/\kappa)^2} - (\delta/\kappa)^2} \tag{2}$$

where $\kappa = (2\pi/\lambda)(\varepsilon_a/4n_{av})$ is the coupling coefficient; $\delta = 2\pi(1/\lambda - 1/\lambda_0)n_{av}$ is the detuning parameter; $\lambda_0 = n_{av}P_0$ is the peak wavelength of the selective reflection band; $\Delta n = n_e - n_0$ is the optical birefringence; $n_{av} = (n_e + n_0)/2$ is the average refractive index and L is the CLC fluid thickness. Here $n_e$ and $n_0$ represent the extraordinary and ordinary refractive indices, respectively, of the nematic substructure shown in Fig. 2.1.

When $\lambda = \lambda_0$, the CLC structure is well phase-matched to the input wavelength, and the reflectivity in Eq. (2) reduces to

$$R = \tanh^2(\kappa_0 L) \tag{3}$$

where $\kappa_0 = \dfrac{\pi}{\lambda_0}\Delta n$. To act as a full reflector with R = 0.999, the $\kappa_0 L$ required is equal to 4.147. To act as a partial reflector with R = 0.90, the $\kappa_0 L$ required is equal to 1.818. As an example, for a CLC with $\Delta n = 0.17$, the required thickness is 8.3 $\mu$m for R = 0.999 and 3.6 $\mu$m for R = 0.90 at 1064 nm. Since the coupling coefficient is proportional to birefringence, materials with lower birefringence require more CLC fluid thickness than those with higher birefringence. Since $\kappa$ is also inversely proportional to $\lambda$, mirrors designed to operate at shorter wavelengths may be thinner

than those designed for longer wavelenghs to have the same reflectivity (neglecting dispersion).

From Eq. (2), the exact selective reflection bandwidth $\Delta\lambda$ is given by

$$\Delta\lambda = 2\frac{\sqrt{1 - \left(1 - \gamma^2/4\right)\left[1 - \left(P_0/2L\right)^2\right]}}{1 - \left(P_0/2L\right)^2}\lambda_0 \qquad (4)$$

Note that the selective reflection bandwidth depends on the thickness in this exact expression. A plot of $\Delta\lambda/\lambda_0$ as a function of $(P_0/2L)$ is shown in Fig. 3.2. When $P_0/L \ll 1$, the selective reflection bandwidth reduces to Eq. (5),[6]
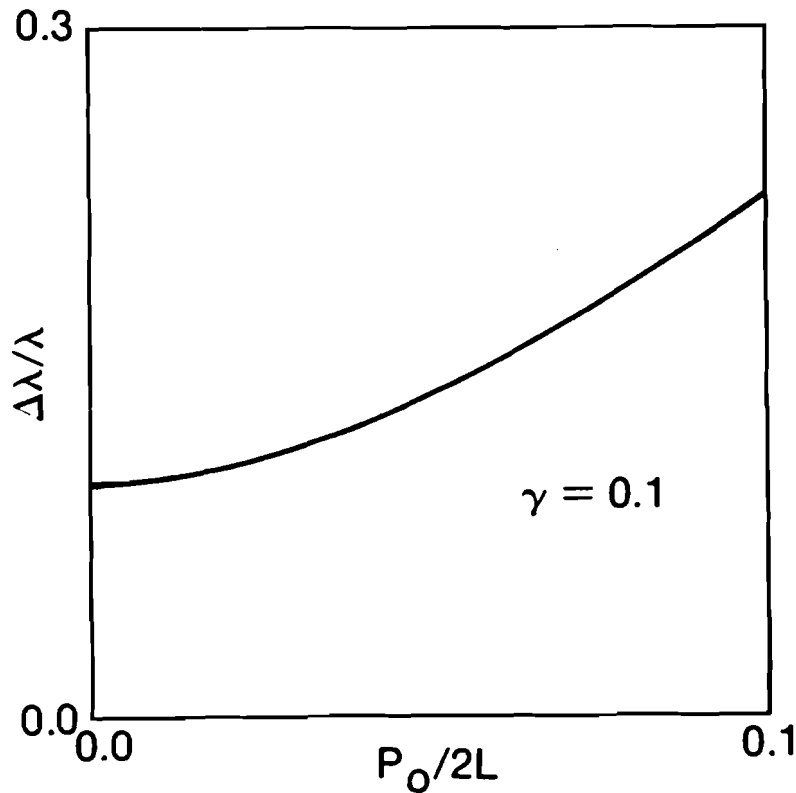


Fig. 3.2    Normalized selective reflection bandwidth $\Delta\lambda/\lambda_0$ as a function of $P_0/2L$.

$$\Delta\lambda = \gamma \, \lambda_o \approx \frac{\Delta n}{n_{av}} \, \lambda_o \tag{5}$$

This equation shows that the bandwidth of a CLC element tuned to a visible wavelength ($\lambda_o$ = 532 nm) is narrower than that for an element tuned to a near-infrared wavelength ($\lambda_o$ = 1064 nm) by a factor of 2. Bandwidth is also proportional to the birefringence of the material. Fluid thickness no longer enters into the equation.

To experimentally verify the relationships in Eq. (3) and Eq. (4), the refractive indices of two different CLC blends were first measured to calculate the coupling coefficient $\kappa_o$. The procedure for measuring the refractive index of a CLC is straightforward. CLC's have a birefringence which is related to that of the nematic substructure (see Fig. 2.1) perpendicular to the helical axis by the following equations[7]:

$$n_{e,ch} = n_{o,n}, \qquad n_{o,ch} = \left[ 0.5 \left( n_{e,n}^2 + n_{o,n}^2 \right) \right]^{\frac{1}{2}} \tag{6}$$

where $n_{e,ch}$, $n_{o,ch}$ represent the refractive indices for the chiral structure and $n_{e,n}$, $n_{o,n}$ for the nematic substructure. The subscripts e,o stand for extraordinary and ordinary refractive indices, respectively. When an Abbé refractometer is used to measure the refractive indices of the CLC, $n_{e,ch}$ and $n_{o,ch}$ are obtained. The refractive indices $n_{e,n}$, $n_{o,n}$ are calculated from Eq. (6) as well as the average refractive index, the birefringence, and the coupling coefficient $\kappa_o$. The measurements and calculations are summarized in Table 3.1 for the two CLC blends identified as mixtures I and II.

In order to confirm Eq. (3), a wedged cell with weak anchoring[8] on both inner substrate surfaces was fabricated. The reflectivity as a function of thickness is shown
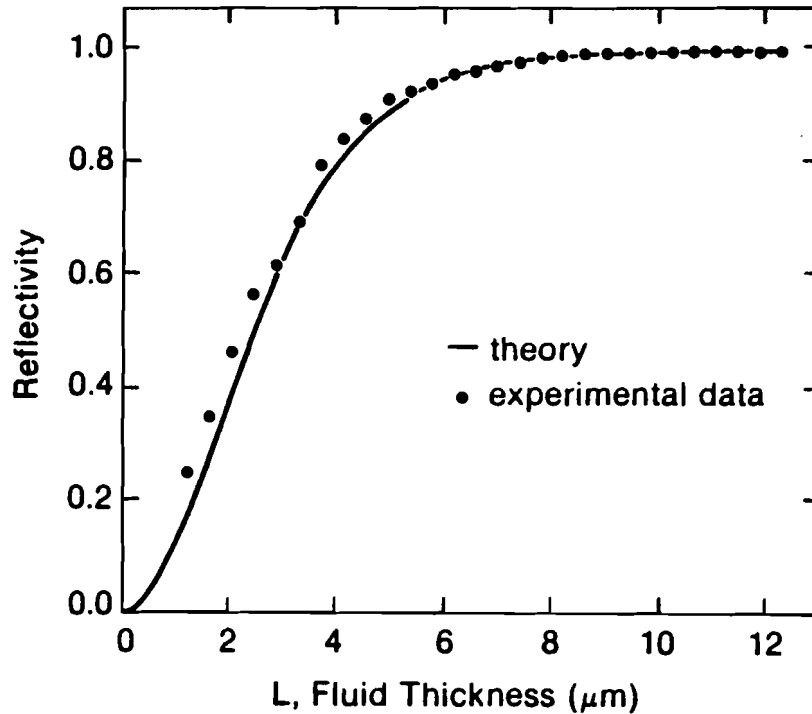
Fig. 3.3    Reflectivity R measured at $\lambda$=1064 nm, as a function of thickness L, for a mixture of E7 and CB15 tuned to exhibit a selective reflection band peak at $\lambda_o$=1064 nm. The solid line represents the result of theoretical calculation, and the circles represent experimental data.

in Fig. 3.3. The close match of theoretical and experimental data supports the validity of Eq. (6).

In order to confirm Eq. (4), two 38-mm diameter CLC mirrors were assembled using BK-7 glass substrates, separated by Mylar$^{®}$ spacers. The gap was filled by capillary action with each of the right-handed CLC mixtures I and II described in Table 3.1.

Spectral transmission scans are shown in Fig. 3.4. From this figure, the wavelength separation between the first minima was used as a measure of the bandwidth. The bandwidths for mixture I with a 9-$\mu$m fluid thickness, and for mixture II with a 12-$\mu$m fluid thickness are summarized in Table 3.2 with theoretical

(a)

(b)
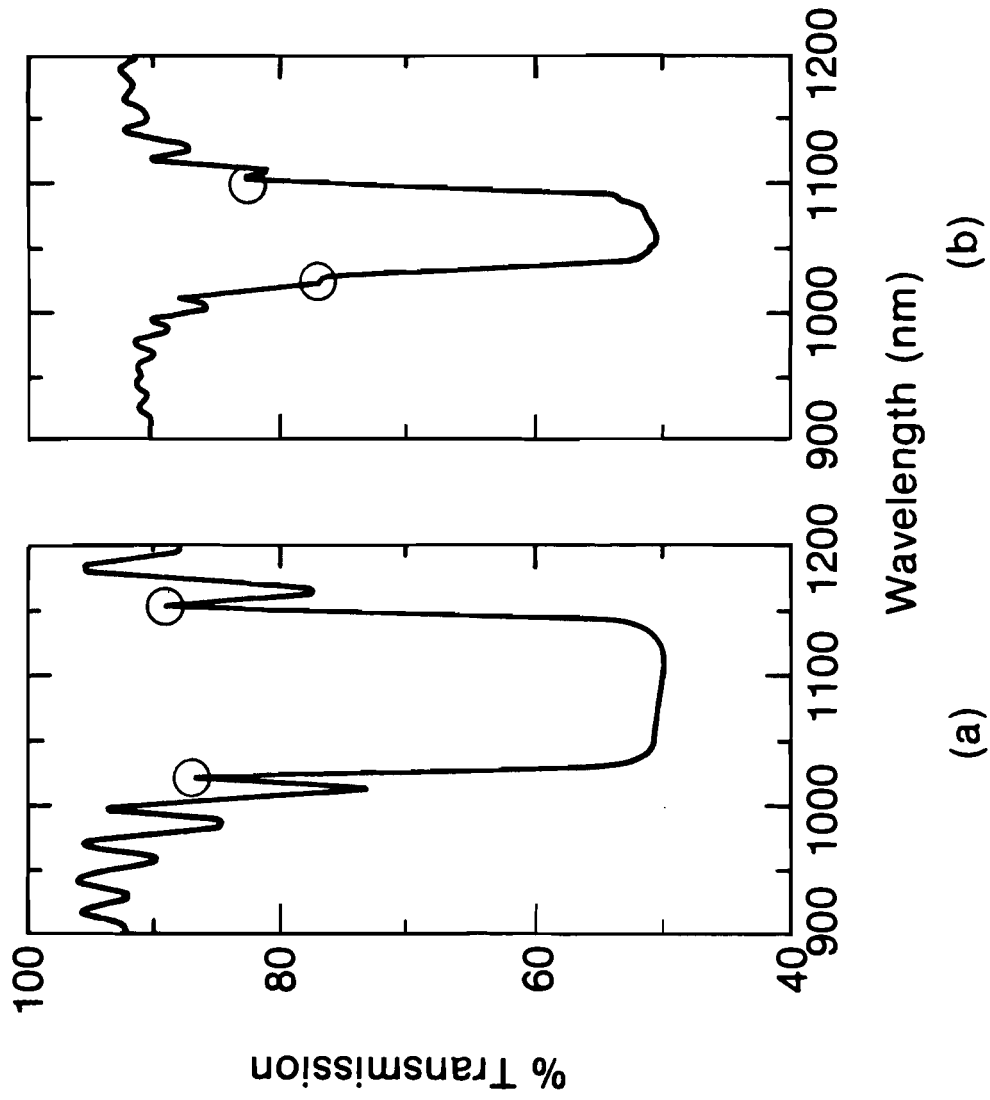
Fig. 3.4   Spectral scans of the CLC mirror:   (a) a mixture of E7 and CB15;   (b) a mixture of ZLI 1167 and CB15.

calculations from Eq. (4) and Eq. (5). The experimental results for both mixtures agree well with the theoretical calculations of Eq. (4). The use of the approximate Eq. (5) shows about a 30 nm differences in bandwidth for both mixtures, indicating that the condition $P_0/2L \ll 1$ is not satisfied.

From Eq. (3), the thicknesses required for $R = 0.999$ are calculated to be 8.0 $\mu m$ and 18.5 $\mu m$, respectively, for mixtures I and II. Index matching between substrates and CLC fluids is important for laser mirror applications. From Table 3.1, the mixture of ZLI1167 and CB15 shows a good index match to BK-7 whose index at $\lambda = 1064$ nm is 1.509.

## TABLE 3.1

**Measurements and Calculations of Refractive Index and Coupling Coefficient**

| Blends with $\lambda_0 = 1064$ nm | | $n_{e,n}$ | $n_{o,n}$ | $n_{av}$ | $\Delta n$ | $\kappa_0$ |
|---|---|---|---|---|---|---|
| Mixture I | E7 + CB15 | 1.6860 | 1.5121 | 1.5991 | 0.1739 | 0.5182 |
| Mixture II | ZL11167 + CB15 | 1.5495 | 1.4703 | 1.5099 | 0.0792 | 0.2238 |

## TABLE 3.2

**Theoretical Calculations of Bandwidth and the Measured Results**

| | $L[\mu m]$ | $\Delta\lambda$ [nm] measured | $\Delta\lambda$ [nm] from Eq. 4 | $\Delta\lambda$ [nm] from Eq. 5 |
|---|---|---|---|---|
| Mixture I | 9 | 150 | 146 | 115 |
| Mixture II | 12 | 84 | 82 | 56 |

## 3.2 Retro-Self-Focusing Effect and Pinholing Effect[8],[9]

In Chap. 2, we predicted that under exposure to a plane wave with a Gaussian spatial distribution, a retro-self-focusing effect occurs in a CLC mirror, wherein the reflected field comes to a focus as a result of an intensity dependent pitch dilation. When this CLC element is used as a laser end mirror, the CLC element will act like a well-aligned concave mirror/pinhole combination and $TEM_{00}$ mode operation will be obtained as a result of the pinholing effect. The mechanism of this pinholing effect is as follows: a $TEM_{00}$ mode has the lowest loss per round trip compared to higher order spatial modes. After sufficient round trips, the $TEM_{00}$ mode becomes dominant and creates a concave mirror over the effective clear aperture of the mirror surface, preventing higher order modes from oscillating.

### Characteristics of Nd:Yag laser with a CLC cavity end mirror

A commercial Nd:YAG laser (Control Laser Corp. Model 256) has been employed for this work. The resonator configurations considered are shown in Fig. 3.5. In Fig. 3.5(A), the CLC–dielectric resonator consists of a flat dielectric HR end mirror, 54-mm long by 4-mm diameter Nd:YAG laser rod, an uncoated $\lambda/4$ plate, and a CLC RH8-10 (see Chap. 1 for nomenclature) end mirror. Output beam patterns were taken with IR film and a CID[10] camera at each end of the resonator, respectively. Figure 3.6 shows the output beam pattern leaked through the HR side. Data captured by the CID camera were passed to a beam analyzer which consisted of a PDP–11/73 and beam analysis software. Contouring patterns show the beam symmetry, and a Gaussian fit of the output intensity distribution shows that a perfect Gaussian beam was generated inside the resonator as a result of pinholing effects. The ellipticity was about 1.04. The output patterns at the CLC mirror side are shown in Fig. 3.7. These
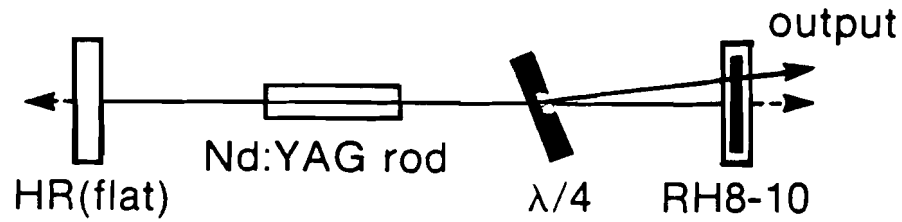
(A)
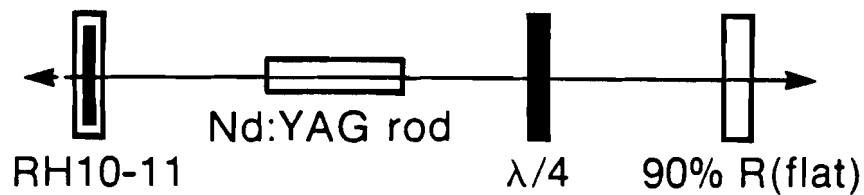


(B)

Fig. 3.5    The CLC resonator configuration tested in the experiment.  (A) CLC
(thick)-dielectric (flat) resonator: output via Fresnel reflection off the slightly
tilted waveplate; (B) CLC -dielectric resonator: output through 90% output
coupler.

photographs were taken with IR film approximately 4 meters from the output mirror.

The polarization change upon Fresnel reflection from the λ/4 plate permits output

coupling through the CLC mirror.  The coupled output beam is shown in Fig. 3.7(A).

At higher lamp current (~16A), a ring pattern evolved with an intensity dip at the center

and a scattering pattern as shown in Fig. 3.7(B).
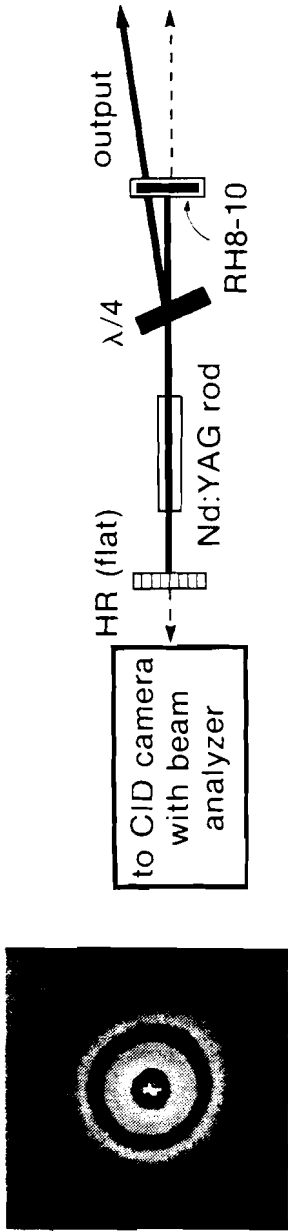
- Sampling of leakage through HR shows perfect Gaussian in resonator.
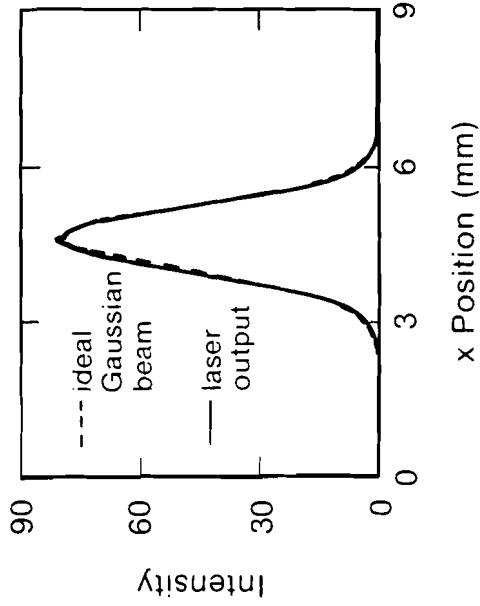
Fig. 3.6   Resonator configuration A:   Quality of output.   Computer-generated intensity contour patterns and Gaussian fit to a linear scale through the 2-D contour map.

laser output

scattered light

(A)

(B)
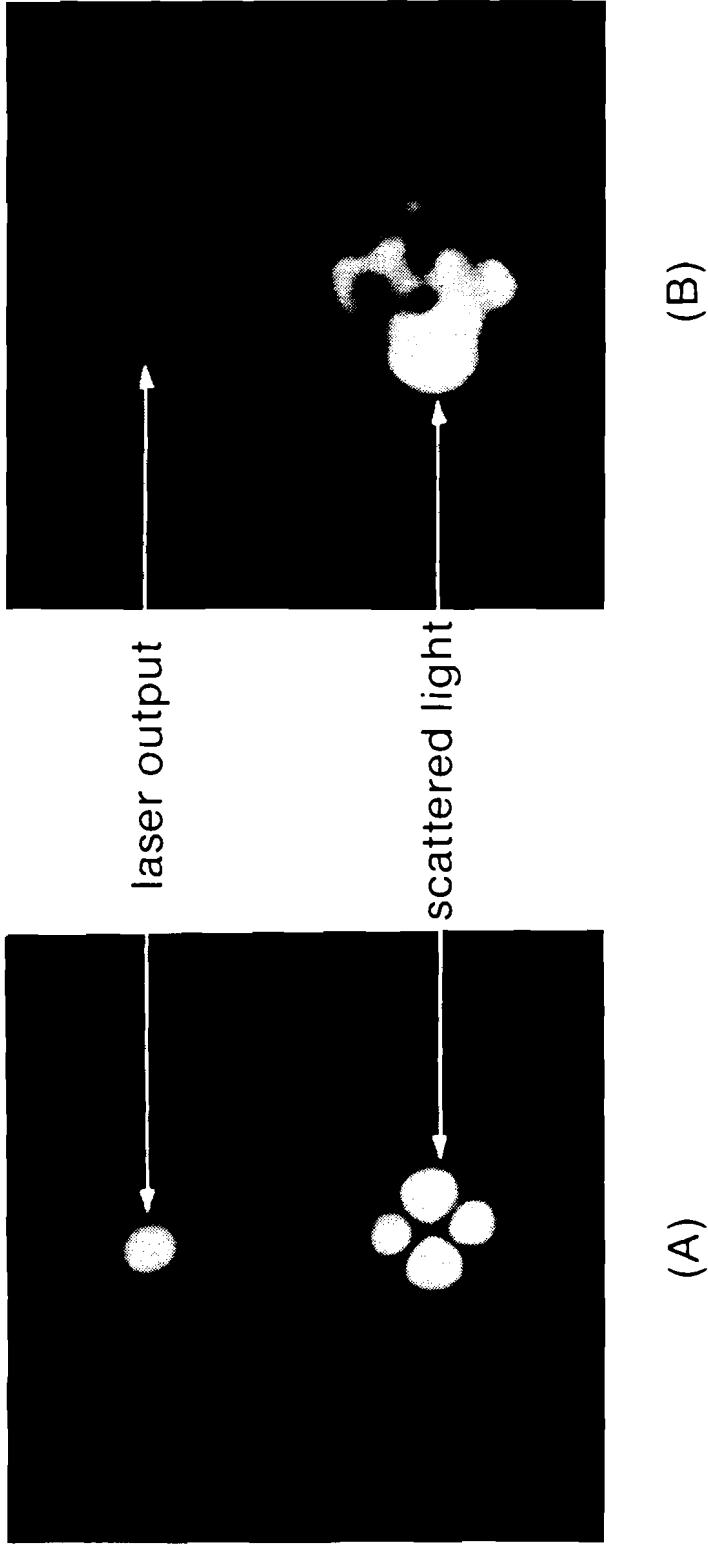
Fig. 3.7    The output of the CLC-dielectric resonator configuration A at the CLC mirror side:    (A) at low current (10.5A);
(B) at high lamp current (16 A).
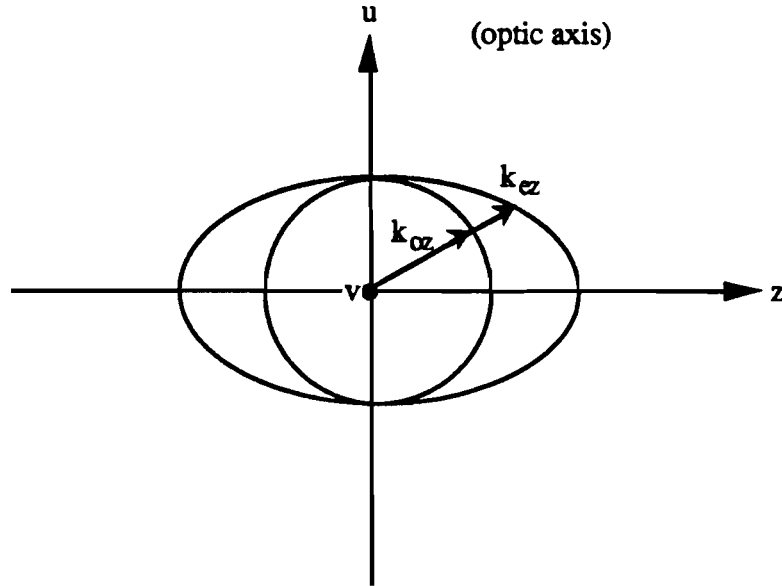
Fig. 3.8    Wave-vector surfaces in the u-z plane for a positive uniaxial crystal.

From the right-handed CLC mirror, a quadrupole scattering pattern was observed as shown in Fig. 3.7(A). The mechanism can be easily explained by using an analogy for the CLC mirror shown in Fig. 3.1. Let us consider a uniaxial crystal (in our analogy, a $\lambda/4$ plate made of nematic liquid crystal) which lies in a local coordinate system (u,v) such that u is the optic axis and v is perpendicular to it, as shown in Fig. 3.8.[11,12] The angular dependence of the extra-ordinary index of refraction causes an angle dependent change in optical path length. In a CLC-dielectric resonator, the retro-self-focusing effect in a CLC mirror provides angular dependence in optical path length on the CLC mirror. When a beam of light with wavelength $\lambda$ passes through the medium, the wavevector component for the ordinary wave, $k_{oz}$, is given by

$$k_{oz} = \left(\frac{2\pi}{\lambda}n_o\right)^2 - k_u^2 - k_v^2 \tag{7}$$

For the extra-ordinary wave, the wave vector component, $k_{ez}$, is given by

$$k_{ez} = \left(\frac{2\pi}{\lambda}n_e\right)^2 - k_u^2\left(\frac{n_o}{n_e}\right)^2 - k_v^2 \tag{8}$$

The total phase change for a sample of thickness L is then given by

$$\varphi = \left(k_{ez} - k_{oz}\right)L$$

$$\cong \varphi_0\left[1 - \left(\frac{2\pi}{\lambda}\right)^2 \frac{1}{2n_o}\left(\frac{k_u^2}{n_o} - \frac{k_v^2}{n_e}\right)\right] \tag{9}$$

where $\varphi_0 = \frac{2\pi}{\lambda}\Delta nL$ is the phase change at the center of the input beam and the second term shows that lines of constant phase are hyperbolas, which is known as an isogyre pattern. In a strong optical field, pitch dilation in a CLC mirror occurs. This effect can be taken into account by introducing a twisted nematic waveplate in Fig. 3.1. For a twisted nematic, let us assume that it has solutions of the form $f = e^{(k_x x + k_y y)}e^{i(k_z z - \omega t)}$. After passing through the medium, the k vectors are rotated as follows:

$$\begin{bmatrix} k_u \\ k_v \end{bmatrix} = \begin{bmatrix} \cos\theta(z) & \sin\theta(z) \\ -\sin\theta(z) & \cos\theta(z) \end{bmatrix}\begin{bmatrix} k_x \\ k_y \end{bmatrix} \tag{10}$$

where $\theta(z)$ is the twist angle through the medium. The phase change $\Delta\varphi$ from a layer of thickness $\Delta z$ can be calculated and the total phase change is then given by

$$\varphi = \varphi_0\left[1-\left(\frac{2\pi}{\lambda}\right)^2\frac{1}{4n_o^2n_e}\left\{\Delta n\left(k_x^2+k_y^2\right)-2n_{av}\left[\left(k_x^2-k_y^2\right)<\cos 2\theta>+2k_xk_y<\sin 2\theta>\right]\right\}\right]$$

(11)

where the brackets indicate the average values of the quantity included. The second term represents circular patterns and the third term represent an isogyre pattern rotated by an amount $\Omega$ as defined in Eq. (12).

$$\tan 2\Omega = \frac{<\sin 2\theta>}{<\cos 2\theta>}$$

(12)

Figure 3.9 shows the rotation of an isogyre pattern as lamp current is increased from 11 A to 13 A in a CLC(RH12-10)-dielectric resonator.

## Measurement of retro-self-focusing effect

The retro-self-focusing effect was observed by investigating the output beam from the CLC-dielectric resonator in Fig. 3.5(A). Since a CLC mirror was fabricated between plane parallel substrates, the reflected beam from $\lambda/4$ plate should diverge beyond the CLC mirror. However, experiment showed it to converge at a certain distance beyond the CLC mirror and then diverge. This showed that the CLC mirror acted as a concave mirror. For the CLC-dielectric resonator in Fig. 3.5(B), the retro-

(a) 12 A      (b) 13 A      (c) 14 A

Fig. 3.9    Evolution of scattering pattern as a function of current. As current is increased, the pattern is rotated.

self-focusing effect was quantified by measuring the effective radius of curvature $R_{CLC}$ of the CLC mirror. Here the YAG laser rod was assumed to be a thin lens[13] and the CLC was modeled as a concave mirror as shown in Fig. 3.10. In the notation of the ABCD matrix formalism widely used in laser resonator analysis, the radius of curvature $R_O$ and the beam radius $w_O$ at the output coupler are given by:[14]

$$R_o = \frac{2B}{A-D} = \infty \tag{13}$$

$$\frac{\pi w_o^2}{\lambda} = \frac{B}{\left[1-(\frac{A+D}{2})^2\right]^{1/2}} \tag{14}$$

where

$$A = D = 1 - \frac{2d}{f_1} - \frac{d}{f_2} + \frac{3d_1d_2}{f_1f_2} + \frac{2d_1d_2}{f_1^2} - \frac{d_1d_2^2}{f_1^2f_2} \tag{15}$$

$$B = 2d - \frac{2(dd_1 + d_1d_2)}{f_1} - \frac{d^2}{f_2} + \frac{2dd_1d_2}{f_1f_2} + \frac{2d_1^2d_2}{f_1^2} - \frac{d_1^2d_2^2}{f_1^2f_2} \tag{16}$$

$$d = d_1 + d_2, \quad f_2 = R_{CLC}/2 \tag{17}$$

Equation (14) shows that the beam radius $w_O$ changes with radius of curvature $R_{CLC}$.

## Resonator Configuration



## Geometrical Optics Equivalence
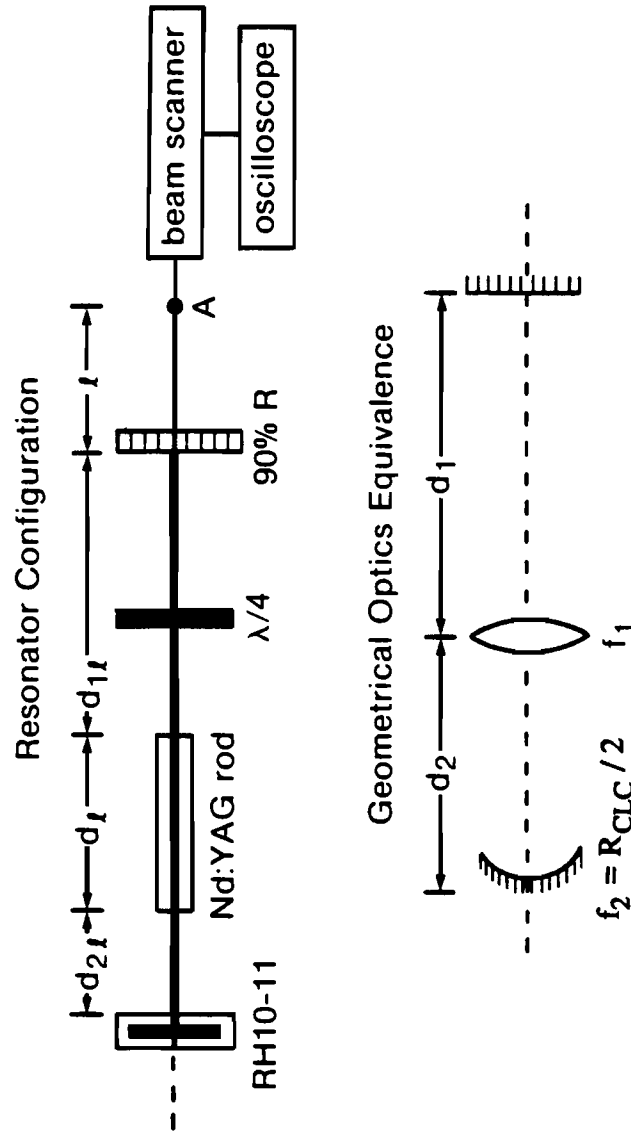


Fig. 3.10    Experimental setup for measurement of the radius of curvature for a CLC mirror and its geometrical optics equivalent.

If $w_0$ and $f_1$ (the thermal lensing effect of the rod) are known, one can calculate the radius of curvature $R_{CLC}$.

The thermal lensing effect can be measured accurately by shearing interferometry[15] without cavity end mirrors as shown in Fig. 3.11(A). For this experiment, a beam expander collimates a He-Ne beam which enters the laser rod. The shearing is accomplished with a shearing plate which is tilted and wedged in orthogonal directions. The interferograms generated are captured by a CID camera and displayed on the monitor. Under no optical pumping, straight fringes parallel to the horizontal direction result. These straight fringes rotate due to thermal lensing as the optical pumping power increases. The effective radius of curvature of the laser rod $R_d$ can be estimated by

$$R_d = \frac{-s t_f}{\lambda \sin \theta_f} \tag{18}$$

where $R_d$ is the radius of curvature of the laser rod, s is the shearing distance, $t_f$ is the fringe spacing and $\theta_f$ is the rotation angle of the straight fringes. The result is depicted in Fig. 3.11(B). It shows that the laser rod used here acts as a negative lens below the lasing threshold current ($\approx$ 10 A) and as a positive lens at higher current.

We determined the beam radius $w_0$ by measuring the beam radius $w_A$ at the position A [see Fig. 3.10] with a beam scanner[16],

$$w_0 = \left[ \frac{w_A^2 - \sqrt{w_A^4 - (2\lambda \ell / \pi)^2}}{2} \right]^{1/2} \tag{19}$$
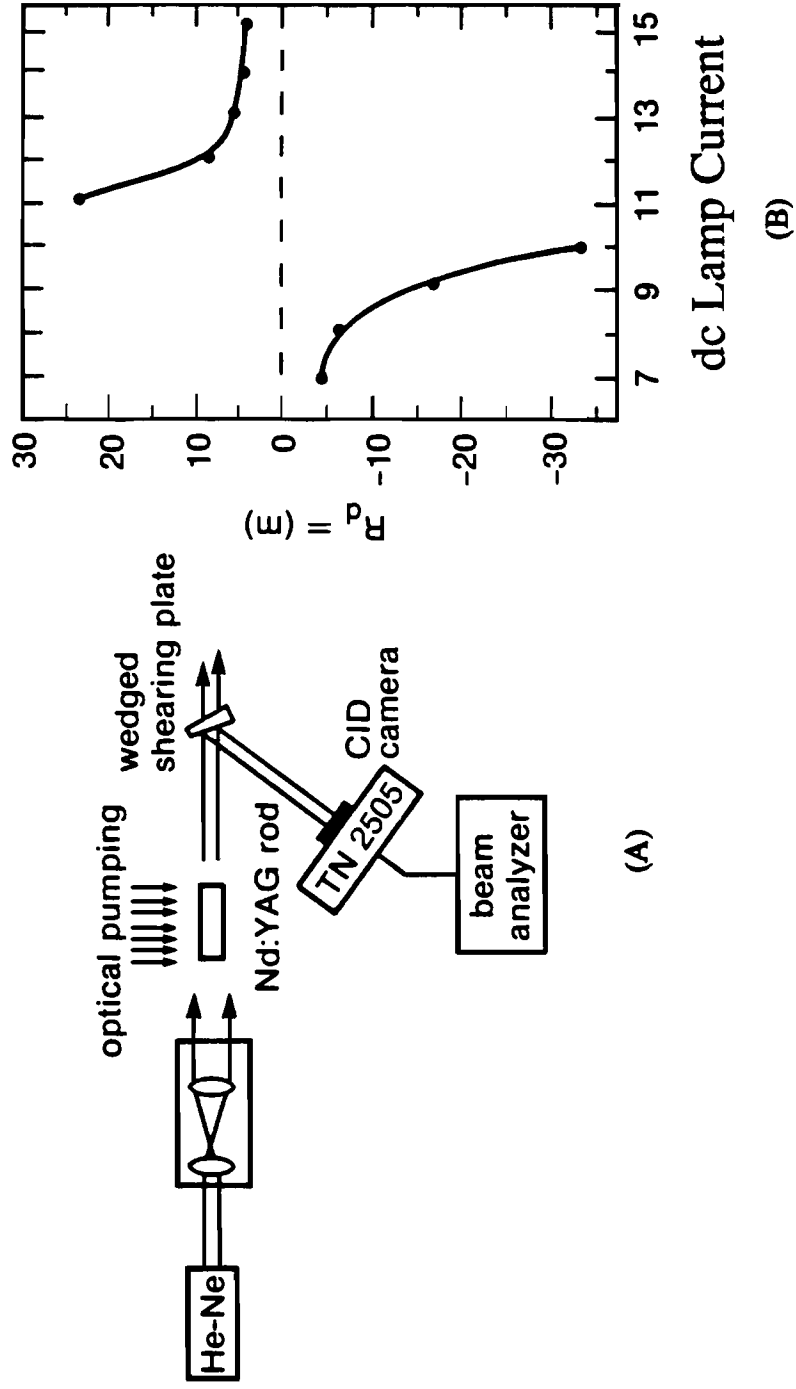
Fig. 3.11      (A) Experimental setup for measurement of the thermal lensing effect of the Nd:Yag laser rod; (B) Effective radius of curvature of the laser rod as a function of lamp current.

where $\ell$, which is equal to 286 cm, is the distance between the output coupler and position A. We measured the thermal lensing effect of the laser rod from Fig 3.11(B) and calculated the spot size $w_0$ from Eq. (10) at two different current settings. Those results are summarized in Table 3.3. In Fig. 3.10, we used $d_{1\ell}$= 282 mm, $d_{2\ell}$ = 312 mm and $d_\ell$ = 54 mm. The output intensity was confirmed to be Gaussian by beam-scanner derived oscilloscope traces. As the lamp current increased, the radius of curvature of the CLC decreased from 0.9–1 m to 0.7 m. This proved the CLC mirror to be concave and its optical power to increase with intra-cavity intensity. The cavity was in a stable region because $d/R_{CLC} \leq 1$, where d is the total cavity length.

From Eq. (54) in Chap. 2, the effective radius of curvature $R_{CLC}$, of the CLC mirror under intense optical field, is given by

$$R_{CLC} = -\frac{\pi w^2}{\lambda}\frac{1}{2\beta|E_0|^2} \qquad (20)$$

**TABLE 3.3   Effective Radius of Curvature of CLC Mirror.**

| lamp current (A) | Spot Size $W_0$ (mm) | Effective Radius of Curvature of | | Output Beam Profile |
|---|---|---|---|---|
| | | Laser Rod (m) | CLC Mirror (m) | |
| 10.8 | 0.4-0.3 | 25 | 0.9-1.0 | Gaussian |
| 11.6 | 0.3 | 12 | 0.7 | Gaussian |

where $\beta = \dfrac{1}{32\pi k_{22}\kappa^2}$ , $u = \beta |E_o|^2$ a normalized intensity, and w is the radius of the

beam. Let us assume the thermal lensing effect of the rod is negligible. Then for the

resonator configuration shown in Fig. 3.5(B) , the beam radius w on the CLC mirror is

determined by the radius of curvature R, as follows:

$$\frac{\pi w^2}{\lambda} = \sqrt{\frac{d|R_{CLC}|}{1-d/|R_{CLC}|}}$$

$$= \frac{d(1+4u^2)}{2u}$$

(21)

Substituting Eq. (21) into Eq. (20), one has

$$R_{CLC} = d + \frac{d}{4u^2}$$

(22)

The condition to obtain Eq. (20) was $u \leq 1$. This restricts the radius of curvature R to

be less than 1.25d. For the cavity configuration in Fig. 3.10, the cavity length was

63 cm and maximum radius of curvature R was equal to 79 cm. Our measurement of

effective radius of curvature $R_{CLC}$ for the CLC mirror was 0.9 to 1 m at 10.8 A and

0.7 m at 11.6 A. This data shows that the normalized intensity u was close to 1.

Above this lamp current, a ring pattern evolved with an intensity dip. The nonlinearlity

in the phase of the reflected field or optical bistability around $u \approx 1$ could be a reason

for the evolution of a ring pattern.

The slope efficiencies were measured for a flat-flat dielectric resonator, with and

without a pinhole for Gaussian beam generation, and a CLC-dielectric resonator as

shown in Fig. 3.12. The slope efficiency for the flat-flat dielectric resonator was steepest, but the spatial intensity distribution was multi-mode. However the output from the CLC (RH10-11)-dielectric (flat) resonator was $TEM_{00}$ mode with comparable slope efficiency and threshold current. Output power was quite insensitive to mirror tilt in the CLC-resonator as compared to the dielectric resonator. In the flat-flat dielectric resonator with a pinhole inserted for $TEM_{00}$ mode operation, the slope efficiency was significantly lower and its threshold current was about 20% higher than for the CLC-dielectric resonator.

The anchoring effect on the CLC-dielectric resonator in Fig. 3.5(A) was investigated. Three different kinds of CLC mirrors, that is, RH10–00, RH10–01 and RH10–11 were used. The resonator lased relatively easily with RH10–10 and RH10–11 CLC mirrors. Lasing could not be obtained with RH10–00 and RH10–01 mirrors because of increased scatter of the weakly anchored input sides of these mirrors. In any case, the degree of uniformity in anchoring and the CLC structure orientation throughout the bulk are critically important for achieving a lasing condition with a high quality output.

In conclusion, we have demonstrated a Nd:YAG laser with CLC end mirrors and described the performance in terms of the retro-self focusing effect and the pinholing effect. We also measured the effective radius of curvature to be ~1 m concave at moderate lamp currents. $TEM_{00}$ output of more than 3 W cw was obtained with no intra-cavity pinhole. The output profile did depend on the quality of the CLC structure. Temperature effects that are known to affect the optical performance of the CLC mirror have not been considered so far, although stable operation has been observed without any form of temperature control on the CLC mirror.
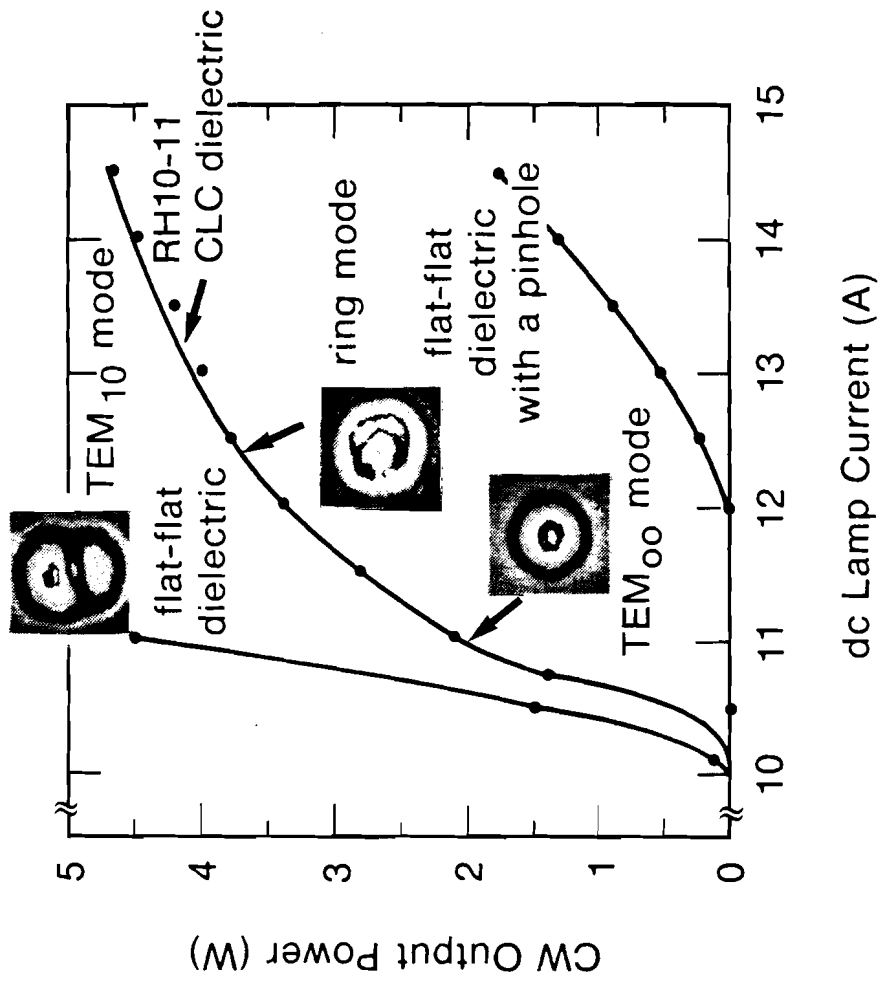
Fig. 3.12    The slope efficiencies for the CLC-dielectric resonator and a flat-flat dielectric resonator with or without a mode selecting intra-cavity pinhole.

## 3.3 TEM$_{00}$ Mode and Mono-longitudinal mode Laser Operation[17]

In a previous section of this chapter, we showed that, under exposure to a plane wave with a Gaussian spatial distribution, a retro-self-focusing effect occurs in a CLC element, wherein the reflected field comes to a focus as a result of an intensity-dependent pitch dilation. When this CLC mirror is used as a laser end mirror, it acts like a well-aligned concave mirror/pinhole combination. TEM$_{00}$ mode operation is obtained as a result of this pinholing effect. In this section, we show how a simple CLC element, when utilized as a laser end mirror, eliminates the need for separate wave plates and a polarizer in order to achieve mono-longitudinal mode in addition to TEM$_{00}$ mode operation.

In a solid state laser cavity, where two waves with the same frequency travel in opposite directions, interference between these two waves produces a standing wave pattern in the optical field intensity. This interference effect in the gain medium can produce a spatial modulation of the population inversion, which leads to multi-longitudinal mode operation even in spectrally homogeneous lasers. This is called spatial hole burning.[18] There are several ways to eliminate spatial hole burning.[19] One way is to put the laser rod between two quarter wave plates and place one linear polarizer between one wave plate and a laser end mirror.[20] In this configuration, counter-propagating, circularly polarized beams with the same handedness, with respect to a fixed coordinate system, are generated, and no standing wave can be formed inside the cavity. However, in practice, additional etalons are required to get mono-longitudinal mode operation because of residual spatial hole burning due to the thermally-induced birefringence.

Let us consider right circularly polarized light given by:

where $\hat{e}_+ = \begin{bmatrix} 1 \\ -i \end{bmatrix}$ is a Jones matrix representation for right circular polarized light.

When right circularly polarized light is incident on a conventional dielectric mirror, it experiences a 180° phase shift as a results of a direction change from the z to -z axis. The reflected field changes its polarization to left circularly polarized light. Interference between the two counter-propagating waves produces a standing wave pattern in revolution along the z direction, which can be derived as:

$$I_s = \left| 2E_0 \sin kz \, \mathrm{Re}\left[\hat{e}_+ e^{-i\omega t}\right] \right|^2 \tag{24}$$

The z dependence of intensity in Eq. (2) gives rise to spatial hole burning and multimode operation.

At normal incidence, when right circularly polarized light is incident on a CLC mirror, the reflected field preserves its original right circularly polarized state. In this case, the interference pattern between the counter-propagating waves is given by:

$$I_s = \left| 2E_0 \cos(\omega t) \mathrm{Re}\left[\hat{e}_+ e^{i k z}\right] \right|^2 \tag{25}$$

Equation (25) shows that the intensity is independent of z. Therefore, there will be no standing wave pattern; that is, no spatial hole burning in regions of a laser cavity where orthogonal polarizations counter-propagate.

The modified Mach-Zehnder interferometer in Fig. 3.13 was used to verify that the reflected field from the CLC mirror preserves its polarization sense upon reflection. The output of a diode-pumped Nd:YAG laser (Amoco Micro Laser) was converted to
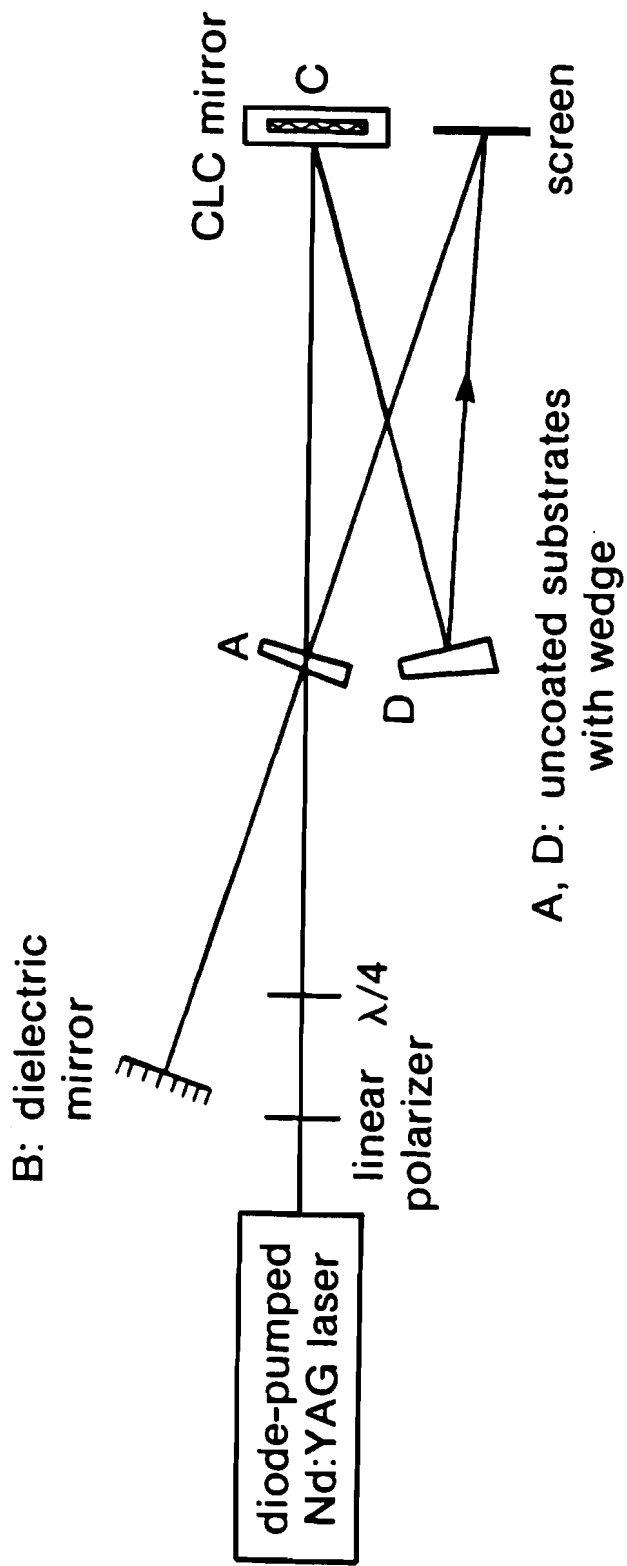
Fig. 3.13    Schematic diagram to verify that the reflected field from the CLC mirror keeps its polarization. Here, A and D are the pick-off glass wedges, B is a dielectric mirror, and C is a CLC mirror.

right circularly polarized light. A reference beam was directed onto a screen with an uncoated, glass wedge A and a dielectric mirror B. The second beam was generated with a right-handed CLC mirror C and an uncoated, glass wedge D. The two beams were recombined at the glass wedge D so that interference of the two waves would produce several tilt fringes on the screen. When a dielectric mirror was placed in C, fringe patterns were observed. However, when the dielectric mirror was replaced with a CLC mirror, no fringe patterns were observed, confirming the orthogonal polarization state of the two beams.

A commercial cw Nd:YAG laser (Control Laser Model 256) was used to demonstrate the mono-longitudinal mode as well as $\text{TEM}_{00}$ mode operation. The modified cavity configuration is illustrated in Fig. 3.14. The CLC-dielectric resonator consisted of a flat, dielectric R=90% output coupler, a $\lambda/4$ plate, a 54-mm long by 4-mm diameter Nd:YAG laser rod, a 10-mm thick Fabry-Perot etalon with R = 65% coatings, and a flat CLC mirror. The cavity length was about 38 cm. Our CLC mirror consisted of a blend of nematic liquid crystal ZLI 1167 and a chiral additive CB15, tuned to exhibit a selective reflection peak at 1064 nm. The CLC fluid thickness was 12 $\mu$m and its reflectivity was 98%. The output power was 1 W cw at 11 A lamp current. For this configuration, light propagating in the region between the $\lambda/4$ plate and the dielectric mirror is linearly polarized, whereas the light between the $\lambda/4$ plate and the CLC12-11 mirror (see nomenclature in Chap. 1) is circularly polarized. In order to confirm the mono-longitudinal mode operation, the output from the resonator was sent to a Fabry-Perot interferometer with R = 50% coated mirrors separated by 6 cm, and then imaged onto a CID camera via a single lens with focal length f = 570 mm. The etalon inside the cavity was easily adjusted to show mono-longitudinal mode operation as shown in Fig. 3.15(A). In this case, the free spectral range was
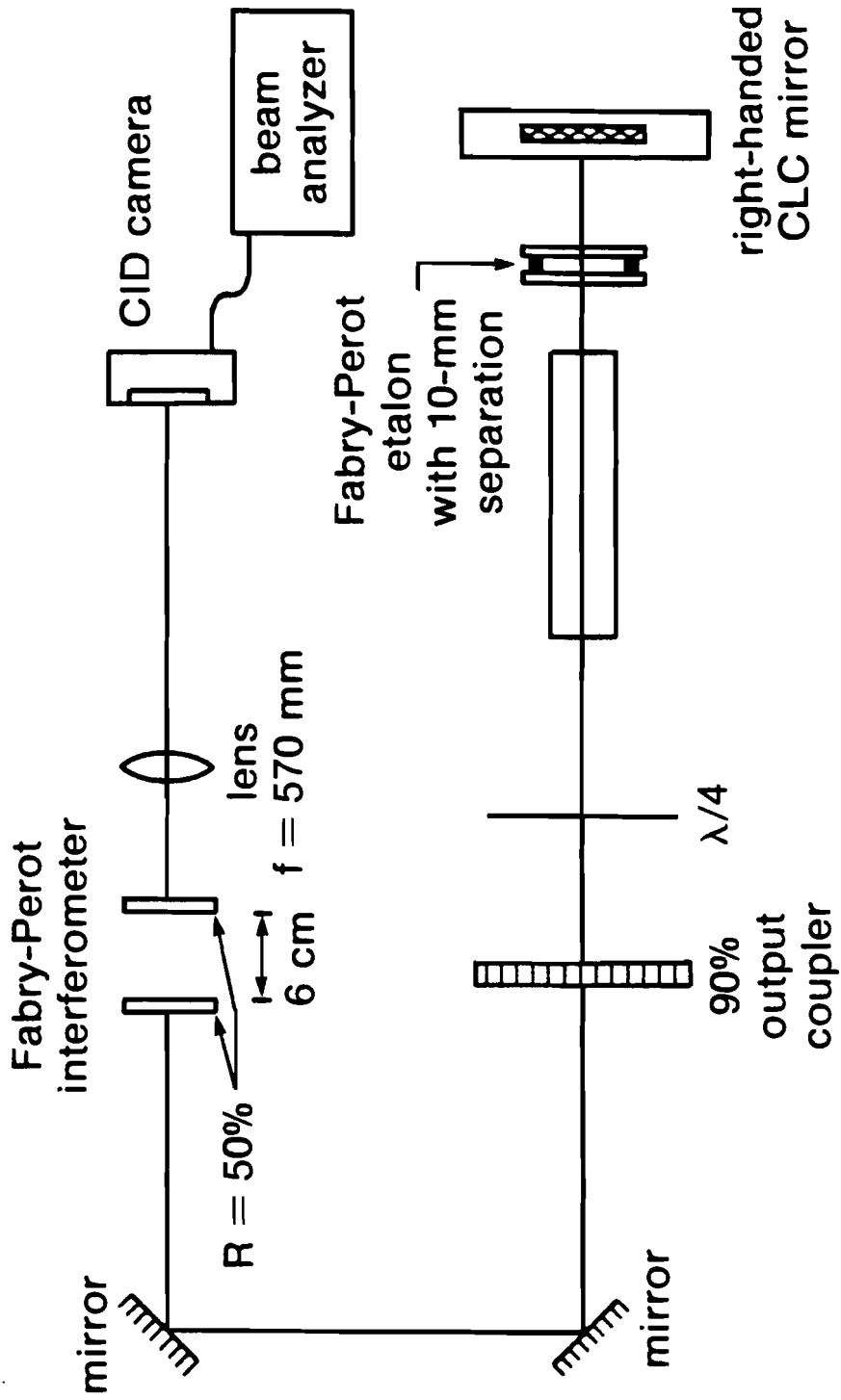
Fig. 3.14   Experimental setup for TEM$_{00}$ mode and mono-mode operation in a CLC-dielectric cavity.

(a)

(b)
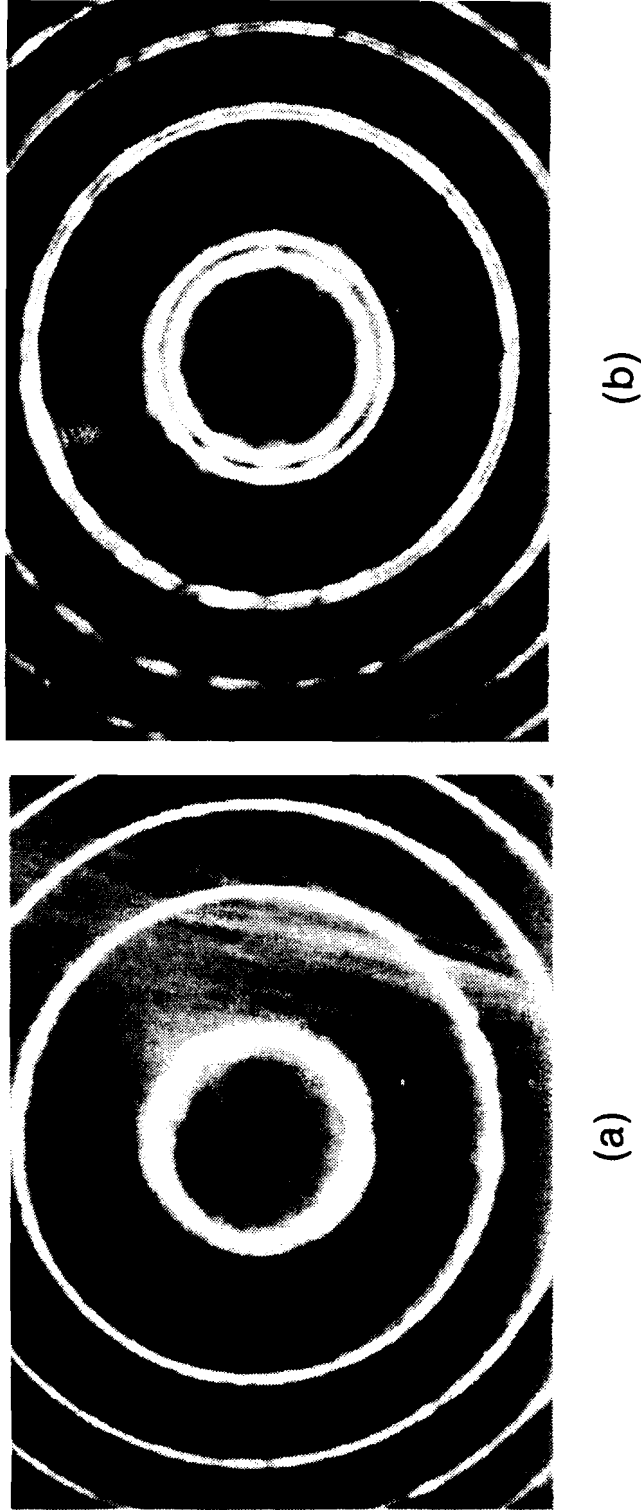
Fig. 3.15    Fabry-Perot interferogram of a CLC-dielectric cavity:   (a) One single longitudinal mode;  (b) Two adjacent modes. The free spectral range is equal to 2.5 GHz.

2.5 GHz. This mono-longitudinal mode operation was extremely stable for periods of half an hour (duration of the experiment). No special precautions to isolate the laser system from thermal or mechanical perturbations were taken. The etalon inside the cavity was also readjusted for lasing on two adjacent modes as shown in Fig. 3.15 (B). However this two mode operating state was not stable. The output beam pattern was also recorded with a CID camera at a distance of 2 m from the output coupler and is shown in Fig. 3.16. A Gaussian fit of the output intensity distribution shows that a Gaussian beam was indeed generated inside the resonator as a result of the pinholing effect, simultaneous with the mono-longitudinal mode lasing condition. Replacement of the CLC mirror with a dielectric HR mirror resulted in the multi-longitudinal mode operation. However near threshold current (10A), mono-longitudinal mode operation was observed.

The slope efficiencies were measured for a flat-flat dielectric resonator with a cavity length of 40 cm, with and without a pinhole in the all dielectric mirror cavity for $TEM_{00}$ mode generation, and for a CLC-dielectric resonator. The results are shown in Fig. 17. The slope efficiency for the flat-flat dielectric resonator was steepest but multi-spatial mode. For the flat-flat dielectric resonator configuration with a pinhole, the slope efficiency was almost the same as that for the CLC-dielectric resonator but its threshold current was about 20% higher. However, the output from the CLC-dielectric resonator was simultaneously $TEM_{00}$ mode and mono-longitudinal mode with comparable threshold current. $TEM_{00}$ mode output was maintained until the cw output power reached 1.3 W. Higher order modes evolved at output powers between 1.3 W and 3 W. Any depolarized light due to thermally-induced birefringence is filtered out on each round-trip path because of the polarization selectivity of the CLC end mirror. Angular insensitivity and low threshold current are additional advantages of a resonator
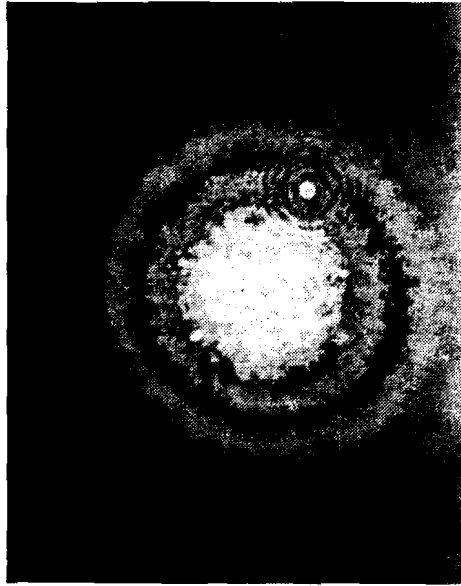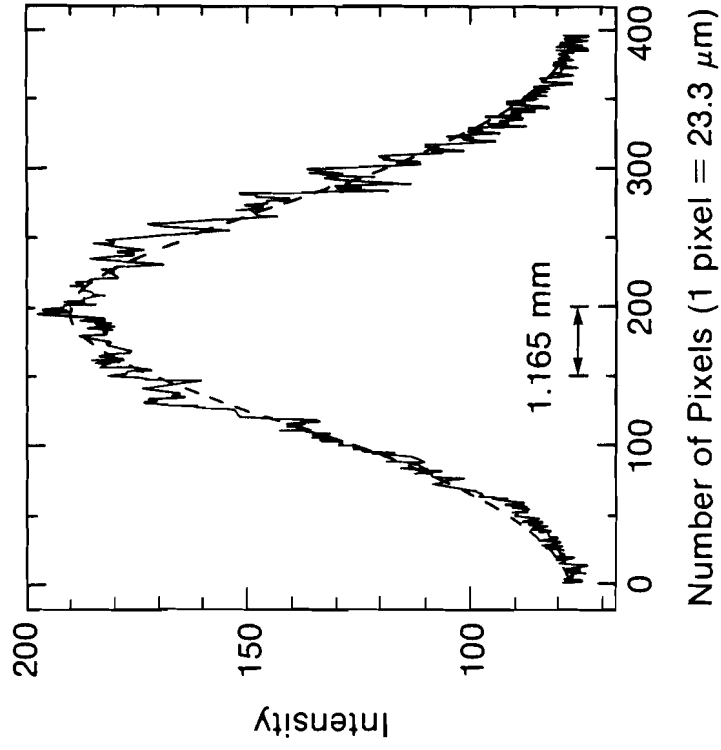
Fig. 3.16    The spatial profile of the CLC-dielectric resonator output at a lamp current of 11 A and its Gaussian fit to the center of the beam. The spikes in the spatial intensity profile are artifacts caused by multiple reflections from the neutral density filters in front of the CID camera.
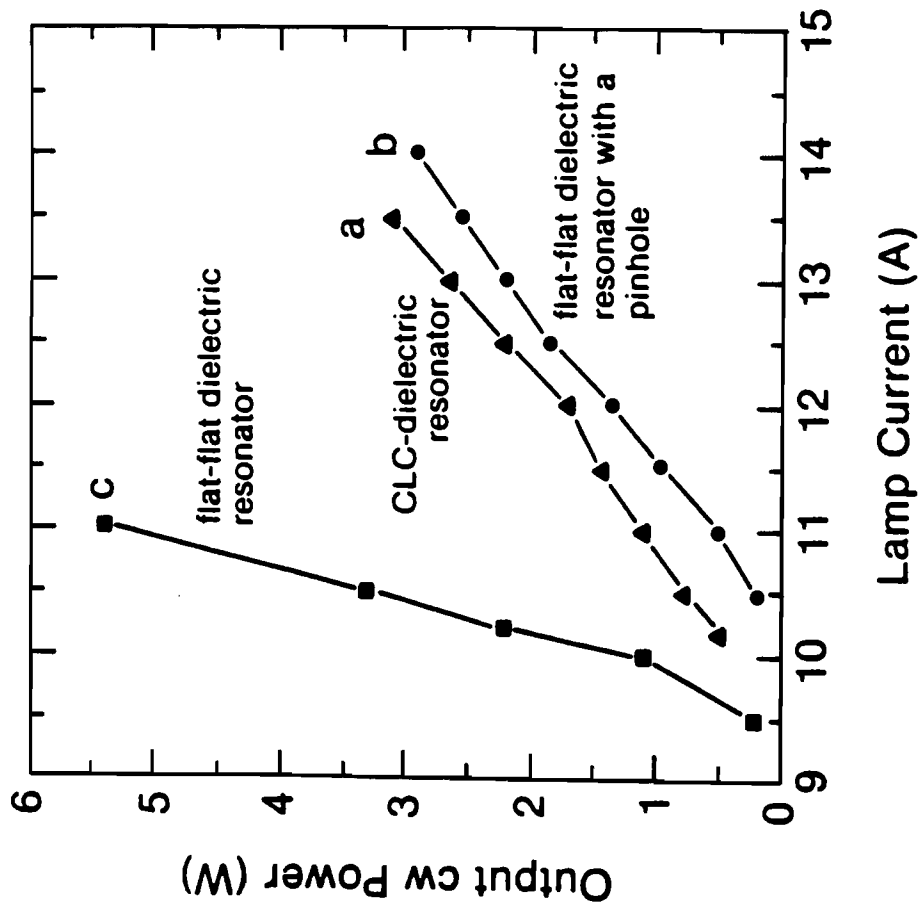
Fig. 3.17    The slope efficiencies for:  (a) a CLC-dielectric resonator and a flat-flat dielectric resonator with (b) or without (c) a mode selecting intra-cavity pinhole.

In conclusion, we have shown that CLC mirrors can be used as laser end mirrors in a solid state laser oscillator to provide both single longitudinal mode and $TEM_{00}$ mode operation for cw powers in excess of 1 W. No pinhole is required to obtain $TEM_{00}$ mode operation. Long-term single mode stability can be maintained without complicated thermo-mechanical isolation aids.

# REFERENCES

1.  I. P. II'chishin, E. A. Tikhonov, V. G. Tishchenko, and M. T. Shpak, "Tuning of the Emission Frequency of a Dye Laser with a Bragg Mirror in the Form of a Cholesteric Liquid Crystal," Sov. J. Quantum. Electron. 8, 1487 (1978).

2.  Yu. V. Denisov, V. A. Kizel, V. A. Orlov, and N. F. Perevozchikov, "Properties of Radiation Emitted by a Laser with Liquid Crystal Reflectors," Sov. J. Quantum Electron. 10, 1447 (1980).

3   Jae-Cheul Lee and S. D. Jacobs, "Design and Construction of Liquid Crystal Laser End Mirrors," submitted for publication to Appl. Phys. Lett.

4.  G. R. Fowles, Introduction to Modern Optics, 2nd ed. (Holt, Rinehart and Winston,Inc., 1975), pp. 33–38.

5.  Jae-Cheul Lee, J. H. Kelly, D. L. Smith, and S. D. Jacobs, "Gain Squaring in a Cr:Nd:GSGG Active-Mirror Amplifier Using a Cholesteric Liquid Crystal Mirror," IEEE J. Quantum Electron. 24, 2238 (1988).

6.  S. D. Jacobs, "Liquid Crystals for Laser Applications," Optical Materials - Properties, edited by M. J. Weber, Part 2, 409-465 (CRC Press, Boca Raton, FL, 1986).

7.  W. U. Müller and H. Stegemeyer, "Birefringence of Compensated Cholesteric Liquid Crystals," Berichte der Bunsen-Gesellschaft, Bd. 77, Nr. 1, 20 (1973).

8.  J. C. Lee, S. D. Jacobs, and R. J. Gingold, "Nd:YAG Laser with Cholesteric Liquid Crystal Cavity Mirrors," Advances in Nonlinear Polymers and Inorganic Crystals, Liquid Crystals, and Laser Media (SPIE, Bellingham, WA, 1988), Vol. 824,7–17

9.  J. C. Lee, S. D. Jacobs, and A. Schmid, "Retro-Self-Focusing and Pinholing Effects in a Cholesteric Liquid Crystal," Mol. Cryst. Liq. Cryst. 150b, 617 (1987)

10. GE model TN 2505; array size: 248 V x 388 H pixels; pixel size: 27.3 μ x 23.3 μm.

11. G. R. Fowles, Introduction to Modern Optics, 2nd ed. (Holt, Rinehart and Winston,Inc., 1975), pp. 174.

12  P. E. Cladis, "New Method for Measuring the Twist Elastic Constant $k_{22}/\chi_a$ and the Shear Viscosity $\gamma/\chi_a$ for Nematics," Phy. Rev. Lett. 28, 1629 (1972)

13. Vittorio Magni, "Resonators for Solid-State Lasers with Large-Volume Fundamental Mode and High Alignment Stability," Appl. Opt. 25, 107 (1986).

14. Joseph T. Verdeyen, Laser Electronics (Prentice-Hall, Englewood Cliffs, NJ, 1981), pp. 94–95.

15. Daniel Malacara, Optical Shop Testing (Wiley, New York, 1978), pp. 105-111.

16. Beam Scan, Model 1086-16, Photon, Inc.

17. Jae-Cheul Lee, S. D. Jacobs, T. Gunderman , A. Schmid, T. J. Kessler, M. D. Skeldon, "$TEM_{00}$ mode and Mono-mode Operation with a Cholesteric Liquid Crystal as a Laser End Mirror," to be submitted to Opt. Lett. for publication.

18. A. Siegman, Lasers (University Science Books, 1986) pp. 462–466.

19. W. Koechner, Solid-State Laser Engineering (Springer-Verlag, 2nd Ed., 1988) p. 126, 223.

20. D. A. Draegert, "Efficient Single-Longitudinal Mode Nd:YAG Laser," <u>IEEE J. Quantum Electron.</u> <u>8</u>, 235 (1972).

# CHAPTER IV

# Cr:Nd:GSGG Active-Mirror Amplifier Incorporating Liquid Crystals

Recently Gadolinium Scandium Gallium Garnet (GSGG) has emerged as an important laser host material for solid state lasers. This material has some advantages relative to YAG. Some of the reasons are as follows:[1] First, GSGG crystal boules of high optical quality can be grown by the Czochralski method. Second, YAG host material cannot be sensitized with chromium ions to improve its efficiency under broadband flashlamp pumping, nor can it be doped with a high concentration of neodymium ions. When a large boule of GSGG is grown, chromium ions can be uniformly doped into the material and neodymium can be doped with about four times higher concentration than in YAG. Third, GSGG has about two times better coupling efficiency of the flash lamp light relative to Nd:YAG when it is doped with chromium and neodymium. In the design of solid state lasers using this new material, the refractive index, n, and the temperature variation of refractive index, $\Delta n/\Delta T$, are important because the temperature variation of the refractive index is responsible for thermal lensing that occurs when solid-state laser rods are pumped. This thermal lensing can cause a degradation in the beam quality. In order to compensate the thermal lensing effect, the magnitude of the thermal lensing must be known. In this chapter, we measure n and $\Delta n/\Delta T$ for Cr:Nd:GSGG using a refinement of the conventional minimum angle of deviation (MAD) technique[2,3] at 1064 nm and we will describe how a simple liquid crystal device can be used to square the small signal gain in a Nd:Cr:GSGG active mirror amplifier.

93

# 1. Refractive Index and Δn/ΔT measurement of Cr:Nd:GSGG at 1064 nm[3]

For the MAD technique, consider the laser beam passing through the prism in Fig. 4.1. The beam which passes through the prism strikes the screen behind the prism. As the prism is rotated through the minimum deviation angle, the spot at the screen moves through its extreme point and then reverses its direction. But if the sample is fixed at minimum deviation angle, the refractive index change due to temperature will cause the spot to move away from its extreme point on the screen. Δn/ΔT can be determined by measuring the displacement of the spot from the original position. At minimum deviation angle, light passes through the prism symmetrically with equal refraction at both surfaces, and one has:

$$n = \frac{\sin i}{\sin r} = \frac{\sin \frac{\theta + \alpha}{2}}{\sin \frac{\alpha}{2}} \tag{1}$$

where i indicates the incidence angle of the beam on the prism, r the angle of refraction, which equals $\alpha/2$ at minimum deviation angle, $\alpha$ the apex angle of the prism, n the refractive index, and the angle $\theta$ between the initial and final directions of the ray is the angle of deviation. Since n is a function of temperature, the angle $\theta$ in Eq. (1) will change with temperature. When the angle $\theta$ is changed due to temperature by $\Delta\theta$, we have:

$$\Delta n = \frac{\sin\dfrac{\theta + \Delta\theta + \alpha}{2}}{\sin\dfrac{\alpha}{2}} - \frac{\sin\dfrac{\theta + \alpha}{2}}{\sin\dfrac{\alpha}{2}}$$

$$= \frac{2\cos\left(\dfrac{\theta + \alpha}{2} + \dfrac{\Delta\theta}{4}\right)\sin\dfrac{\Delta\theta}{4}}{\sin\dfrac{\alpha}{2}} \tag{2}$$

where $\Delta\theta$ indicates the change of angle $\theta$ due to temperature and $\Delta n$ is the change of refractive index n. Dividing both sides by $\Delta T$, we have:

$$\frac{\Delta n}{\Delta T} = \frac{2\cos\left(\dfrac{\theta + \alpha}{2} + \dfrac{\Delta\theta}{4}\right)\sin\left(\dfrac{\Delta\theta}{4}\right)}{\sin\dfrac{\alpha}{2} \bullet \Delta T} \tag{3}$$

where $\Delta T$ indicates temperature variation. To make a connection between $\Delta\theta$ and displacement $\Delta y$ of the spot due to temperature in Fig. 4.1, we have:

$$y + \Delta y \approx x\tan\left(\frac{\theta}{2} + \Delta\theta\right) \qquad x \gg b \tag{4}$$

$$x = \ell\cos\frac{\theta}{2} \qquad , \qquad y = \ell\sin\frac{\theta}{2} \tag{5}$$
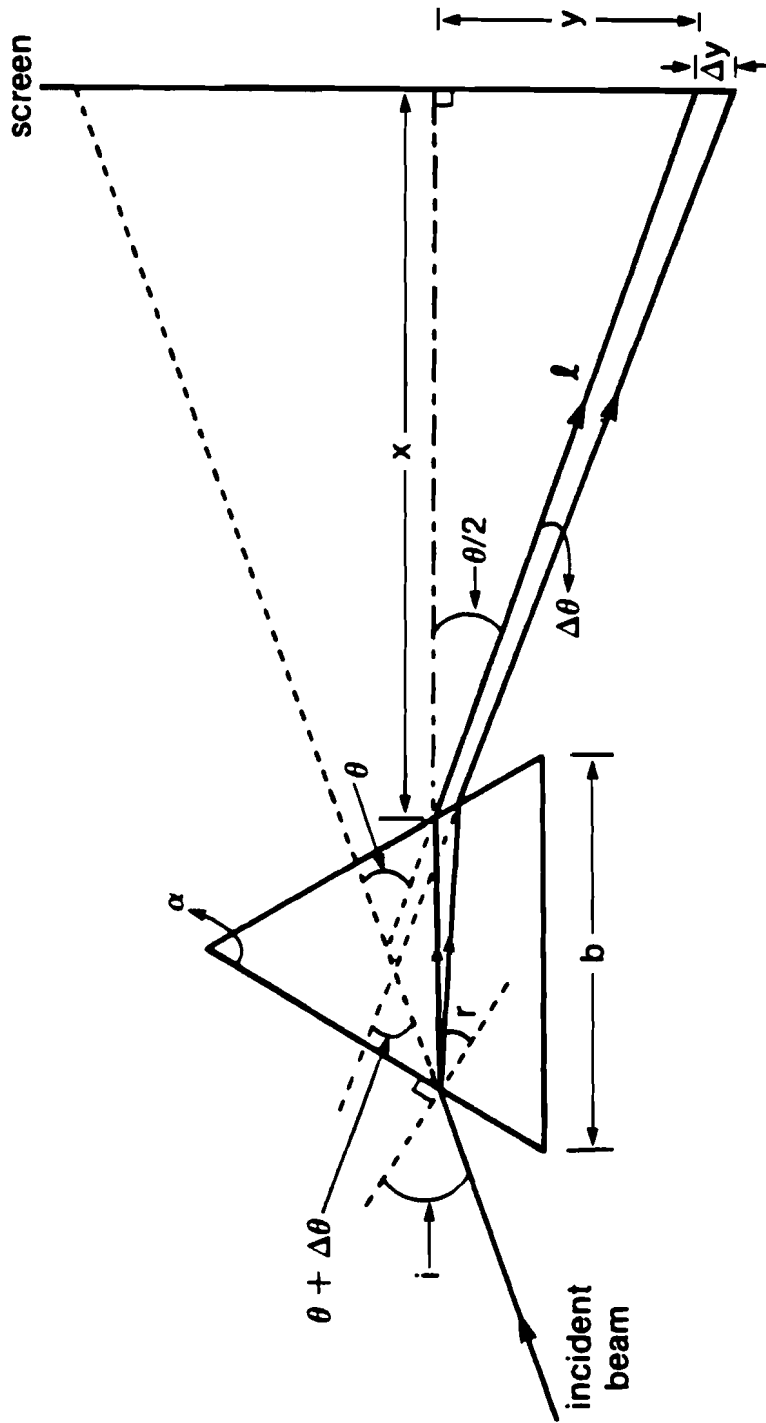
Fig. 4.1    Beam path geometry in prism for minimum angular deviation technique.

where x indicates the horizontal distance between screen and prism, b is a base length

of the prism and $\ell$ indicates beam path between the prism and the plane of observation.

Rearranging Eq. (4), we have

$$\Delta\theta = \tan^{-1}\left(\frac{\ell\sin\dfrac{\theta}{2}+\Delta y}{\ell\cos\dfrac{\theta}{2}}\right)-\frac{\theta}{2} \; . \tag{6}$$

Therefore, if we know the refractive index, n, we can calculate the angle $\theta$ from

Eq. (1) and once we measure path length $\ell$ of the beam and displacement $\Delta y$ of the

spot, we can calculate $\Delta\theta$ from Eq. (6). Accordingly we can obtain $\Delta n/\Delta T$ from

Eq. (3).

As it is well-known, the refractive index n can be measured as follows: First

read the angular setting of the rotation stage at minimum deviation angle, and then

rotate the rotation stage until retroreflection from the prism surface is obtained. The

difference in angular readings corresponds to the incidence angle i in Eq. (1).

Therefore, we can calculate refractive index of the material.

Figure 4.2 shows our experimental set-up. In order to find the spot position

and to find the turning point of the spot, we used a charge injection device (CID GE

Model TN2500, Array Size:248x244 pixels, pixel size: 46x36 μm). Data captured by

the CID controller was passed to a beam analyzer which consisted of a PDP-11/73 and
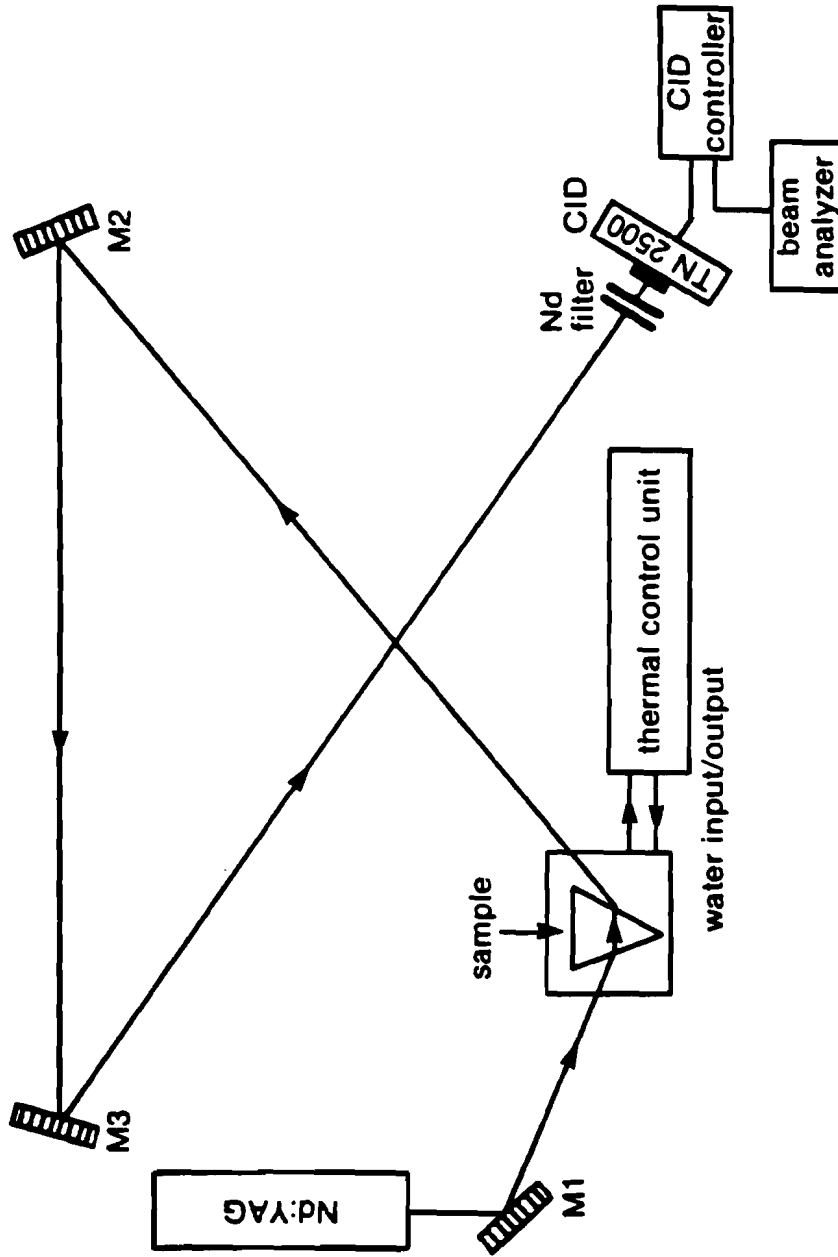
Fig. 4.2    Schematic diagram of the experimental setup.

beam analysis software. The means of determining the spot location was to use repetitive gaussian fits in the x and y direction to converge on the center location.

The YAG laser which was used in this experiment has 15 mw $TEM_{00}$ mode and good pointing stability ($\pm$ 1 pixel shift over 5 minutes). It consists of 3 mm x 65 mm YAG rod, cw pumped in an elliptical cavity with a 1000 W tungsten lamp.

The Cr:Nd:GSGG sample[5] has chromium concentration of 2 x $10^{20}$ ions/cc and neodymium concentration of 2x$10^{20}$ ions/cc. Table 4.1 shows its melt composition. The prism was prepared with $\lambda$/10 flatness on input and output faces and cut with striations parallel to the base. The apex angle of the prism was 45° $\pm$ 10 seconds.

We fabricated a prism housing for temperature control from aluminum plates which had a hollow internal flow path to allow for thermal control via water circulated from a thermal control unit (MGW, Lauda, Model RMS6) whose stability was $\pm$ 0.1°C. Plates were wrapped with foam insulation to minimize temperature loss. The prism was sandwiched between the aluminum plates with silicone heat sink compound. In this experiment, we did not measure the internal temperature of the prism sample, but instead waited for the spot position to settle down within $\pm$ 2 pixels on the array detector, which corresponds to $\pm$ 0.25x$10^{-6}$ of $\Delta n/\Delta T$.

In our experiment, we measured $\Delta n/\Delta T$ of undoped YLF[6] for the extraordinary refractive index to check the method and compare results with previous unpublished work.[7] We obtained good agreement as can be seen in Table 4.2. We measured the refractive index of Cr:Nd:GSGG at 10°C, aligned the prism to the minimum deviation angle, and then changed the temperature to get $\Delta n/\Delta T$. Table 4.2 shows our results. Balanova et al.[8,9] measured the refractive index of Cr:Nd:GSGG at 577 nm. (See

## Table 4.1   Composition of Cr:Nd:GSGG

| Elements<br>Samples | Gd | Nd | [Sc, Ga] | Cr | Ga | 0 |
|---|---|---|---|---|---|---|
| This Work (5) | 3.03 | 0.071 | 1.57 | 0.05 | 3.3 | 12 |
| Balavanova (9) | 2.93 | 0.070 | 1.75 | 0.25 | 3.0 | 12 |

## Table  4.2   Experimental data of Cr:Nd:GSGG

| Material | Apex<br>Angle $\alpha$ | Refractive<br>Index n | | $\Delta T$ from<br>$10°C$ | $\Delta n/\Delta T \times 10^6$ | |
|---|---|---|---|---|---|---|
| | | | | | This work | J. Rinefierd (7) |
| YLF | 60° 6" | $n_e$ | 1.4704 | +45° | −4.1 | −4.3 |
| | | $n_o$ | 1.4481 | | | −2.0 |
| Cr:Nd:GSGG | 45°±10" | 1.9424<br>± (0.0005) | | +20° | 10.7 (±0.3) | |
| | | | | +40° | 10.9 (±0.3) | |

Table 4.1 for the composition of their material.) They derived a single term Sellmeier formula for n which they claimed accurate to within $\Delta n = 10^{-3}$ at any wavelength in the visible and near IR. Using their formula we calculated a refractive index of 1.949 at 1064 nm. Our measured value of 1.9424 ($\pm$ 0.0005) differs by $6.6 \times 10^{-3}$ units. Hoefer et al.[10] measured $\Delta n/\Delta T$ of an undoped GSGG sample at 1064 nm and they obtained a room temperature value of $10.1 \times 10^{-6}$ by using a combination of Fizeau and Twyman-Green interferometry. In our work, for Cr:Nd:GSGG, $\Delta n/\Delta T = 10.7$ ($\pm$ 0.3)$\times 10^{-6}$ for $\Delta T = +20°C$ from 10°C and $\Delta n/\Delta T = 10.9$ ($\pm$ 0.3)$\times 10^{-6}$ for $\Delta T = +40°C$ from 10°C. The accuracy of our measurement can be improved with the use of an array detector which has better resolution and by measuring internal temperature of the sample in-process.

## 4.2 Gain Squaring in a Cr:Nd:GSGG Active-Mirror Amplifier Using a Cholesteric Liquid Crystal Mirror[11,12]

Active-mirror amplifiers (AMAs) have been demonstrated for use in laser fusion systems.[13] Unlike rod and disk amplifiers, AMAs are inherently double-pass devices, exhibiting larger energy extraction and compensation for thermally induced birefringence. In 1981, D. C. Brown et al., implemented a passively switched double/double-pass active-mirror amplifier ($D^2AMA$) system[14] (four passes of the active medium) which employed a polarizer, three (3) quarter wave plates, a series of AMAs and a dielectric mirror for sending the beam backward to make the second double pass. However, this system was quite complicated and several difficulties were encountered. Leakage occurred at the polarizer due to its imperfections and depolarization introduced by the active mirrors. This leakage caused a back-reflection to the driver line and laser oscillator. A much simpler alternative for multiple passing

of AMAs is suggested in this section, wherein a cholesteric liquid crystal (CLC) mirror is used to passively transmit and reflect laser radiation in front of an AMA.

In what follows, we explain how the unique properties of CLCs permit simple construction of a $D^2AMA$ system. Proof of the concept is demonstrated by measuring small-signal gain and beam quality for Cr:Nd:GSGG in a $D^2AMA$ configuration.

A high repetition rate active mirror is shown schematically in Fig. 4.3. It consists of a circular plate of the gain medium pumped from one side by a shape tailored array of flashlamps. The keys to the operation of the active mirror are the dielectric thin film coatings applied to the plate. The coating on the rear (pumped) side of the plate is highly reflecting at the gain wavelength and highly transmitting at the pump wavelengths. The front coating is the converse of the rear. In operation, both the beam to be amplified and the pump light double pass the gain medium for efficient extraction and absorption. Cooling is done through a major face only, to ensure that with uniform pumping, thermal gradients are parallel to the direction of propagation of the amplified beam. It is possible to simultaneously cool both major faces if a suitably transmissive coolant for the front can be identified. The circumference of the plate is angled and fine ground to defeat parasitic oscillations. A combination blastshield and UV filter protects the active medium from ultraviolet light emitted by the flashlamp array.

The setup for a $D^2AMA$ using a CLC is shown in Fig. 4.4. The right-handed CLC mirror described in the previous section is placed in front of the active mirror. The presence of the CLC causes the crystalline disc to be traversed four times, instead of the usual double pass. In this figure, the input probe beam from the GSGG oscillator, which is LH, is incident on the CLC mirror. No interaction occurs between
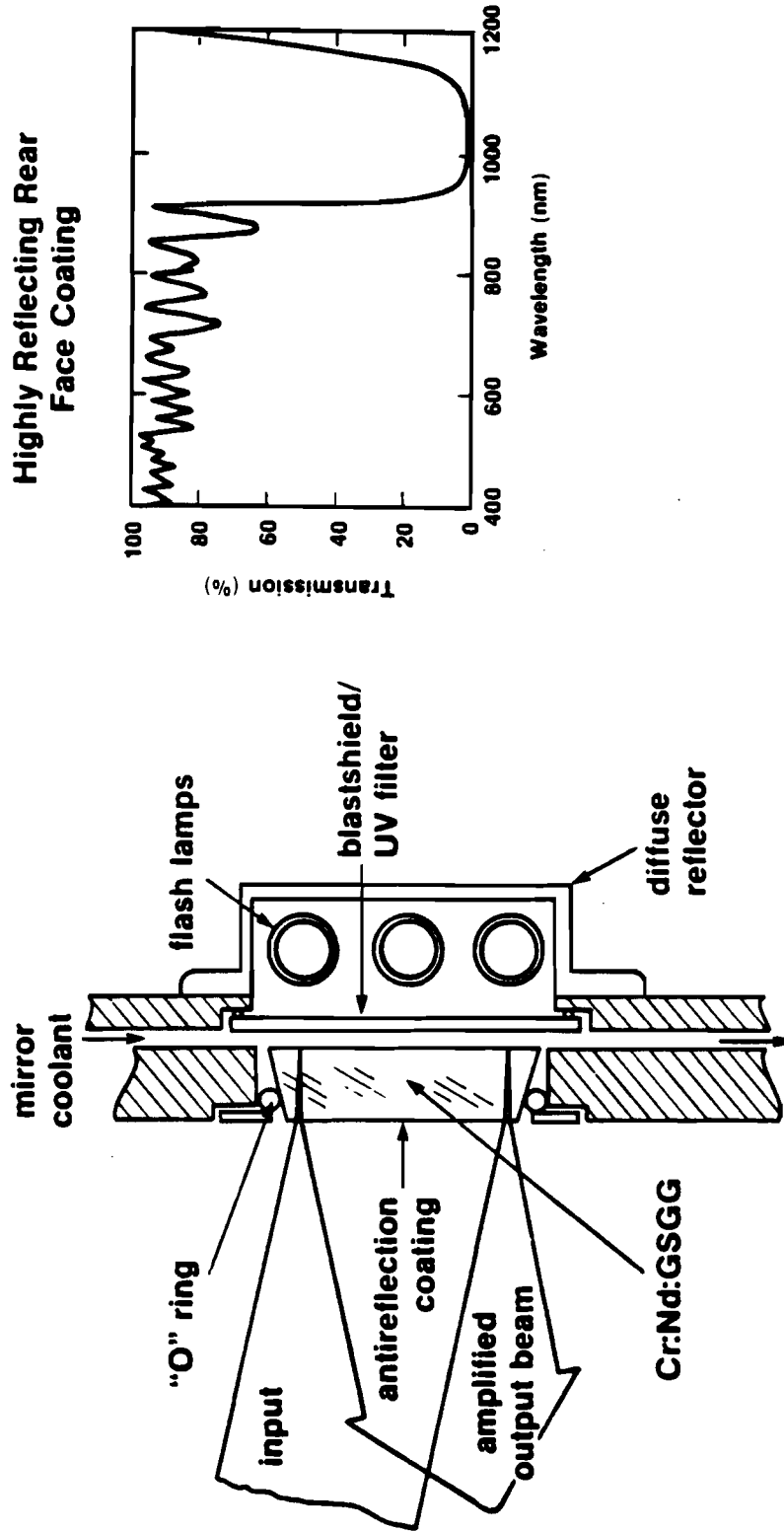
Fig. 4.3   High-repetition-rate active-mirror technology.
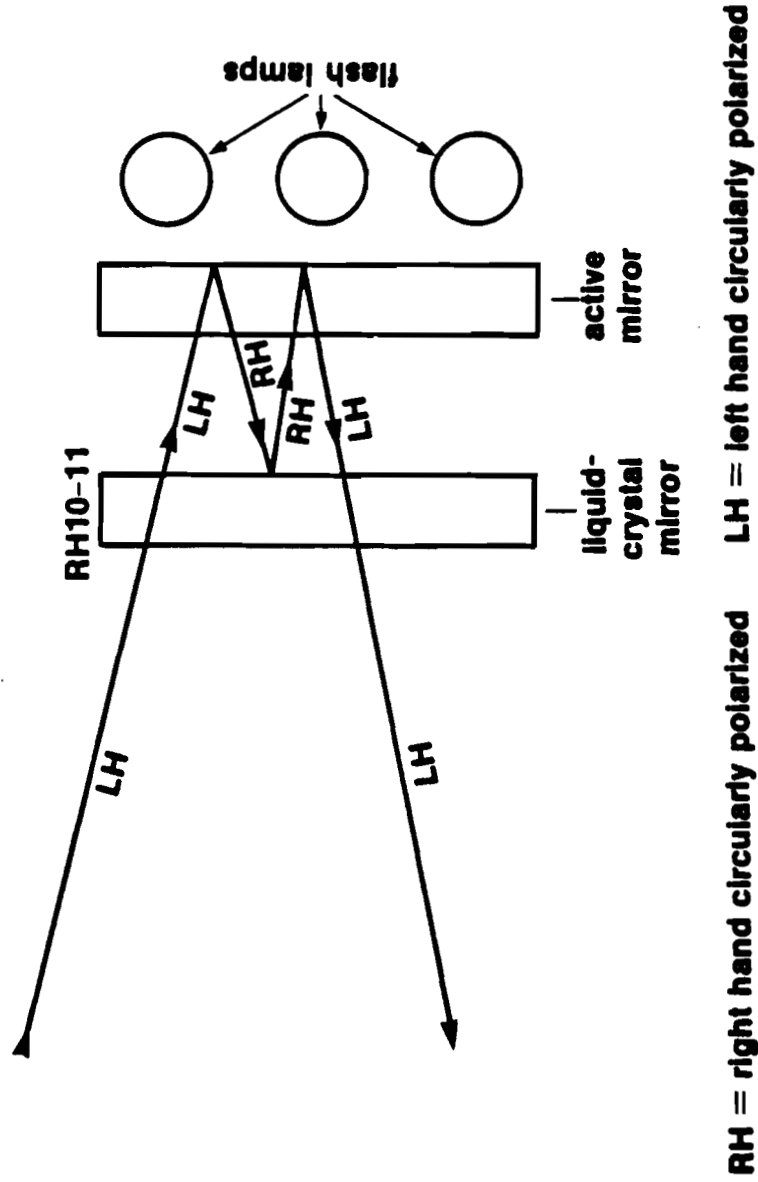
Fig. 4.4    Experimental setup for doubling number of passes in an active-mirror amplifier by insertion of a CLC element.

RH = right hand circularly polarized    LH = left hand circularly polarized

the right-handed helical structure of the CLC and the LH incident beam. It is transmitted to the rear, dielectric-coated side of the active mirror, where it reflects back with a change in polarization from LH to RH. Upon returning to the CLC, the beam is now reflected by the CLC because its handedness matches that of the CLC. There is no polarization change upon reflection from the CLC, however, and the beam proceeds as shown in the figure. One more reflection from the dielectric HR permits the beam to exit the CLC. As it is shown here, the beam makes a quadruple pass through the active-mirror gain medium due to the inherent nature of the active mirror being double passed. Therefore, one can get the square of the small-signal gain for the $D^2AMA$ configuration.

The small-signal gain of the active mirror was measured with and without the CLC mirror as a function of the bank energy as shown in Fig. 4.5. The probe beam from a Q-switched GSGG oscillator with a pulse width of 0.5 $\mu$s was attenuated to ensure that the small-signal gain was being measured. Our measurement utilized the ratio of ratios technique,[15] which eliminates any errors due to probe fluctuations. The small-signal gain at the maximum bank energy of 460 J, was 1.46 without the CLC and 2.05 with the CLC. This demonstrates that the small-signal gain can be approximately squared by placing a passive CLC mirror element in front of the active mirror. In the large signal regime, the use of this CLC element will result in increased extraction efficiency. [The slightly lower gain of this active mirror (1.46) compared to our previous result[12] (1.6) has been traced to a decreased pumping efficiency due to the large number (>350,000) of shots on the flash lamp reflector.]

The near-field pattern of the probe beam before and after injection was measured by using a CID camera. Contour plots of the incident and output near fields are shown in Fig. 4.6. No large beam defects were found as a result of the insertion
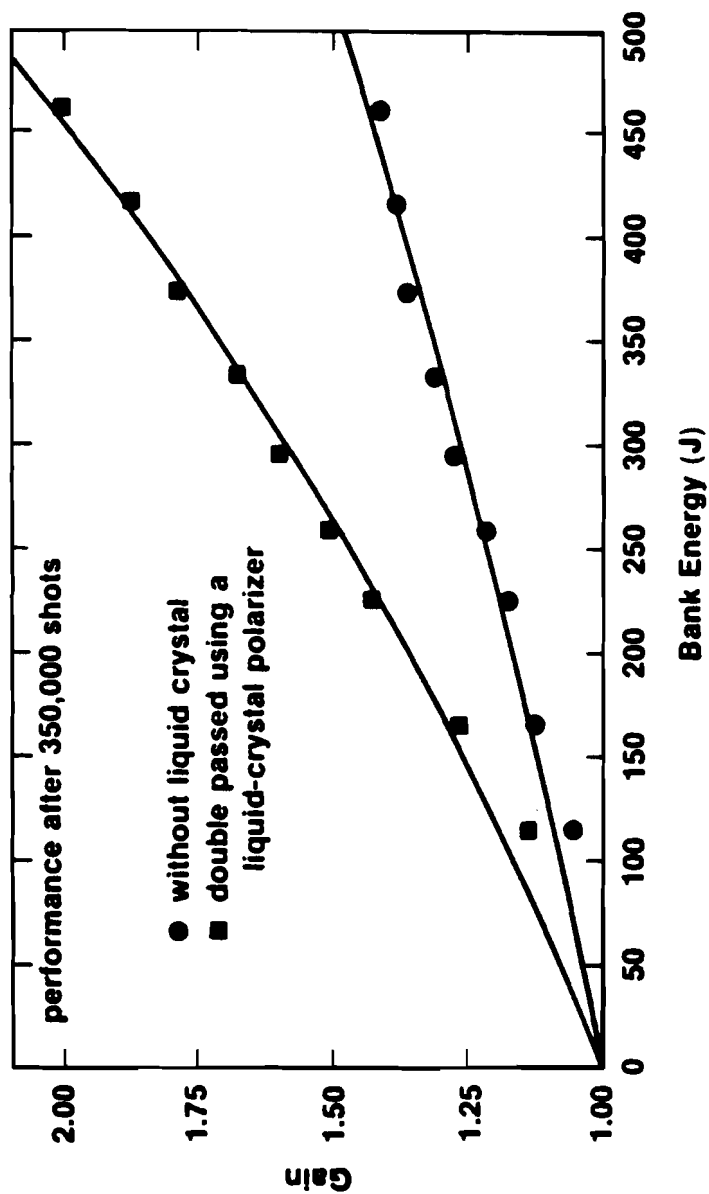
Fig. 4.5   Small-signal gain of the Cr:Nd: GSGG active-mirror amplifier with and without a liquid crystal for doubling the number of passes.

- **Good beam quality**

- **Maintains polarization; contrast ~ 200:1**
- **High system transmission T ~ 85% including active mirror**
- **Angularly insensitive ± 10°**
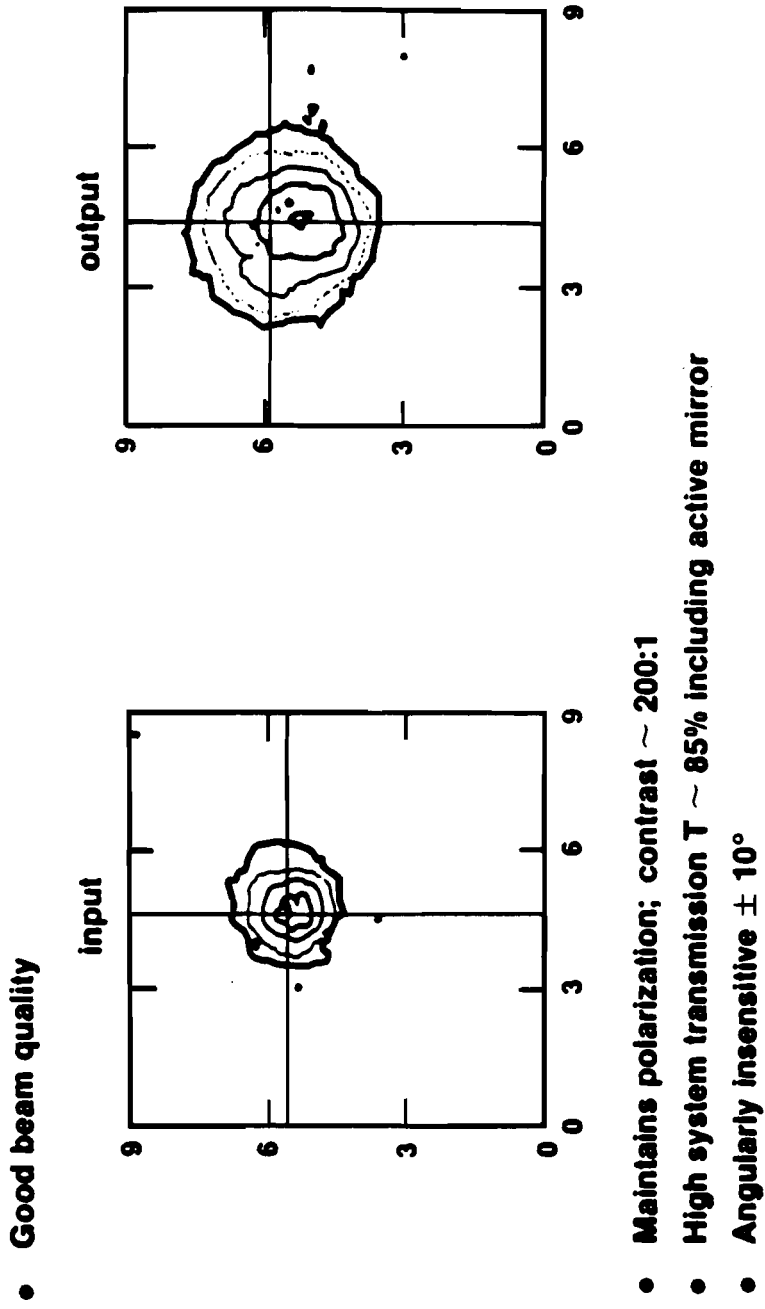
Fig. 4.6    Contour plots of the input and output beam as measured on a CID camera.    The change in level of intensity from one line to next line is 20 percent.

of the CLC although admittedly we could sample only over the relatively small (20 mm$^2$) area of our probe beam.

The passive contrast ratio was measured near the center of the active mirror with the CLC at near normal incidence. A $\lambda/4$ plate and a linear polarizer were placed in the output beam and the polarizer was rotated while measuring the output with an energy meter. The ratio of the maximum to minimum, averaged over 100 shots, was determined to be greater than 200:1. The angular sensitivity of the CLC was measured to be $\pm$ 10° for a 4% decrease in transmission.

In conclusion, we have squared the small-signal gain of a Cr:Nd:GSGG active-mirror amplifier using a passive, 10-$\mu$m thick, cholesteric liquid-crystal selective reflection mirror. This double/double-pass configuration was easy to align and solved difficulties, such as polarization leakage and back reflection coupling, which had plagued previous multi-pass schemes.

## REFERENCES

1. W. F. Krupke, M. D. Shinn, J. E. Marion, J. A. Caird, and S.E. Stokowski, "Spectroscopic, Optical and Thermomechanical Properties of Neodymium and Chromium-Doped Gadolinium Scandium Gallium Garnet," J. Opt. Soc. Am. B 3, 102 (1986).

2. R. S. Longhurst, Geometrical and Physical Optics, 2nd edition (New York: John Wiley & Sons, 1967), pp. 72–73

3. R. A. Sawyer, Experimental Spectroscopy, 3rd edition (New York: Dover, 1963), pp. 58–59.

4. J. C. Lee and S. D. Jacobs, "Refractive Index and $\Delta n/\Delta T$ of Cr:Nd:GSGG at 1064 nm," Appl. Opt. 26, 777 (1987).

5. Sample and compositional data provided by S. E. Stokowski, Lawrence Livermore National Laboratory (1986).

6. Provided by Sanders Associates Inc., Boule #538.3.

7. Unpublished data, J. Rinefierd and S. D. Jacobs, University of Rochester (1979).

8. S. A. Balabonova, E. V. Zharikov, V. V. Laptev, and V. D. Shigorin, P. N. Levedev Physical Institute Report 231, Moscow (1983).

9. S. A. Balabonova, E. V. Zharikov, V. V. Laptev, and V. D. Shigorin, "Refractive Indices of Rare Earth Gallium Garnets," Sov. Phys. Crystallog. 29, 704 (1984).

10. C. S. Hoefer, K. W. Kirby, and L. G. De Shazer, "Thermo-Optic Properties of Gadolinium Garnet Laser Crystals," J. Opt. Soc. Am. B 5, 2327 (1988).

11.   Jae-Cheul Lee, J. H. Kelly, D. L. Smith, and S. D. Jacobs, "Gain Squaring in a Cr:Nd:GSGG Active-Mirror Amplifier Using a Cholesteric Liquid Crystal Mirror," IEEE J. Quantum Electron. 24, 2238 (1988).

12.   J. H. Kelly, D. L. Smith, J. C. Lee, S. D. Jacobs, D. H. Smith, J. C. Lambropoulos, and M. J. Shoup III, "High-Repetition-Rate Cr:Nd:GSGG Active-Mirror Amplifier," Opt. Lett. 12, 996 (1987).

13.   J. A. Abate, L. Lund, D. Brown, S. Jacobs, S. Refermat, J. Kelly, M. Gavin, J. Waldbillig, and O. Lewis, "Active Mirror: A Large-Aperture Medium-Repetition Rate Nd:glass Amplifier," Appl. Opt. 20, 351 (1981).

14.   D. C. Brown, J. A. Abate, and J. Waldbillig, "Passively Switched Double-Pass Active Mirror System," Appl. Opt. 20, 1588 (1981).

15.   J. V. Meier, N. P. Barnes, D. K. Remelius, and M. R. Kokta, "Flash lamp-Pumped $Cr^{3+}$:GSAG Laser," IEEE J. Quantum Electron. 22, 2058 (1986).

# CHAPTER V

## Liquid Crystal Laser Beam Apodizers

Laser beam apodization has been a goal of solid state laser programs since the early 1970s. Apodization is the shaping of the spatial beam profile to increase the fill factor through the gain medium. This allows more energy to be extracted and also reduces linear and nonlinear edge diffraction effects which cause self-focusing spikes. Therefore a beam apodizer determines, to a large extent, the ultimate performance of a high power laser system.

An ideal beam apodizer possesses the following characteristics:[1]

1. The slope of the transmission function should be such that the radial distance between 90% and 10% transmission points is at least $3\lambda L/d$, where $\lambda$ is the laser wavelength, L is the propagation distance over which intensity modulation should be minimal, and d is the beam diameter. One of the transmission functions which approximates this condition is a super-Gaussian of order N, that is,

$$T(r) = \exp[-(r/r_0)^N] \qquad (1)$$

where the radial clear aperture $r_0$ is selected based on the condition that $T(r_1) = 10^{-3}$, where $2r_1$ is the entry aperture of the amplifying device that follows the apodizer.

2.   Wavefront quality over the clear aperture and into the soft edge is a smooth function with continuous first derivatives.

3.   The peak to minimum transmission ratio (contrast ratio) is at least 1000 to 1.

4.   High laser damage threshold at the design wavelength and pulse width.

5.   Environmental stability.

Several techniques for apodizing laser beams have been reported.[1-11] Recently, S. D. Jacobs et al. have developed a new apodizer based on liquid crystal technology that has demonstrated properties resembling those of a perfect apodizer.[12] However, their device concept works best for small clear apertures, and the exponential relationship used to model the reflectivity of their cholesteric liquid crystal (CLC) as a function of thickness is valid only as a first approximation.

In this chapter, we discuss several, different kinds of beam apodizers based on liquid crystal technology which can be used for beam apodization of slab-geometry amplifiers or diode lasers, and also for beam apodization of rod amplifiers with large clear apertures. In what follows, we will explore the design concepts for two CLC laser beam apodizers: one based on a gradient-index optical effects and the other based on fluid thickness variations. This chapter concludes with a description of a profile-tunable laser beam apodizer using nematic liquid crystals.

## 5.1   Cholesteric Liquid Crystal Laser Beam Apodizers[13]

From Eq. (23) in Chap. 2, the reflectivity of a CLC element is given by

$$R = \frac{\sinh^2 \kappa L \sqrt{1 - (\delta/\kappa)^2}}{\cosh^2 \kappa L \sqrt{1 - (\delta/\kappa)^2} - (\delta/\kappa)^2} \tag{2}$$

From this equation, one can find three different ways to shape the reflectivity profile:

- by varying the CLC fluid thickness: L(r)

- by varying the coupling coefficient : κ(r)

- the combination of the two above methods

For these concepts, weak anchoring at one side or at both sides is required to avoid any disinclination lines in the molecular structure[14] which could cause diffraction.


## 5.1.1  CLC beam apodizer utilizing fluid thickness variations

Geometrical constraints to liquid crystal apodizer construction using previous designs[12] make scale-up to apertures greater than 6 mm difficult. These difficulties are eliminated by designing an apodizer which consists of a single, homogeneous CLC fluid between a plano-convex lens with radius of curvature, $\rho$, and a plano-concave lens with radius of curvature, $\rho'$. The two substrates have slightly different inner radii of curvature. Index matching between fluid and substrate lens elements is important to remove focusing. This requires that the average refractive index of the substrates should be within 1% of the $n_{av}$ of the fluid to keep $\lambda/4$ wavefront quality. The gap thickness between the two substrates is given by

$$L(r) = \frac{r^2}{2\rho} \left[1 - \frac{\rho}{\rho'}\right]$$

(3)

The transmission profiles for $\rho/\rho' = 0.863$ and $\rho/\rho' = 0.9$ with $\rho = 1033.4$ mm are shown in Fig. 5.1 as two solid lines. As $\rho/\rho'$ increases, that is, as the radii of curvature for the two substrates approach each other, the clear aperture of the apodizer increases. In this figure, the dotted lines represent a super-Gaussian fit to the transmission profiles. Both fits show that the order of super-Gaussian is N = 3.51.
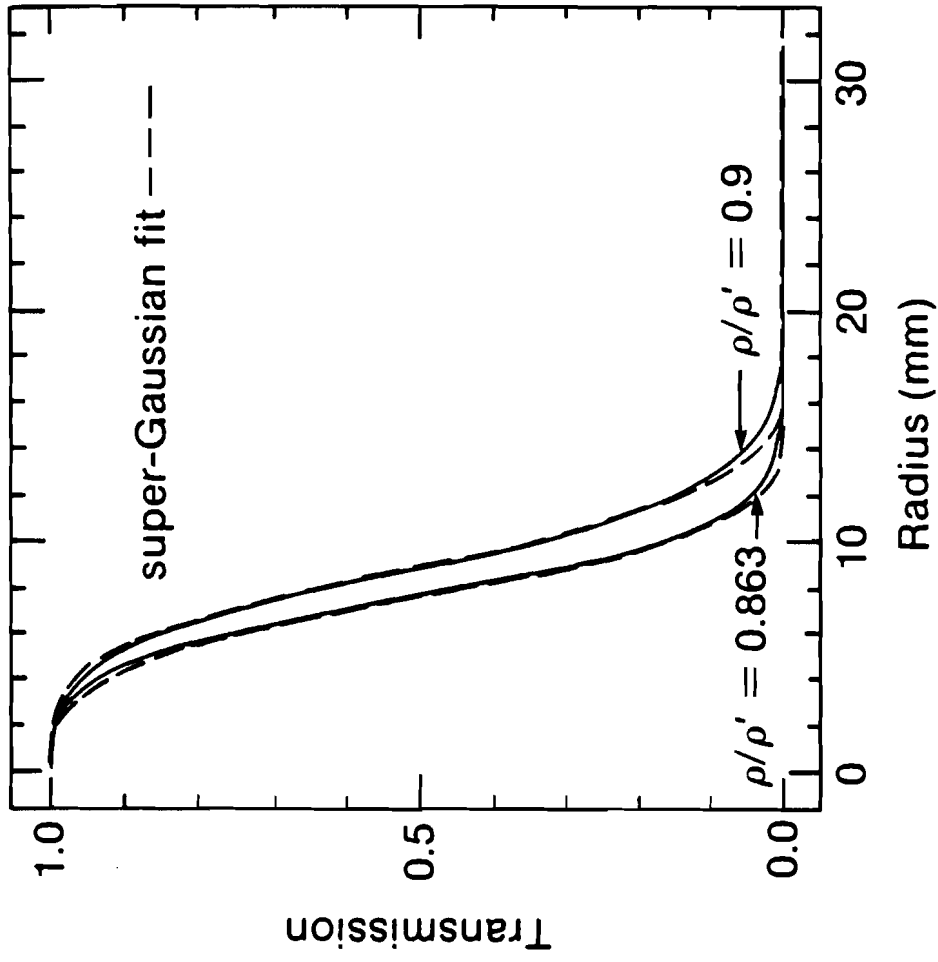
Fig. 5.1    Calculated edge transmission profiles for two CLC beam apodizers with $\rho/\rho' = 0.863$ and $\rho/\rho' = 0.9$ [two solid lines]. Here dotted lines represent super-Gaussian fits for each case.

As long as the CLC fluid thickness is varied according to Eq. (3), the order of the apodizer is invariant and equal to N = 3.51 for this design.

Two 50.8-mm diameter borosilicate glass (BK-7) substrates with $\rho$ = 1033.4 mm and $\rho'$ = 1197.5 mm were obtained and assembled into a cell using the curved surfaces as inner walls as shown in Fig. 5.2. The air gap was filled by capillary action at 60°C with a homogeneous mixture of E7 and CB15 tuned to 1064 nm (refer to Chap. 1 for fabrication). The experimental setup used to measure apodizer transmission profiles is shown in Fig. 5.3(a). The output of a diode-pumped Nd:YAG laser (Amoco Micro Laser @ 1064 nm) is converted to right circularly polarized light, collimated and focussed onto a CLC cell (spot size; 500 µm). The cell is scanned by passing through the beam on a translation stage. Transmitted light intensity is measured using a photodiode detector (United Detector Technologies, UDT-10). The measured (circles) transmission for the device at 22°C and calculated (solid line) profiles as a function of radius are shown in Fig. 5.3(b). Super-Gaussian fits to both curves (dashed lines) give N = 3.51 ($r_0$ = 8.5 mm) for the theoretical data and N = 3.52 ($r_0$ = 9.9 mm) for the experimental data. Local misalignment of molecules in the CLC can cause the coupling coefficient to be lower than the theoretical value, explaining the above discrepancy.

An apodizer with a true super-Gaussian transmission function can be obtained by adjusting the CLC fluid thickness as a function of the radius to satisfy the following condition:

$$T(r) = \exp\left[-(\frac{r}{r_0})^N\right] = 1 - \tanh^2 \kappa_0 L(r) \tag{4}$$

gap thickness

$$L(r) = \frac{r^2}{2\rho}\left[1 - \frac{\rho}{\rho'}\right]$$
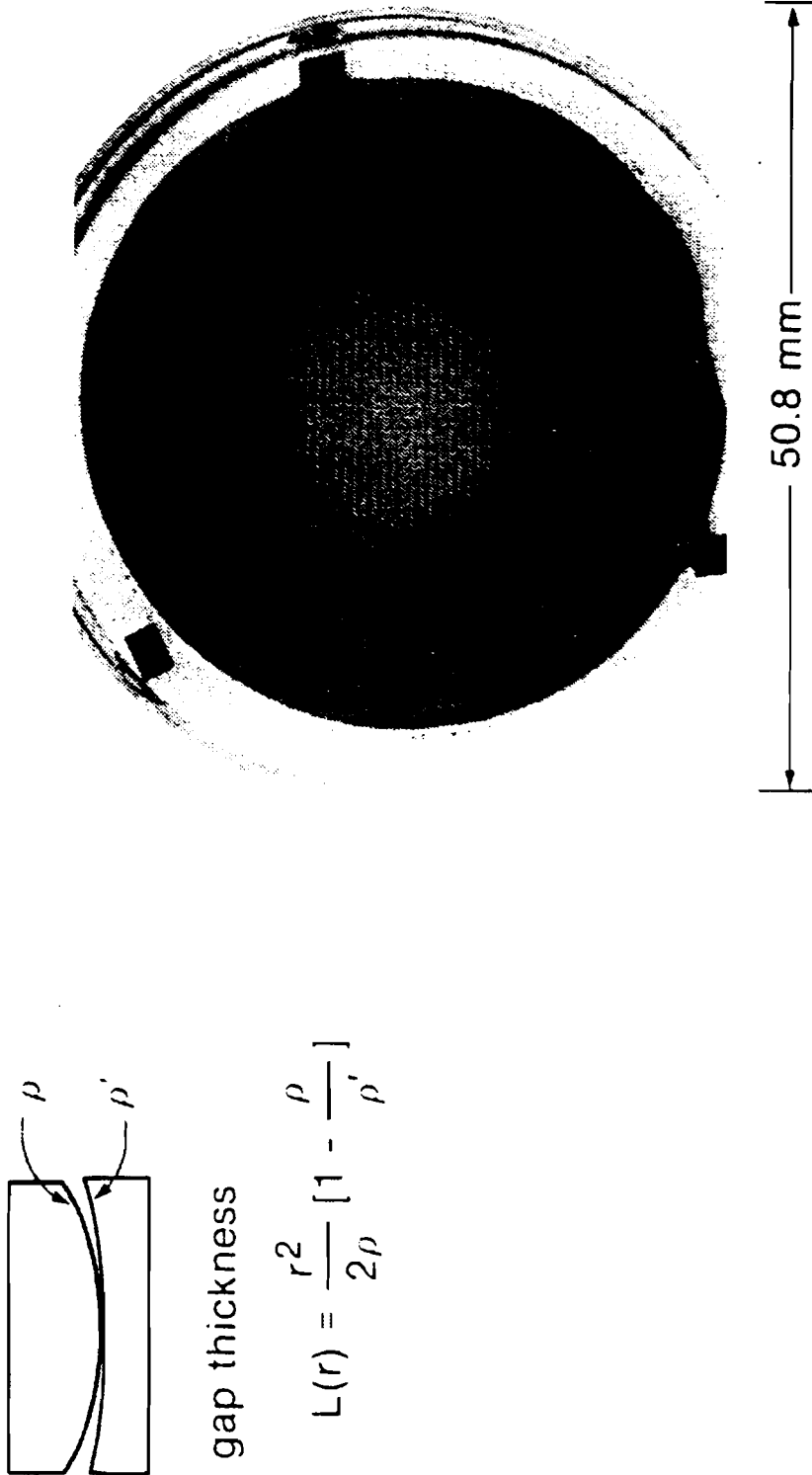
**Fig. 5.2** Photograph between linear polarizers, of a 1064-nm CLC circular beam apodizer made from off-the shelf plano-concave/convex lenses ($\rho = 1033.4$ and $\rho' = 1197.5$). The schematic diagram indicates the assembly orientation and the resulting relationship for fluid gap L, as a function of radial dimension r.
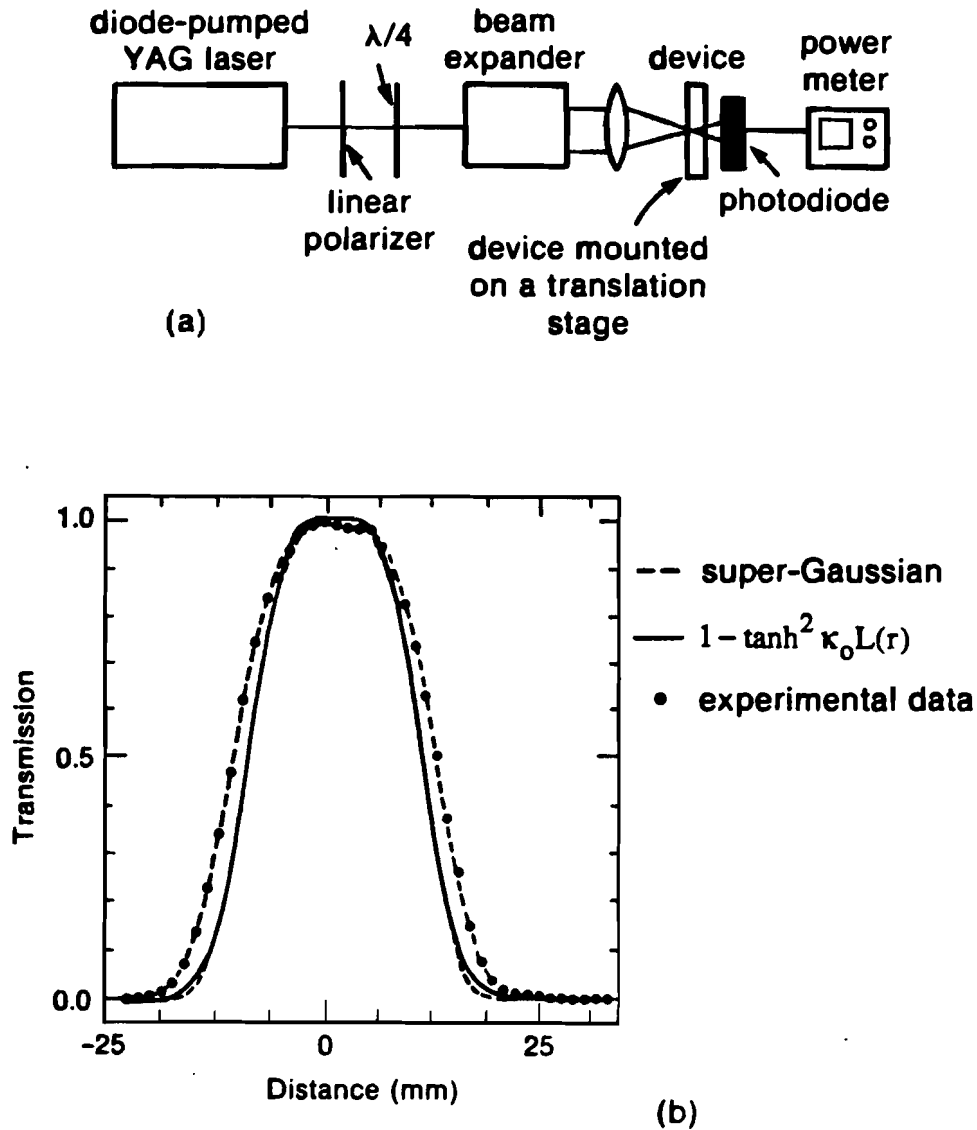
Fig. 5.3    (a) Experimental apparatus used to measure transmission profiles of

apodizers;  (b) Transmission profile at $\lambda = 1064$ nm, for a circular CLC

apodizer filled with a homogeneous fluid (mixture of E7 and CB15).

The solid line is the calculated transmission profile for an ideal case, the

circles are the experimental results and the dotted lines represent the best

super-Gaussian fit to the data (N = 3.51).

Then $\kappa_o L(r)$ is given by

$$\kappa_o L(r) = \tanh^{-1}\left[1 - \exp\left\{-\left(\frac{r}{r_o}\right)^N\right\}\right]^{1/2}$$

(5)

where $\kappa_o$ is the coupling coefficient and $L(r)$ is the CLC fluid thickness. A plot of $\kappa_o L(r)$ as a function of $(r/r_o)$ for $N = 5$ and $8$ is shown in Fig. 5.4(a). A consideration of molecular alignment imposes a restriction on the thickness variation beyond the clear aperture, a. The clear aperture, a, should be determined such that the contrast ratio is at least 1000 to 1. From Eq. (4), a is given by

$$a = \sqrt[N]{1.9326}\, r_o$$

(6)

A geometrical concept which implements this thickness variation is shown in Fig. 5.4(b). In this configuration, the CLC fluid is confined between a plane-parallel substrate and a plane-aspheric substrate. The aspheric profile is required on the inner surface of the second substrate only. A CNC (Computerized Numerical Controller) controlled diamond turning method could be used to make this aspheric surface. However this method restricts the choice of substrates to soft materials such as $CaF_2$ and PMMA. Since these materials have low refractive indices, their use imposes restrictions on the numbers of suitable liquid crystal compounds.

### 5.1.2 CLC apodizers utilizing gradient-index optical effects

In general, a super-Gaussian apodizer of order greater than 3.51 is required in high power laser applications to maximize output energy. This cannot be achieved
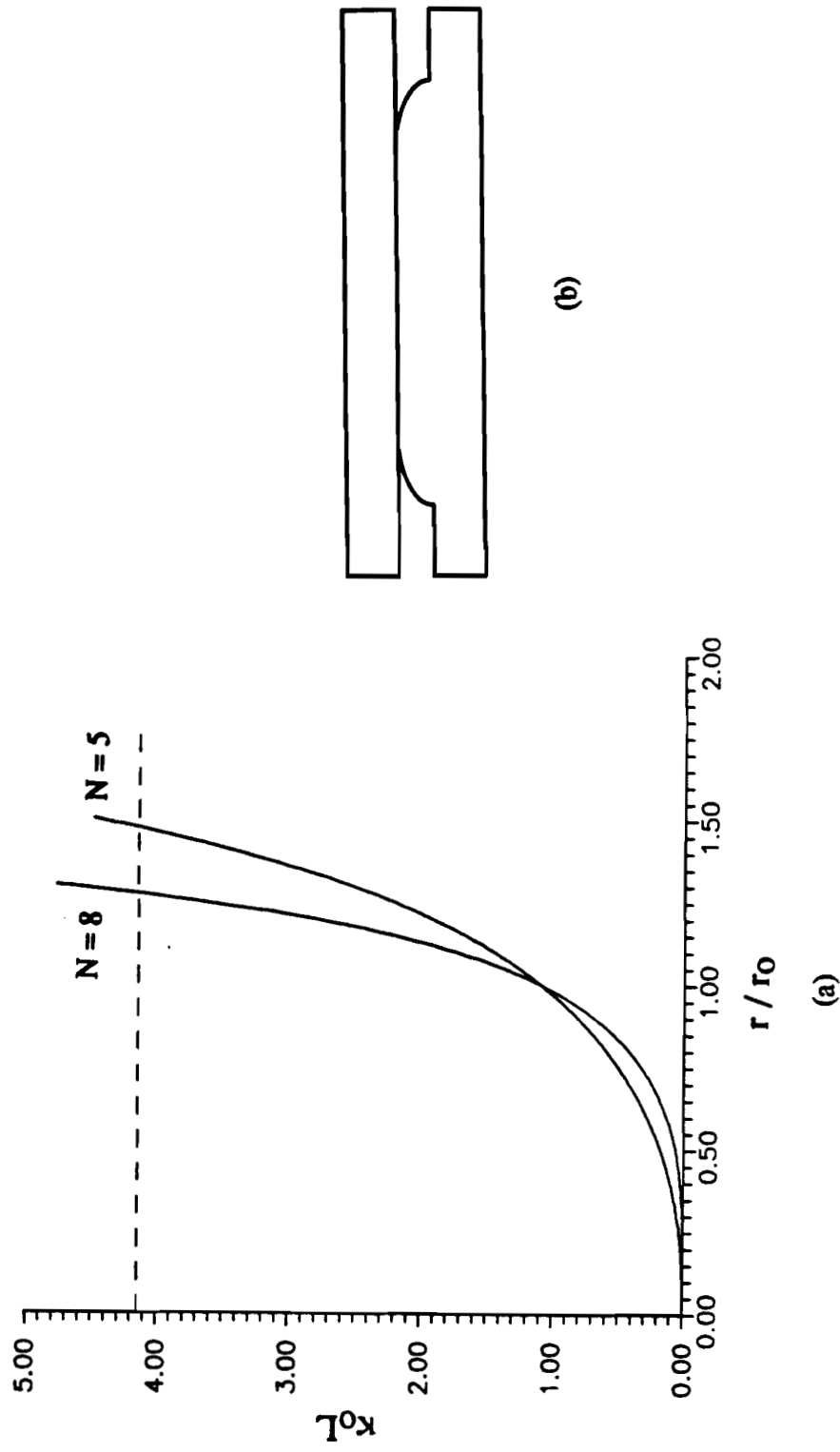
(a)

(b)

Fig. 5.4    (a) The $\kappa_0 L$ (or fluid thickness) variation required to get super-Gaussian $N = 5$ and 8.   The dotted line represents
the value of $\kappa_0 L$ to obtain the contrast ratio of 1000 to 1.
(b) A geometrical concept to implement the thickness variation described in (a).

with the simple, single fluid concept demonstrated above, because the order N of the super-Gaussian cannot be varied. The addition of a gradient index effect, however, permits orders greater than 3.51 to be constructed.

A spatial gradient in selective reflection peak wavelength can be induced by filling a device with mixtures of two CLC fluids, having different selective reflection bands, from opposite sides of a cell as shown in Fig. 5.5. The fluid-like properties of liquid crystals allow them to blend together in Region 3. This concept will be referred to as a gradient CLC (GCLC). The blending ratio (relative concentration) of chiral additives in the nematic liquid crystal host varies linearly in Region 3 from the Region 1 side to the Region 2 side. Since the helix wave number of the CLC, $q_0 = 2\pi/P_0$, is proportional to the concentration,[15] $\delta/\kappa$ in Eq. (2) can be rewritten as

$$\frac{\delta}{\kappa}(x) = \frac{2n_{av}}{\Delta n}\left(1 - \frac{q_0(x)}{k_0}\right)$$

$$= \frac{2n_{av}}{\Delta n}\left(1 - \frac{\lambda}{\lambda_0}\right) \tag{7}$$

where $k_0 = \frac{2\pi}{\lambda} \cdot n_{av}$ is the wave number in the liquid crystal medium. For simplicity, the average refractive index and birefringence are assumed to be constant in the wavelength regions of interest. Then $\lambda/\lambda_0$ changes linearly as a function of position. If two CLC's are chosen such that CLC2 has a normalized wavelength $\lambda/\lambda_0$ which gives rise to high reflectivity and CLC1 has $\lambda/\lambda_0 = 1.076$ ( in Fig. 2.4), a smooth edge profile can be created in the overlap region as shown in Fig. 5.5. Assuming that the width of the overlap region is held constant, the slope of the
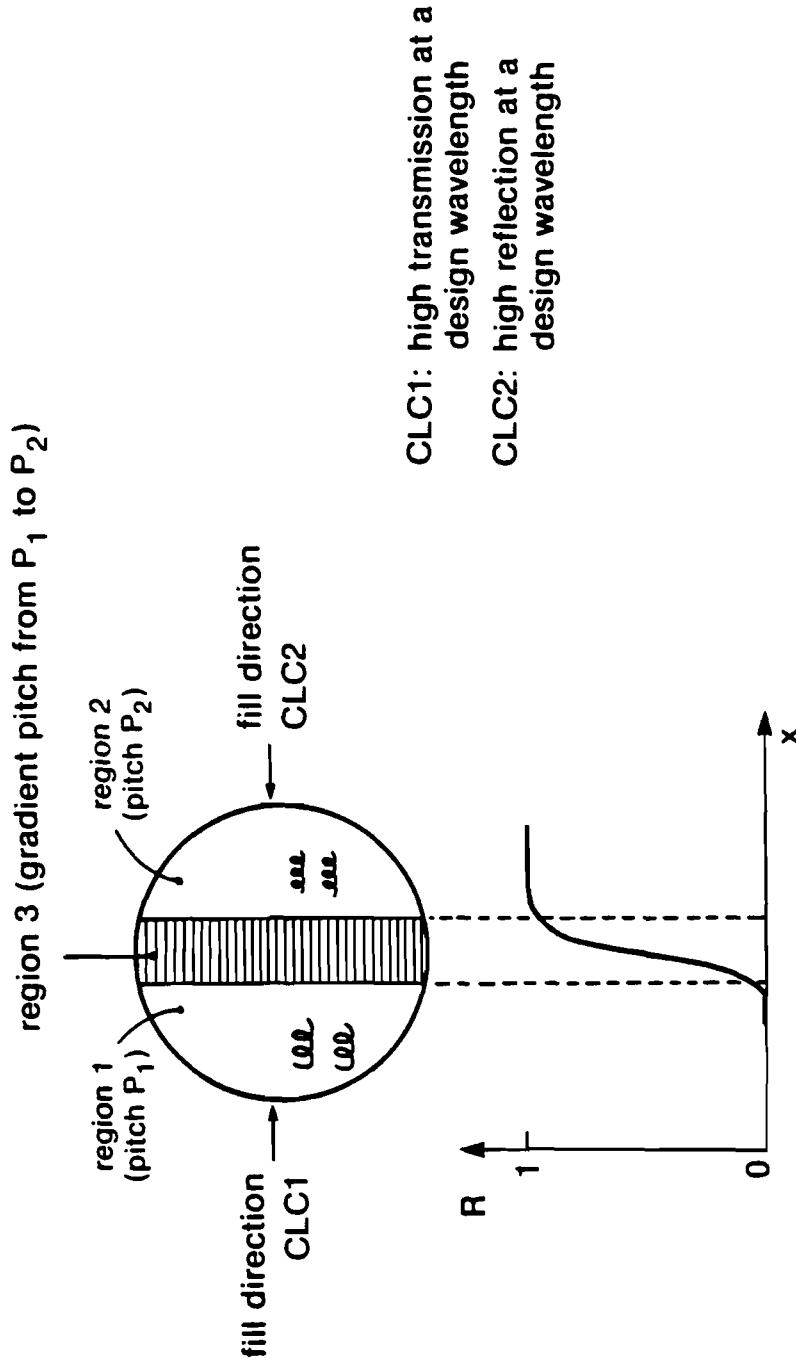
Fig. 5.5    Reflectivity profile for a gradient cholesteric liquid crystal element. The fluid-like property of cholesteric liquid crystals allows them to mix over a finite region of contact and create a pitch gradient. This results in a smoothly varying reflectivity profile.

transmission function across the overlap region can be varied by tuning the $\lambda/\lambda_0$ of CLC2 used for high reflection in Region 2 of Fig. 5.5. As the $\lambda/\lambda_0$ in Region 2 approaches 1.076, the slope across the overlap region (Region 3) is reduced, resulting in a softer reflectivity edge profile for the device.

There are several ways to create shaped gradients in $\Delta n$ and $n_{av}$: (1) by using the same host nematic with different concentrations of the same chiral additive, resulting in two distinctly different selective reflection bands with similar $\Delta n$; (2) by using different host nematics (allowing for variability in viscosity and birefringence) with the same chiral additive; and (3) by using different host nematics with different chiral additives.

## One-dimensional apodizer

Three cleaned, uncoated, nearly identical 38-mm diameter GCLC cells were assembled from borosilicate glass (BK-7) substrates. For each cell, the gap thickness was set at 13 μm with Mylar® spacers. Filling was done by capillary action at 60°C, above the isotropic transition temperature of nematic E7, with two different right-handed CLC blends, each containing a different amount of the chiral additive CB15. One CLC was tuned to exhibit a selective reflection peak at $\lambda_0 = 1064$ nm at 22°C, the other at $\lambda_0 = 820$ nm. A near planar structure was produced by the usual method of shearing. Figure 5.6 gives reflection spectra in the form of optical density for each CLC mixture in the visible and near infrared at 22°C. These spectral scans were taken with unpolarized optical radiation in a spectrophotometer (Perkin-Elmer Lambda-9). As mentioned earlier, the side lobes (or ripples) do not appear in spectra under conditions of weak anchoring, due to the nonuniformities in helix wave number of the
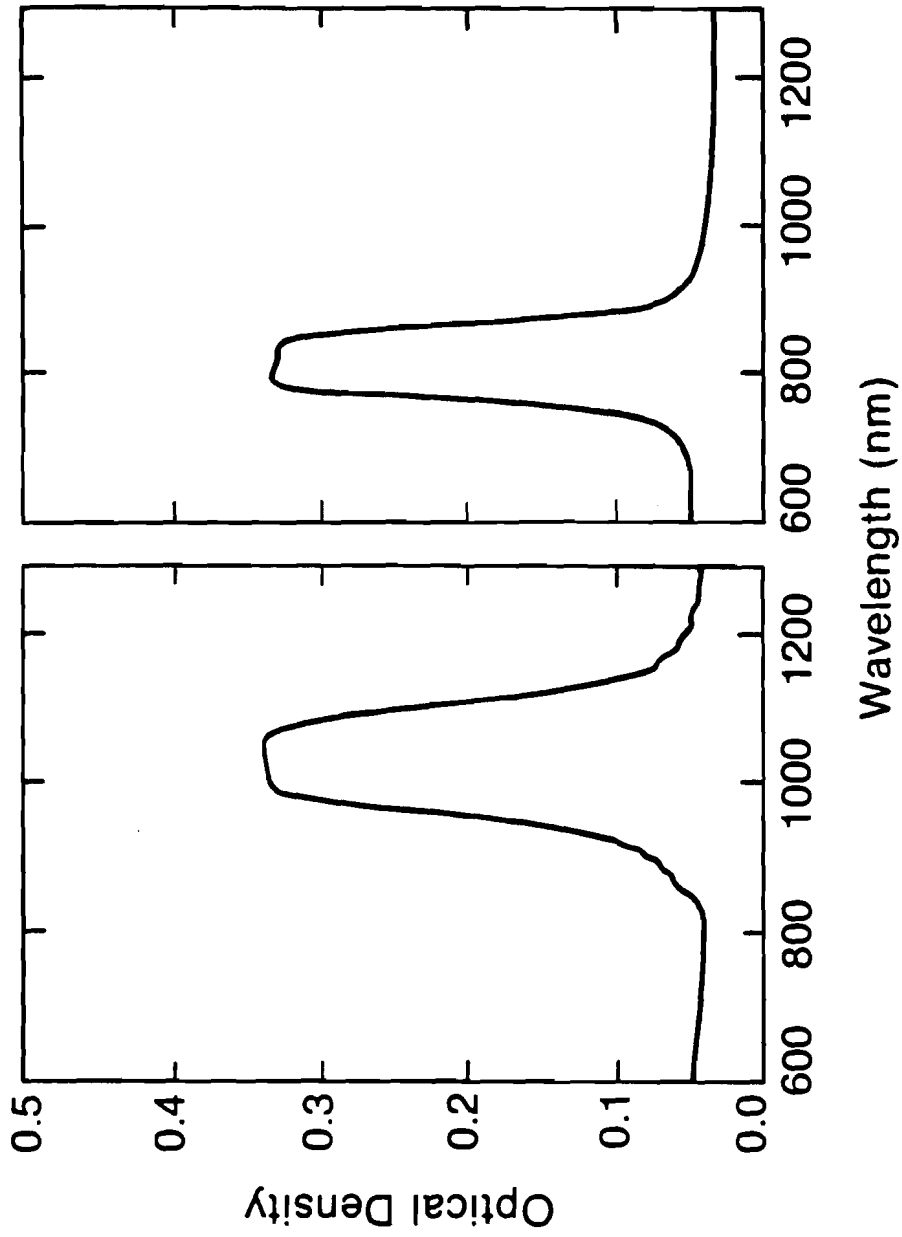
Fig. 5.6    Individual selective reflection bands for two different cholesteric liquid crystals used in fabricating a GCLC element.

molecules in the bulk. The slight tilt of the flat top region and the asymmetric selective reflection peak shapes in these scans come from a slight tilt in the planar structure induced by inner-substrate surface effects. The degree of selective reflection, as indicated by the magnitude of the change in optical density, $\Delta$O.D., from the base line, is equal to about 0.29, which shows good alignment. (The theoretical limiting value is equal to log 2 = 0.3.)

Figure 5.7 shows the transmission profiles of the three GCLC cells taken at T = 22°C. The size of the interface region is determined and can be controlled by the length of time during which the filled device is annealed at a temperature above the isotropic phase transition temperature of the mixtures. This keeps fluid viscosity low, and permits in-situ blending to occur.

The concept of controlled fluid blending to create a linear optical gradient can be exploited to make a one dimensional rectangular beam apodizer as shown in Fig. 5.8. This device can be constructed by taking two nearly identical GCLC cells whose fabrication was described above, and overlaying them as shown in the figure. In this configuration, the light is transmitted only in the overlap region where transmission (T) occurs for both cells. In the R regions light will be blocked by selective reflection. A transmission profile across one such apodizer is shown in Fig. 5.9. The clear aperture of the device can be adjusted by mechanically sliding the two GCLC elements relative to each other. One dimensional apodizers are useful for shaping beams which must pass through a slab-geometry amplifier.
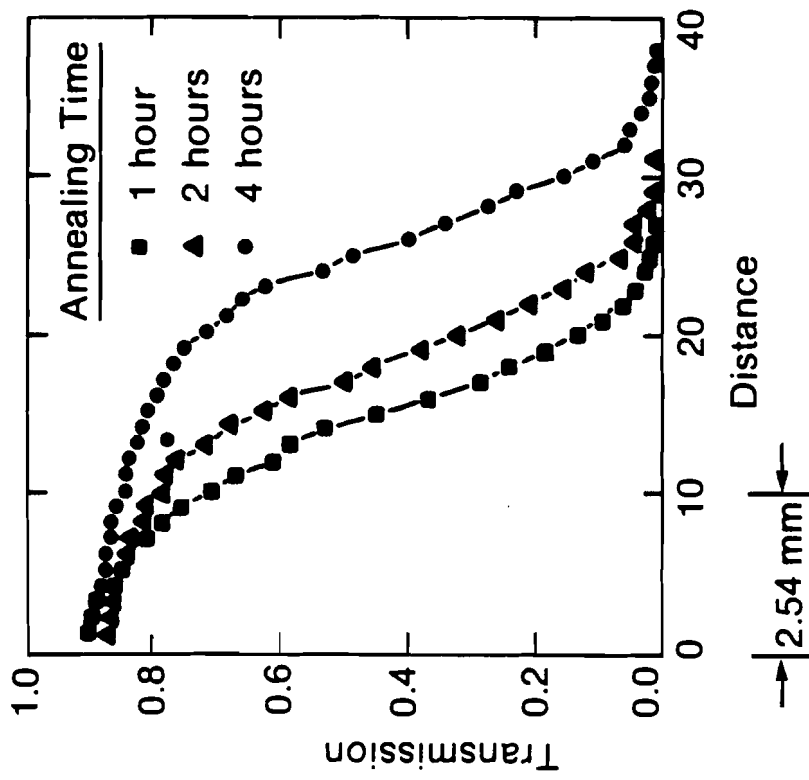
Fig. 5.7    Transmission for three GCLCs as a function of position after annealing periods of 1h, 2h, and 4h in the isotropic phase.
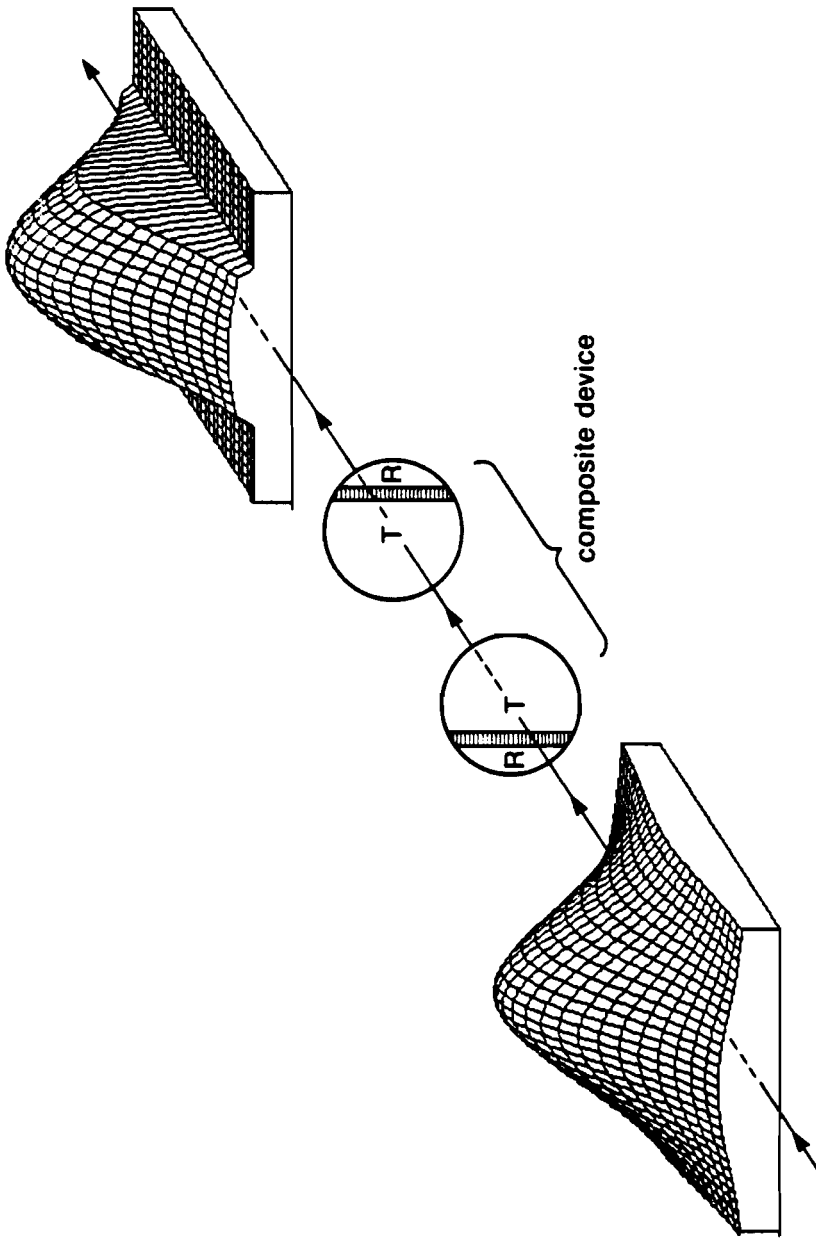
Fig. 5.8    A one-dimensional beam apodizer can be obtained by stacking a pair of two complimentary CLC cells. A variation in lateral position of the cells relative to each other allows for the adjustment of the clear aperture. In this illustration, R represents reflection of the incident beam, T represents transmission. The shaded area represents the mixing region in each element where a pitch gradient exist.

Fig. 5.9    Transmission profile of a one-dimensional apodizer. GCLCs which were annealed in the isotropic phase for 1h and 2h were chosen to construct the composite device.

## Circular beam apodizers of large clear aperture

The GCLC concept can be used to construct circular apodizers with a wider range of profiles. The concept is shown in Fig. 5.10(a). In this figure, CLC1 has high transmission and CLC2 has high reflection at the design wavelength. The fluid-like properties of CLC's allow them to mix together and form a pitch gradient region where the reflectivity cha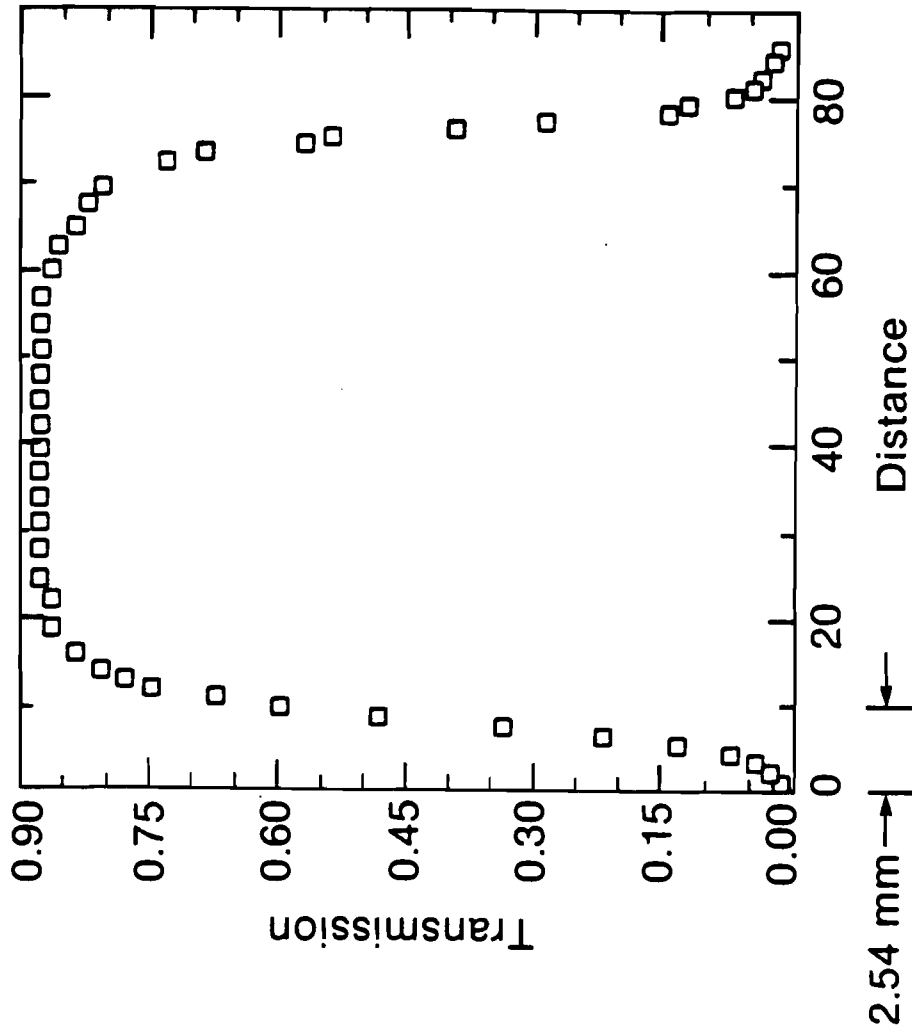nges from 0 to 1 outward radially from the center of the device. Good circular symmetry can be achieved by using slightly different radii of curvature for the supporting substrates so that CLC1 is drawn into the narrow gap area in the center by radial capillary action.

In order to prove the concept, two 50.8-mm diameter borosilicate glass (BK-7) substrates with $\rho = 1033.4$ mm and $\rho' = 1197.5$ mm were chosen to assemble a cell. Mixtures of ZLI1167 and CB15 (isotropic at 90°C, tuned to 910 nm) and E7 and CB15 (isotropic at 60°C, tuned to 1064 nm) were used as CLC1 and CLC2, respectively. This device is designed such that, with curved surfaces acting as the inner cell walls, the gap thickness at the inner edge of the CLC2 band is sufficient to give high reflection.

Fabrication proceeded as follows: First, CLC1 was filled by capillary action at 90°C until it assumed a good circular symmetry at the center of the cell. The cell was then cooled to 45°C and CLC2 was loaded in very slowly, so as not to initiate mixing. CLC1 tended to resist deformation because of its increased viscosity at the lower temperature. Once the filling of CLC2 was done, the temperature was increased up to 90°C for a one hour anneal in the isotropic phase of both blends. The element was then cooled down to room temperature and sheared to get good alignment. Photographs of an assembled device between two crossed polarizers are shown in Fig. 5.10(b).
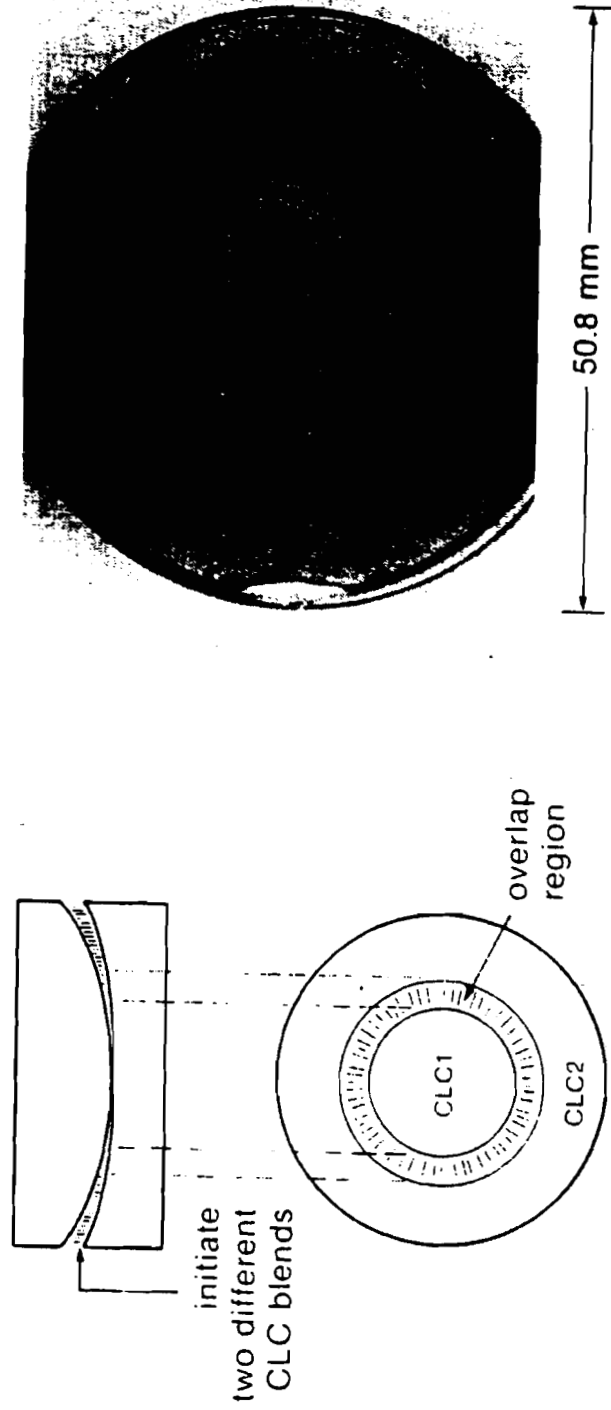
Fig. 5.10  Photograph between two linear polarizers, of a 1064-nm GCLC beam apodizer. For this apodizer, the mixture of CB15 in ZLI1167, tuned to 910 nm is used as CLC1; the mixture of CB15 in E7, tuned to 1064 nm is used as CLC2.

Experimental data (circles) taken at 22°C and a super-Gaussian fit (dashed line) are shown in Fig. 5.11. This apodizer profile is seen to match a super-Gaussian of order N = 8.3 with $r_0$ = 12.4 mm. The deviation from ideal performance in the central flat-top region where high transmittance is required, is a result of residual reflectance at 1064 nm from the wing of the CLC1 reflection band centered at 910 nm. It can be eliminated by preparing a CLC1 blend which has a selective reflection peak at a shorter wavelength than 910 nm. The slope at the edge of the apodizer can be changed by varying the length of time at which the filled device is thermally annealed at a constant temperature above the isotropic phase transition temperatures of the mixtures, where the viscosities are low. A slight asymmetry to the apodizer profile seen in Fig. 5.11 is a result of a wedge inadvertently introduced by epoxy in a sealing operation.

## 5.2. Nematic Liquid Crystal Profile-Tunable Laser Beam Apodizer[16]

Nematic liquid crystals (NLCs) are optically birefringent. When linearly polarized light propagates through a homogeneously aligned NLC cell with its optic axis at an angle of 45° with respect to the polarization direction of the light, the light interacts with two different refractive indices, $n_e$ and $n_o$. As a result, there will be a phase retardation $\delta_p$:

$$\delta_p = \frac{2\pi}{\lambda} \Delta n \, L$$

(8)

where $\Delta n = n_e - n_o$ is the optical birefringence, $\lambda$ is the wavelength of the incident light and L is the thickness of the birefringent material. When $\delta_p$ = 90°, the fluid acts as a
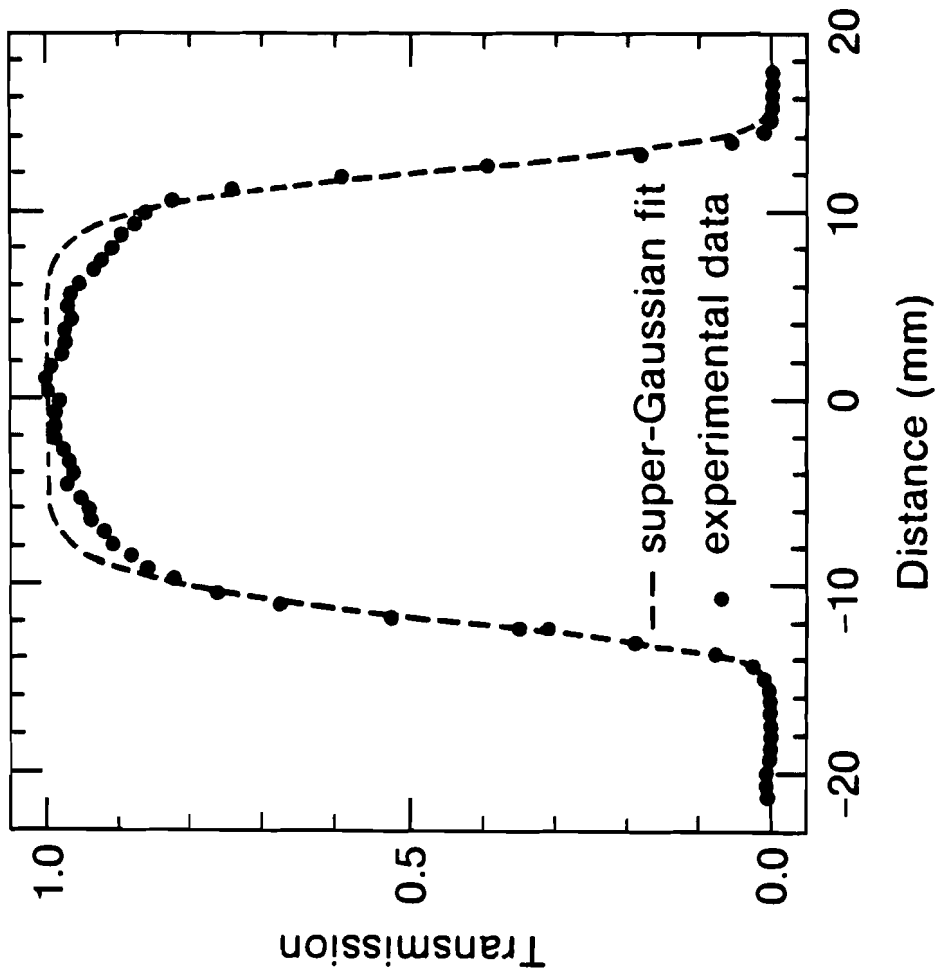
Fig. 5.11    Transmission profile of the GCLC apodizer in Fig. 5.10 at $\lambda = 1064$ nm. The circles are the experimental results and the dotted lines represent the best super-Gaussian fit to the data ($N = 8.3$, $r_0 = 12.4$ mm).

quarter wave plates, which changes linearly polarized light to circularly polarized light. When $\delta_p = 180°$, the fluid act as a half wave plate which rotates linearly polarized light by $90°$.

When an electric field perpendicular to optic axis is applied across the NLC fluid, the optic axis can be reoriented along the direction of the field. Let $\theta$ be the angle between the optic axis and the z-axis. Then the extra-ordinary refractive index seen by light propagating through the fluid is given by

$$\frac{1}{n_e^2(\theta)} = \frac{\cos^2\theta}{n_e^2} + \frac{\sin^2\theta}{n_o^2} \tag{9}$$

The angle $\theta$ depends on the field strength. In a strong electric field, $\theta$ becomes zero and the birefringence disappears. The angular distribution of $\theta$ for a strongly anchored NLC cell in an electric field is well described elsewhere.[17] In this case, the birefringence $\Delta n(\theta) = n_e(\theta) - n_o$ is a function of applied voltage, v and the phase retardation can be tuned continuously.

Many techniques for apodizing laser beams have been reported.[1-11] However, none of the devices based upon these techniques has found broad acceptance. One of the reasons is the lack of tunability of the edge transmission function in assembled devices.

In this section, we discuss a tunable laser beam apodizer by combining our liquid crystal technology and the radial birefringence element (RBE)[18] concept proposed by G. Giuliani et al. as a method of realizing a pseudo-Gaussian reflectance profile for unstable resonators. This device consists of a birefringent, nematic liquid crystal sandwiched betweeen two substrates as shown in Fig. 5.12. When
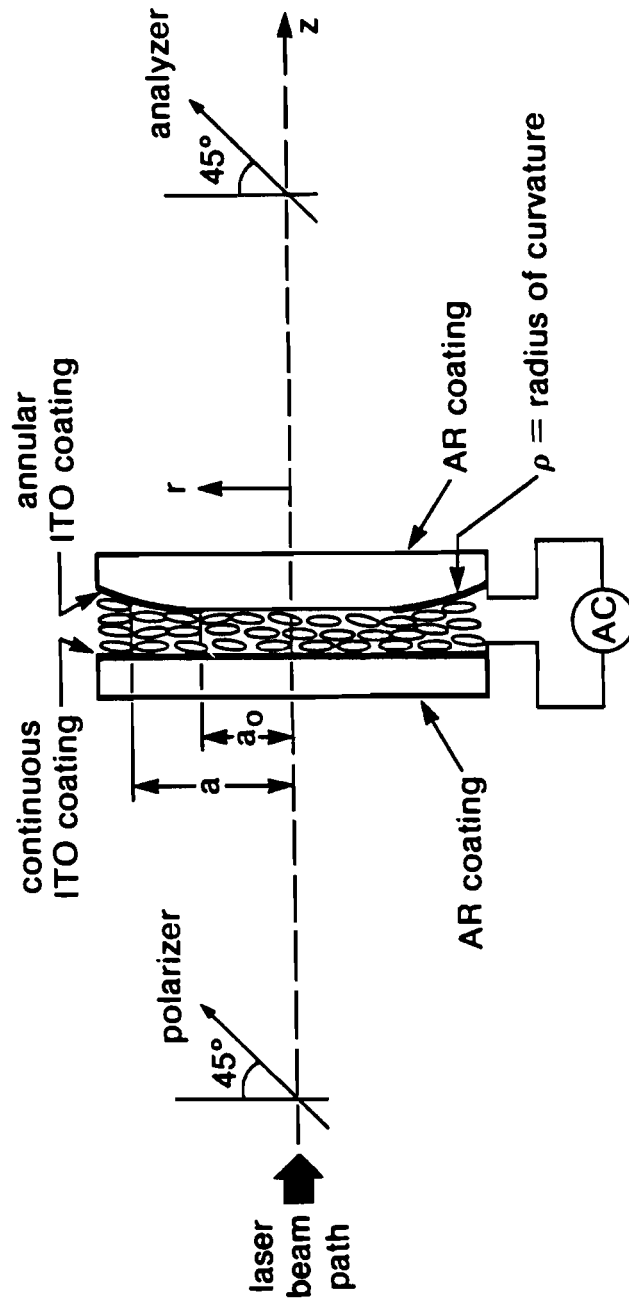
Fig. 5.12    Schematic diagram of a tunable laser beam apodizer. This device consists of a birefringent, nematic liquid crystal sandwiched between a plane parallel substrate and a plano-convex substrate with flat-top at the center region.

unpolarized light propagates through a homogeneously aligned NLC cell with its optic axis at an angle of 45° with respect to the polarization direction of the light, the normalized transmission function T(r) between parallel polarizers is given by

$$T(r) = \cos^2\left[\frac{\pi}{\lambda}\Delta nL(r)\right] \tag{10}$$

where $\Delta n$ is the birefringence of the nematic liquid crystal. $L(r)$ is the thickness variation of the birefringent medium which is given by

$$L(r) = \begin{cases} L(0) \\ \dfrac{r^2 - a_o^2}{2\rho} \end{cases} \tag{11}$$

where $\rho$ is the radius of curvature of the convex surface and $a_o$ is the location where the transmission starts to drop. The maximum transmission occurs when $L(0)$ is equal to

$$L(0) = \frac{N\lambda}{\Delta n} \qquad \text{where } N=1,2,3,\dots \tag{12}$$

For this condition, the transmission T(r) is given by

$$T(r) = \begin{cases} 1 & r \le a_o \\ \cos^2\left[\dfrac{\pi}{2}\dfrac{r^2 - a_o^2}{a^2 - a_o^2}\right] & r > a_o \end{cases} \tag{13}$$

If an annular, transmissive conductive coating is deposited around the inner edge of one substrates, the shape of the edge profile may be modified by a low ac voltage, v. Then the transmission function in Eq. (10) can be rewritteen by

$$
T(r,v) = \begin{cases} 1 & r \leq a_o \\ \cos^2\left[\dfrac{\pi}{2}\dfrac{r^2 - a_o^2}{a_{eff}^2 - a_o^2}\right] & r > a_o \end{cases}
\tag{14}
$$

where $a_{eff}^2 = \dfrac{\Delta n(0)}{\Delta n(v)}(a^2 - a_o^2) + a_o^2$ and $a_{eff}$ is the location where transmission goes to

zero. It is clear from the above that $a_{eff}$ is a function of applied voltage. Here $0 < \dfrac{\Delta n(v)}{\Delta n(0)} \leq 1$ and the absolute value of $\Delta n(0)$ is not important. Note that $a_{eff}/a > 1$,

that is, the clear aperture of the device increases with an increase in applied voltage. In order to reduce the phase distortion which leads to a focusing effect in the annular region, the refractive index of the liquid crystal should be well matched with the refractive index of each substrate. However, index-mismatching is indispensible for changing $\Delta n(v)/\Delta n(0)$. But this can be minimized by choosing materials with low birefringence $\Delta n(0)$. As a trade-off, this will require the increased gap thickness, $L(0)$ as one can see in Eq. (12). The plot of this transmission function for $(a_o/a)^2 = 0.4$ and $\Delta n(v)/\Delta n(0) = 0.6$ is shown in Fig. 5.13. The super-Gaussian fit to the curve shows that the transmission function of the device is close to the super-Gaussian of $N = 8$. The condition that the transmission at $r = a$ should be equal to zero, determines the radius of curvature $\rho$ of the convex surface.

$$
\rho = \frac{\Delta n}{\lambda}(a^2 - a_o^2)
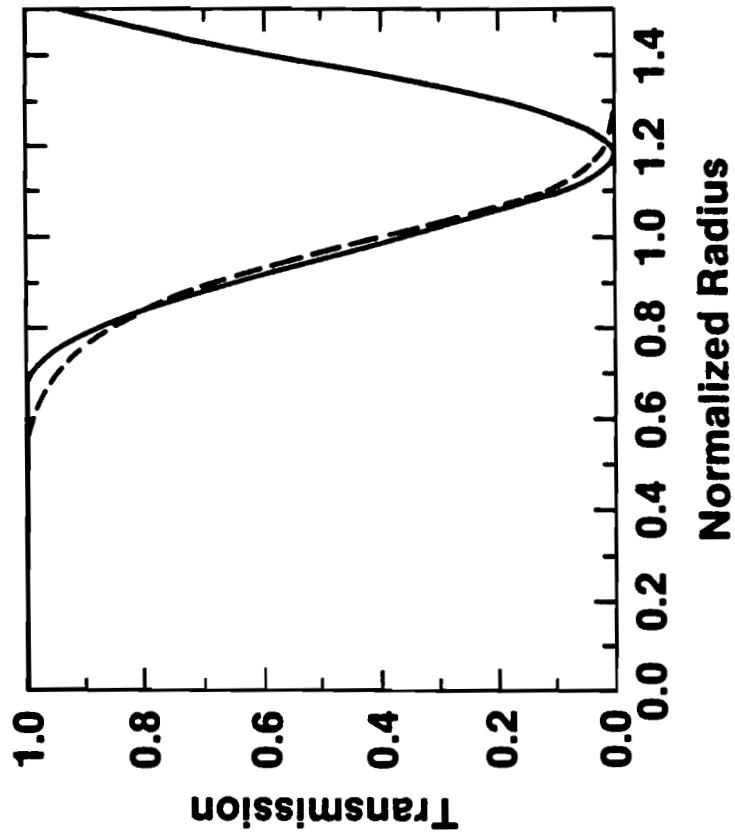\tag{15}
$$

Fig. 5.13    Transmission profile of the tunable apodizer. The solid line represents the case where $\Delta n(v)/\Delta n(0) = 0.6$ and $(a_o/a)^2 = 0.4$. The dotted line represents a super-Gaussian fit to the data.

For a proof of concept, a plano-convex borosilicate glass (BK-7) substrate with $\rho = 1.5$ m was fabricated and polished to have a flat-top region. The nematic liquid crystal E7, which has $\Delta n = 0.18$ at 1064 nm, was used without considering index-matching. The locations and thicknesses of Mylar® spacers were chosen to maximize transmission at the center of the cell. Newton ring patterns were used as a guide to establish circular symmetry of the device before filling with the liquid crystal fluid. Photographs of the device between parallel (a) and crossed (b) polarizers are shown in Fig. 5.14. A two-dimensional, transmission profile at 1064 nm was obtained by with a CID camera as shown in Fig. 5.15. The algorithm to measure transmission profile is as follows:

$$T(r) = \frac{I_0(r) - B}{I_i(r) - B}$$

(16)

where $I_i(r)$ and $I_0(r)$ are the input and output intensity profiles and B is the background intensity. In this figure, the side lobes in the transmission profile would be cut out in any laser system application by a hard-edged aperture. However, this procedure would not produce any diffraction because there is no light at the first side minima. The transmission profile as a function of applied voltage is depicted in Fig. 5.16. This figure shows that when the applied voltage is increased from 0 to 10 $V_{p-p}$, the order of super-Gaussian change from 14.1 to 12.89 and the clear aperture changes from 7.25 mm to 8.93 mm.

The wavefront quality of the device was measured using Mach-Zehender interferometry. The wavefront quality for extra-ordinary ($\Gamma_e$) and ordinary waves ($\Gamma_o$) were measured separately as shown in Table 5.1. As mentioned earlier, spherical
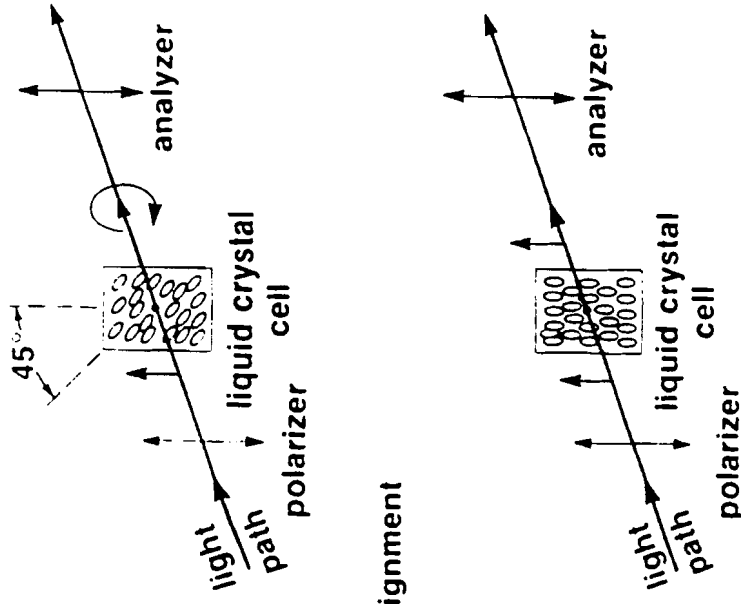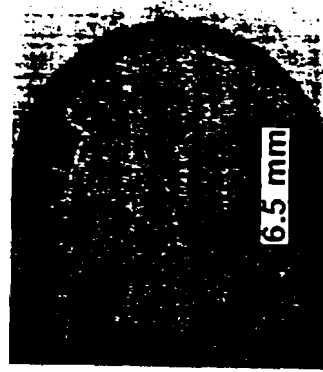
Fig. 5.14    Photographs of the device between parallel polarizers on a light box. When the long axes of the molecules are aligned at an angle of 45° (above) 0° (below) with respect to the transmission axis of the polarizers.
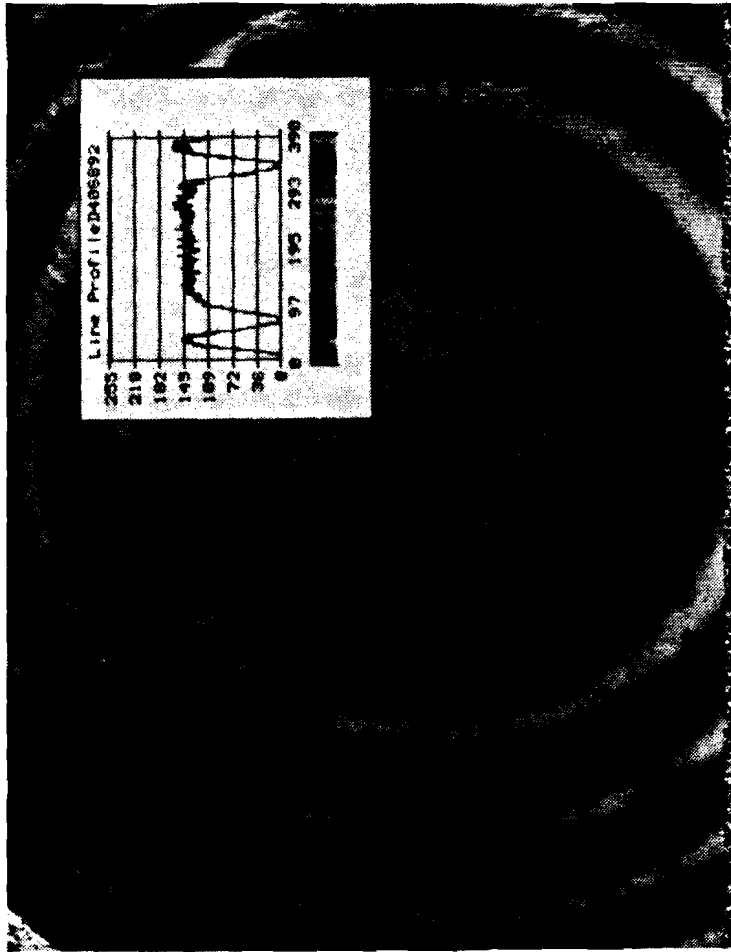
Fig. 5.15    Transmission profile of the apodizer at 1064 nm.

| V$_{p,p}$(V) | 0 | 6 | 10 |
|---|---|---|---|
| closest super-Gaussian order (N) | 14.1 | 13.7 | 12.89 |
| C.A. (mm) | 7.25 | 7.78 | 8.93 |
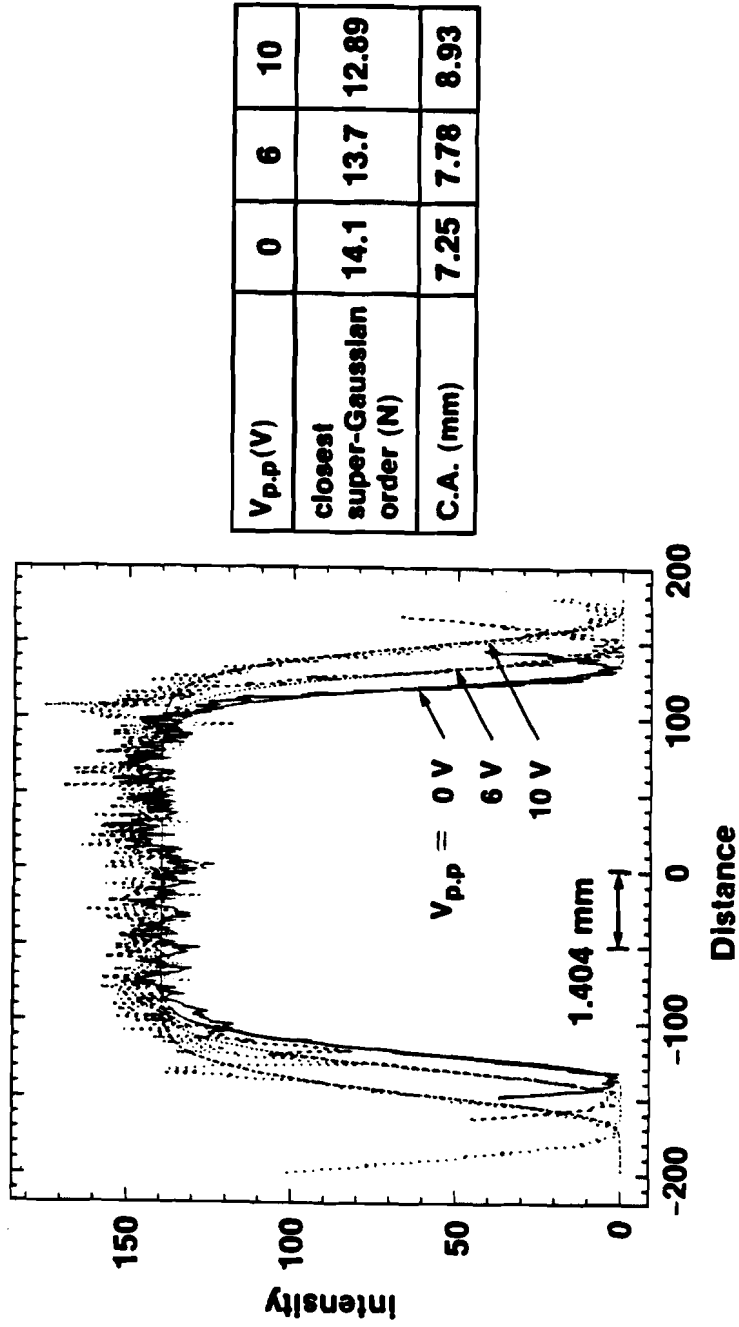


Fig. 5.16    Transmission profile of the device as a function of applied voltage.

aberration (focus) can be reduced by using low birefringence liquid crystals, index-matched to the substrate.

**Table 5.1**

**Wavefront Quality of the Tunable Laser Beam Apodizer.**

| Wavefront Quality (wave numbers) | $\Gamma_o$ | $\Gamma_e$ |
|---|---|---|
| RMS (without focus) | 0.02 | 0.09 |
| Peak value | 0.15 | 0.37 |
| Focus | 0.12 | 0.67 |
| Coma | 0.07 | 0.13 |
| Astigmatism | 0.02 | 0.03 |
| Spherical | 0.24 | 1.16 |

## REFERENCES

1.  V. R. Costich and B. C. Johnson, "Apertures to Shape Highpower Beams," Laser Focus 10, 43 (1974).

2.  A. Penzkofer and W. Frohlich, "Apodizing of Intense Laser Beams with Saturable Dyes," Opt. Commun. 28, 197 (1979).

3.  Y. Asahara and T. Izumitani, "Process of Producing Soft Aperture Filter; Heat Treatment of Glass Composed of Oxides of Sodium, Silicon, Zinc, Aluminum, Tin and/or Arsenic in a Silver Salt Bath," U.S. Patent 4,108,621 (August 22, 1978).

4.  G. Dubé, "Progress in Glass Components for Neodymium Lasers," Advanced Laser Technology and Applications, L. Esterowitz, ed., Proc. Soc. Photo-Opt. Instrum. Eng. Vol 335, 10 (1982).

5.  V. I. Kryzhanovskii, B. M. Sedov, V. A. Serebryakov, A. D. Tsvetkov, and V. E. Yashin, "Formation of the Spatial Structure of Radiation in Solid-State Laser Systems by Apodizing and Hard Apertures," Sov. J. Quantum Electron. 13, 194 (1983).

6.  A. J. Campillo, B. Carpenter, B. E. Newnam, and S. L. Shapiro, "Soft Apertures for Reducing Damage in High-Power Laser-Amplifier System," Opt. Commun. 10, 313 (1974).

7.  E. W. S. Hee, "Fabrication of Apodized Apertures for Laser Beam Attenuation," Opt. Laser Technol. 7, 75 (1975).

8.  S. B. Arifzhanov, R. A. Ganeev, A. A. Gulamov, V. I. Redkorechev, and T. Usmanov, "Formation of a Beam of High Optical Quality in a Multistage Neodymium Laser," Sov. J. Quantum Electron. 11, 745 (1981).

9.  G. Dubé, "Total Internal Reflection Apodizers," Opt. Commun. 12, 344 (1974).

10. J.-C. Diels, "Apodized aperture using frustrated total reflection," Appl. Opt. 14, 2810 (1975).

11. B. J. Feldman and S. J. Gitomer, "Annular Lens Soft Aperture for High Power Laser Systems," Appl. Opt. 16, 1484 (1977).

12. S. D. Jacobs, K. A. Cerqua, K. L. Marshall, A. Schmid, M. J. Guardalben, and K. J. Skerrett, "Liquid-Crystal Laser Optics: Design, Fabrication, and Performance," J. Opt. Soc. Am. B 5 (9), 1962–1979 (1988).

13. Jae-Cheul Lee, S. D. Jacobs, and K. J. Skerrett, "Laser Beam Apodizer Utilizing Gradient-Index Optical Effects in Liquid Crystals," Opt. Eng. submitted for publication.

14. P. D. de Gennes, The Physics of Liquid Crystals, (Oxford, Claredon ,1974), pp. 240–241.

15. Ibid, pp..264-266

16. Jae-Cheul Lee, S. D. Jacobs, T. J. Kessler, and N. Van Lieu, "Profile-Tunable Laser Beam Apodizer," presented at CLEO '89, Baltimore, MD, 24–28 April 1989.

17  S. T. Kowel, E. Balizer, T.T. Su, I. H. Loh, P. Cleverly, G. C. Martin and P. G. Kornreich, Polymeric microelectronics. US Army Report #DAAK70-80-C-0053-1.

18. G.Giuliani, Y. K. Park, and R. L. Byer, "The radial birefringent elements and its application to laser resonator design," Opt. Lett. 5, 491 (1980).

# VI. CONCLUSIONS

In this thesis, the optical properties of cholesteric liquid crystals (CLCs) and their applications in laser resonators and amplifiers were described.

CLCs have selective reflection in wavelength and polarization and the optical rotatory power of the CLC elements results from the helical structure of the molecules. And the field reflected by the CLC preserves its sense of circular polarization, whereas the field reflected from a conventional dielectric mirror changes its sense of circular polarization. The Jones matrix for the CLC element was derived for the first time.

We showed both in theory and experiment that under exposure to a plane wave with a Gaussian intensity distribution, a retro-self-focusing effect occurs in which the reflected field comes to focus, as a result of transverse, optical field-induced pitch dilation in a CLC. When this CLC element was used as a laser end mirror in a cw Nd:YAG laser, it acted like a well aligned concave mirror/pinhole combination. $TEM_{00}$ mode operation was obtained as a result of this pinholing effect. At the same time, this laser resonator was operated in a mono-longitudinal mode. A CLC element as a laser end mirror provides orthogonal polarizations in a gain medium to eliminate spatial hole burning, which would otherwise lead to multi-longitudinal modes. $TEM_{00}$ mode and mono-longitudinal mode operation with 1.3 W cw output were demonstrated to occur simultaneously in a commercial Nd:YAG laser resonator with CLC end mirrors.

The small-signal gain of the Cr:Nd:GSGG active mirror amplifier was squared by placing a passive CLC element in front of the active mirror amplifier. The small-signal gain at the maximum bank energy of 460 J was 1.46 without the CLC and 2.05 with the CLC.

We designed, fabricated and characterized liquid crystal laser beam apodizers with large clear apertures. The construction of these devices was based on fluid thickness variation or gradient-index optical effects in liquid crystals. A circular apodizer was demonstrated, in which the thickness variation of the CLC fluid was defined by two substrates with different inner surface radii of curvature. This device had fixed edge profile given by a super-Gaussian of order $N=3.51$. The ability to vary $N$ in this design was estabilished by using the mixing properties of liquid crystals to create a gradient index optical effect. One device combining both the fluid thickness variation and the gradient-optical effect was fabricated. The order of super-Gaussian was $N=8.3$ with clear aperture of 28.8 mm. An electro-optic, profile tunable apodizer, based on nematic liquid crystals was fabricated. This device would br useful where final, in-situ fine tuning in both clear aperture and the order of super-Gaussian edge-profile are required. When the applied voltage to the device was increased from 0 to 10 $v_{p-p}$, the order of the super-Gaussian changes from 14.1 and 12.89 and the clear aperture changed from 7.25 mm to 8.93 mm.

Further researches can be extended to see :1) how CLC mirrors will work with the broad-band gain medium such as Nd:glass or Ti:saphire, 2) how CLC resonators will perform in pulse mode operation (Q switch or mode-locking), and 3) how liquid crystal laser beam apodizers will perform in real high power laser systems.